2018

Quality improvement in wire arc additive manufacturing

Bintao Wu
University of Wollongong

UNIVERSITY
OF WOLLONGONG
AUSTRALIA

QUALITY IMPROVEMENT IN WIRE ARC ADDITIVE MANUFACTURING

A thesis submitted in fulfilment of

the requirements for the award of the degree

DOCTOR OF PHILOSOPHY

from

UNIVERSITY OF WOLLONGONG

By

BINTAO WU

B. Eng., M. Eng.

School of Mechanical, Materials, Mechatronics and Biomedical Engineering

Faculty of Engineering and Information Sciences

August, 2018

CERTIFICATION

I, Bintao Wu, declare that this thesis, submitted in fulfilment of requirements for award of Doctor of Philosophy at school of Mechanical, Materials, Mechatronics and Biomedical Engineering, University of Wollongong, Australia, is wholly my own work unless otherwise referenced and acknowledge. The document has not been submitted for qualifications at any other or academic institution.

Type name: Bintao Wu

Signature:

Date: August, 2018

ACKNOWLEDGEMENTS

I wish to express my sincere appreciation and gratitude to my supervisor, Prof. Huijun Li, and co-supervisor A/Prof. Zengxi Pan, and Dr. Dominic Cuiuri, for their valuable guidance, support, inspiration and close supervision during my PhD candidature in University of Wollongong (UOW). The assistance they provided in my studies over the last two years is the key factor for the successful completion of this work.

I would like to express my warmest thanks to Dr. Donghong Ding, Chen Shen, and Yan Ma for their valuable discussion, good friendship and encouragement.

I am deeply grateful to the staffs from the UOW Welding and Industrial Automation Research Centre, and Australia institute for innovative materials center for their expertise and extensive use of facilities. A special thanks to Matthew Franklin and Nathan Tarlinton for their support.

I would also like to convey sincere appreciation to all the members of the Faculty of Engineering and Information Science at UOW and Engineering Enquiry Centre staff for assisting in administration work.

I also appreciate the assistance from the China Scholarship Council (CSC), University of Wollongong (UOW) for providing the scholarships to support my study.

Finally, I wish to express my special thanks to all my friends and to my family for their support and encouragement during my PhD candidature career.

ABSTRACT

In recent years, significant progress has been made in the development of the Wire Arc Additive Manufacturing (WAAM) processes due to its economically produced large-scale metal components with relatively high deposition rate. As WAAM has evolved, a wide range of materials have become associated with the processes and applications. Today, producing high-quality WAAM products and improving their potential service life are still a challenge. This dissertation focuses primarily on critical issues and methodologies to improve quality performance of component fabricated by WAAM technique.

The research was the first attempt to study the WAAM process from complex thermal behaviour point of view. It is found that due to the influences of thermal accumulation, the interlayer's surface oxidation, bead geometry, microstructural evolution, grain size, and crystalline phase vary along the building direction of the as-fabricated wall, which creates variations in arc shape, metal transfer behaviour, mechanical properties and fracture features. Additionally, the corrosion behaviour within the WAAM-processed part is anisotropic due to corresponding anisotropy in microstructure, phase structure, grain size and orientation. The research provides a better understanding of the effects of heat accumulation behaviour on deposition stability and material properties during WAAM process, which benefits future process control, improvement, and optimization.

To achieve improved microstructure and mechanical properties, an innovative WAAM process with forced interpass cooling using compressed CO_2 was employed in this research.

ABSTRACT

It is found that the forced interpass cooling is beneficial to additively manufactured components, contributing to an appealing surface finish with less visible surface oxidation, refined microstructure, improved hardness, enhanced strength and low distortion. Active interpass cooling not only improves deposition properties, but also promotes geometrical repeatability and also improved manufacturing efficiency through the reduction of dwell time between layers.

A quality-based framework is proposed in the last section of the thesis, aiming to produce high-quality and defect-free WAAM components. This thesis concludes that the wide application of WAAM still presents many challenges, and these may need to be addressed in specific ways for different materials in order to achieve an operational system in an acceptable time frame. The integration of materials and manufacturing process to produce defect-free and structurally-sound deposited parts remains a crucial effort into the future.

TABLE OF CONTENTS

ABBREVIATIONS AND SYMBOLS

Abbreviations

WAAM	Wire Arc Additive Manufacturing
GTAW	gas tungsten arc welding
GMAW	gas metal arc welding
CMT	cold metal transfer
BPF	Power-Bed Fusion
UOW	University of Wollongong
CAD	computer-aided design
3D	3-dimensional
ASTM	American Society for Testing Materials
YS	yield strength
UTS	ultimate tensile strength
EI	elongation
CMT-P	cold metal transfer- pulse
CMT-ADV	cold metal transfer- advanced
CO_2	carbon dioxide
UIT	ultrasonic impact treatments
AM	Additive Manufacturing
LBM	Laser Beam Melting
EBM	Electron Beam Melting
IR	infrared
H_2O	water
HNO_3	concentrated nitric acid

HF	hydrofluoric acid
OM	Optical Microcopy
SEM	scanning electron microscopy
EDS	energy dispersive X-ray spectroscopy
XRD	X-ray diffraction
BM	base material, base metal
HAZ	heat affected zone
TIG	tungsten inert gas
MIG	metal inert gas

Symbols

β	beta phase, body-centred cubic structure in Ti_6Al_4V
α	alpha phase, face-centred cubic structure in Ti_6Al_4V
°C	Celsius degree
$g \cdot cm^{-3}$	gram per cubic centimetre
at.%	atom percent
σ_y	yield strength
$\sigma_{0,y}$	lattice frictional stress
d	average grain diameter
L/min	litre per minute
mm/min	millimetre per minute
wt.%	weight percent
rpm	revolutions per minute
mm/s	millimetre per seconds
°	degree

min^{-1}	per minute
kV	Kilovolts
mA	milliampere
g	gram
s^{-1}	per seconds

LIST OF FIGURES

LIST OF TABLES

Chapter 1 INTRODUCTION

1.1 Background

In recent years, wire arc additive manufacturing (WAAM) has increasingly attracted attention from the industrial manufacturing sector due to its ability to create large metal components with high deposition rate, low equipment cost, high material utilization, and consequent environmental friendliness. The origin of the WAAM process can be traced back to 1925s when Baker [1] proposed to use an electric arc as the heat source with filler wires as feedstock materials to deposit metal ornaments. Since then, consistent progress has been made on the development of this technology, particularly in the last 10 years; the WAAM technique bears various nomenclatures by different research institutions worldwide [2-24], as shown in **Figure** 1-1. Today, WAAM has become a promising fabrication process for various engineering materials such as titanium, aluminium, nickel alloy and steel. Compared to traditional subtractive manufacturing, the WAAM system can reduce fabrication time by 40-60% and post-machining time by 15-20% depending on the component size[25]. For instance, recent breakthrough in WAAM technology has made it possible to fabricate landing gear rib with a saving of approximately 78% in raw material when compared with the traditional subtractive machining process[26].

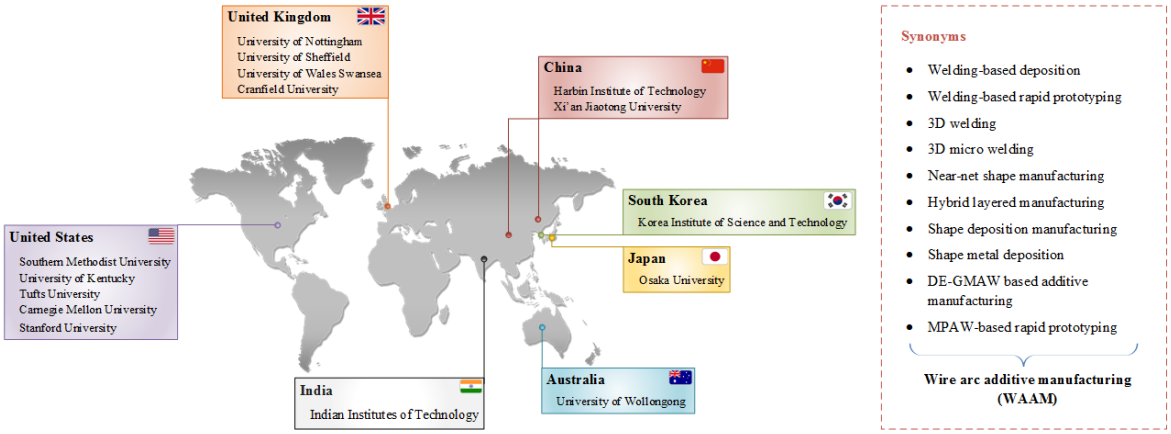

Figure 1-1 Different terminology of WAAM named by various research groups

Due to the highly complex nature of WAAM, many different aspects of the process need to be studied, including processes development, material quality and performance, path design and programming, process modelling, process monitoring and online control[27]. Several WAAM review papers have been published by leaders in the field, covering the state-of-the-art systems, design, usage, in-situ process monitoring, in-situ metrology and in-process control and sensing [26, 28-32].

1.2 Objective of current research

The main objective of this research is to investigate the effects of thermal accumulation on the deposition stability and material properties during WAAM process with the aim of providing strategies for further process control and optimization. Furthermore, to avoid the generation of the defects during deposition and to improve manufacturing efficiency, an innovative WAAM process with active interpass cooling using compressed CO_2 gas is proposed. Based on the research work, a quality-based framework will be presented in

conclusion, aiming to achieve high-quality and defect-free WAAM components. The research tasks completed in this dissertation are now listed in **Figure 1-2**.

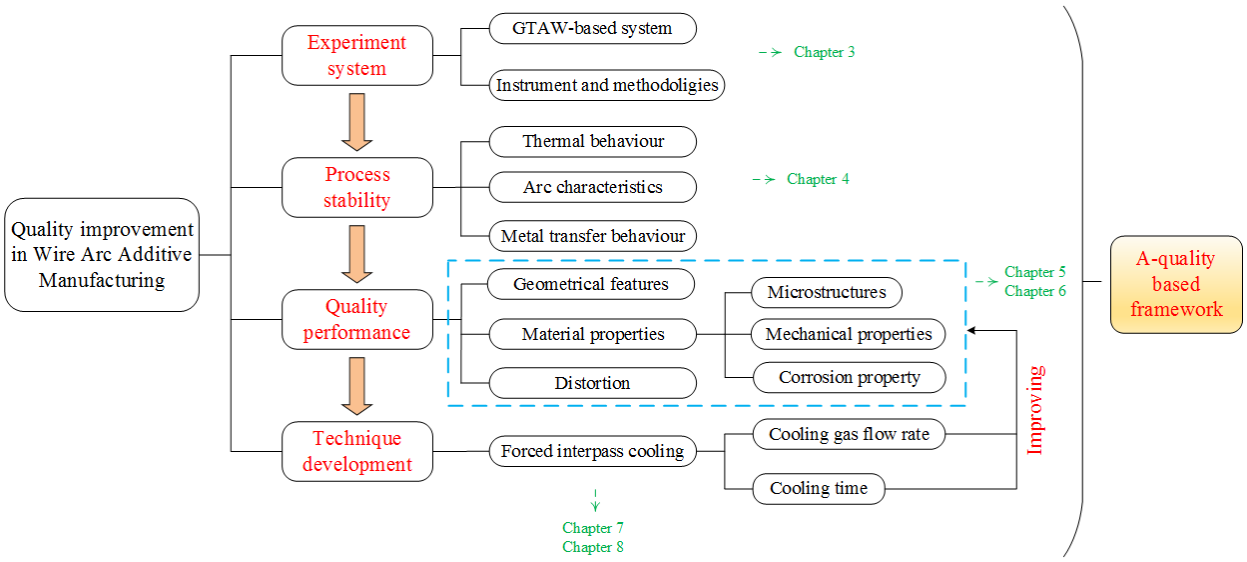

Figure 1-2 Outline of this dissertation

1.3 Outline of thesis

This thesis is organized as follows:

Chapter 2 reviews the microstructure and mechanical properties of various metals, including titanium and its alloys, aluminum and its alloys, Ni-based alloy, steel and other intermetallic materials fabricated by the various WAAM processes. The common defects that have been found to occur for different materials are also summarized. The current methods for both in-process and post-process quality improvement and defect reduction are introduced.

Chapter 3 introduces the experiment instruments and methodologies that have been used in this study.

Chapter 4 investigates the influence of heat accumulation on bead formation, arc

stability, metal transfer behaviour during the manufacture of Ti6Al4V with the gas tungsten wire arc additive manufacturing (GT-WAAM) using localized gas shielding. An infrared pyrometer is used to measure the in-situ interpass temperature and arc stability and metal transfer behaviour are monitored by means of a high-speed camera.

Chapter 5 further investigates the effects of heat accumulation on microstructure and mechanical properties of additively manufactured Ti6Al4V parts by means of optical microscopy (OM), X-ray diffraction (XRD), scanning electron microscopy (SEM), energy dispersive spectrometer (EDS) and standard tensile tests, aiming to explore the quality performance of fabricating Ti6Al4V parts by GT-WAAM using localized gas shielding.

Chapter 6 investigates the relationships between corrosion resistances, microstructure and phase composition of Ti-6Al-4V components that have been fabricated with the gas tungsten wire arc additive manufacturing (GT-WAAM) process, through the use of electrochemical corrosion testing, optical microscopy, X-ray diffraction and hardness testing, trying to provide a strategy for the anisotropic corrosion behaviour of additive manufactured part.

Chapter 7 proposes an innovative manufacturing process with forced interpass cooling using compressed CO2 to achieve improved microstructure and mechanical properties. The effects of various interpass temperatures and rapid forced cooling on deposition geometry, thermal distortion, surface oxidation, microstructural evolution, and mechanical properties of the fabricated part were investigated.

Chapter 8 conducts a comparative analysis of simulation and experimental investigation on the effects of forced interpass cooling on the thermal state during deposition process, and

further to characterize the geometry and thermal distortion of build part.

Chapter 9 gives a discussion on improving quality of WAAM fabricated parts through process selection, feedstock optimization, process monitoring and control and post-process, including proposals for future research directions.

1.4 Original Research Contributions

The main contributions of the dissertation are threefold.

(1) In-depth study of the heat accumulation effects on the process stability and material properties of WAAM-fabricated component.

Complex thermal behaviour during fabrication plays an import role in the process stability, geometrical formation and mechanical properties of components manufactured using WAAM technology. Owing to the influences of heat accumulation, the interlayer surface oxidation, bead geometries, microstructural evolution, grain size, and crystalline phase vary along the building direction of the as-fabricated wall, which leads to the variations in arc shape, metal transfer behaviour, mechanical properties and fracture features. A better understanding of the relations between thermal accumulation and process stability, material properties will benefit future process control, improvement, and optimization.

(2) A newly developed active interpass cooling technique for WAAM to achieve improved component quality.

An innovative wire arc additive manufacturing (WAAM) process with forced interpass cooling using compressed CO_2 was employed in this dissertation. Forced interpass cooling using compressed CO_2 gas is easily implemented, and is beneficial to additively manufactured Ti6Al4V components, contributing to an appealing surface finish with less

visible surface oxidation, refined microstructure, improved hardness, enhanced strength and low distortion. Furthermore, it significantly promotes manufacturing efficiency through a sharp reduction of dwell time between the deposited layers.

(3) The development of a quality-based framework for WAAM components

Based on an in-depth understanding of various materials, ideal process setup, in-process parameter control and post processing, a quality-based framework is proposed, for producing high-quality and defect-free components. Three main aspects are primarily considered: feedstock optimization, manufacturing process, and post-process treatment.

Chapter 2 LITERATURE REVIEW

This chapter reviews the microstructure and mechanical properties of various metals, including titanium and its alloys, aluminum and its alloys, Ni-based alloy, steel and other intermetallic materials fabricated by the various WAAM processes. The common defects that have been found to occur for different materials are also summarized. The current methods for both in-process and post-process quality improvement and defect reduction are introduced. Finally, a discussion is given on improving quality of WAAM fabricated parts through process selection, feedstock optimization, process monitoring and control and post-process, including proposals for future research directions.

2.1 Wire Arc Additive Manufacturing (WAAM) systems

Depending on the nature of the heat source, there are commonly three types of WAAM processes: Gas Metal Arc Welding (GMAW)-based[33], Gas Tungsten Arc Welding (GTAW)-based[2] and Plasma Arc Welding (PAW)-based[3]. As listed in **Table 2-1**, specific class of WAAM techniques exhibit specific features. The deposition rate of GMAW-based WAAM is 2-3 times higher than that of GTAW-based or PAW-based method. However, the GMAW-based WAAM is less stable and generates more weld fume and spatter due to the electric current acting directly on the feedstock. The choice of WAAM technique directly influences the processing conditions and production rate for a target component.

Table 2-1 Comparison of various WAAM techniques

WAAM	Energy source	Features
GTAW-based	GTAW	Non-consumable electrode; Separate wire feed process; Typical deposition rate: 1-2kg/hour; Wire and torch rotation are needed;
GMAW-based	GMAW	Consumable wire electrode; Typical deposition rate 3-4kg/hour; Poor arc stability, spatter;
	Cold metal transfer (CMT)	Reciprocating consumable wire electrode; Typical deposition rate: 2-3kg/hour; Low heat input process with zero spatter, high process tolerance;
	Tandem GMAW	Two consumable wires electrodes; Typical deposition: 6-8kg/hour; Easy mixing to control composition for intermetallic materials manufacturing ;
PAW-based	Plasma	Non-consumable electrode; Separate wire feed process; Typical deposition rate 2-4kg/hour; Wire and torch rotation are needed;

Most WAAM systems use articulated industrial robot as the motion mechanism. Two different system designs are available. The first design uses an enclosed chamber to provide a good inert gas shielding environment similar to laser Power-Bed Fusion (PBF) system. The second design uses existing or specially designed local gas shielding mechanism with the robot positioned on a linear rail to increase the overall working envlop. It is capable of fabricating very large metal structure up to a meter in dimension. **Figure 2-1** shows an example of this design of WAAM system, used for the research and development at the University Wollongong (UOW).

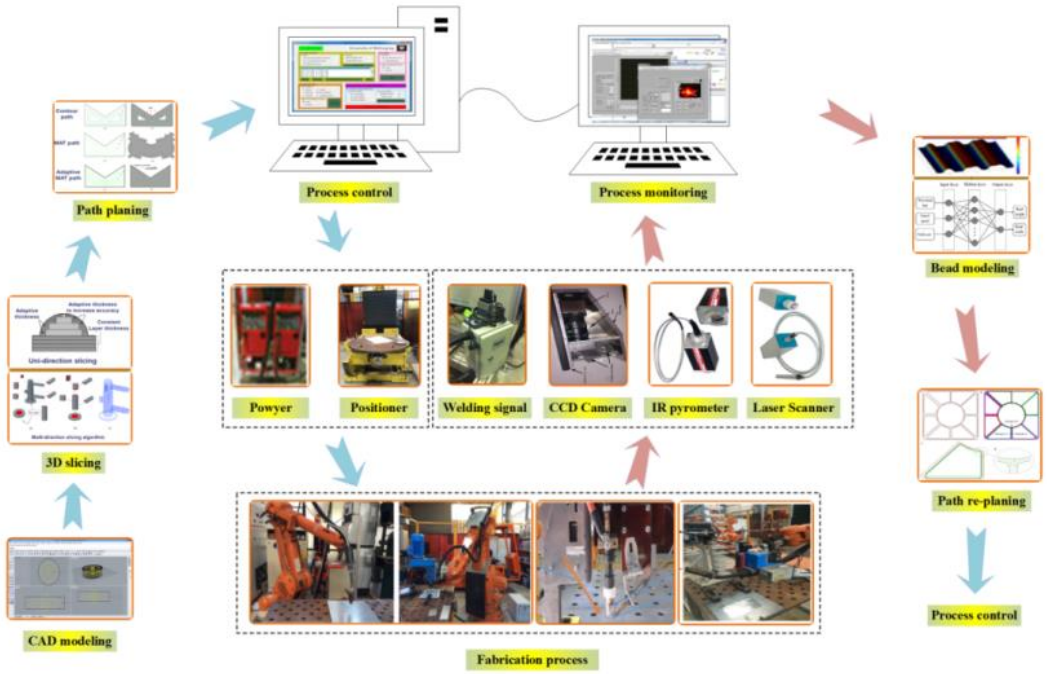

Figure 2-1 WAAM system design concepts, University of Wollongong

Fabricating a part using WAAM involves three main steps: process planning, deposition, and post processing. For a given CAD model, 3D slicing and programming software generates the desired robot motions and welding parameters for the deposition process, aimed at producing defect-free fabrication with high geometrical accuracy [22, 23, 34]. Based on the welding deposition model for the specific material being used to fabricate the component, the 3D slicing and programming software offer automated path planning and process optimization to avoid potential process-induced defects [35-38]. During fabrication, the robot and external axis provide accurate motion for the welding torch to build up the component in a layer-by-layer fashion. Advanced WAAM systems can be equipped with various sensors to measure welding signals [39], deposited bead geometry [40], metal transfer behaviours[41] and interpass temperature[33, 42, 43], thereby supporting in-process monitoring and control to achieve higher product quality. This is an area of current and future research interest, with

the potential for significantly improving WAAM process performance.

2.2 Metals used in WAAM process

WAAM processes use commercially available wires which are produced for the welding industry and available in spooled form and in a wide range of alloys as feedstock materials. **Table 2-2** indicates the commonly used alloys and their various applications in WAAM. Manufacture of a structurally sound, defect free, reliable part requires an understanding of the available process options, their underlying physical processes, feedstock materials, process control methods and an appreciation of the causes of the various common defects and their remedies. This section reviews the metals that are commonly used in WAAM, with a particular emphasis on the microstructure and mechanical properties of the additively manufactured alloys.

Table 2-2 Metals typically used with WAAM process

Applications	Alloys				
	Ti-based	Al-based	Steel-based	Ni-based	Bimetallic
Aerospace	[26]	[44]	-	[45]	[46]
Automotive	-	[47]	[48]	-	[49]
Marine	[50, 51]	-	[52]	-	-
Corrosion resistance	[53]	-	-	[54]	[55]
High temperature	[56]	-	-	[57]	[58]
Tools and molds	-	-	[59, 60]	-	-

2.2.1 Titanium alloys

Titanium alloys have been widely studied for application of additive manufacturing in aerospace components due to their high strength-to-weight ratio and inherently high material

cost. There are increasing demands for more efficient and lower cost alternative to the conventional subtractive manufacturing methods, which suffers very low fly-to-buy ratios for many component designs. There exists many business opportunities for the WAAM process, particularly for large-sized titanium components with complex structures [26].

It is well accepted that the microstructure of the product depends on its thermal history during the fabrication process. The distinctive thermal cycle, which involves an alternating heating and cooling [61, 62], produces meta-stable microstructures and inhomogeneous compositions in the fabricated part[63]. For example, Baufeld et al [62] investigated the microstructures of Ti6Al4V fabricated using a GTAW-based WAAM system, and found two distinctive regions on the as-build wall. In the bottom region, where alternating bands are perpendicular to the build direction, a basket Widmanstätten structure with α phase lamellae is present, while in the top region, where no such bands appear, needle-like precipitate is the main structure. Similar microstructural evolution has also been observed in PAW-based process. Lin, et al [64, 65] reported a graded microstructure along the build direction and identified the martensite α' structure, Widmanstätten structure and basket-wave structure from the bottom to the top region of the fabricated component, as shown in **Figure 2-2.** An epitaxial growth of β grains with discrete direction is also observed along the build direction owing to thermal gradient [66], commonly seen in additively manufactured titanium alloy components.

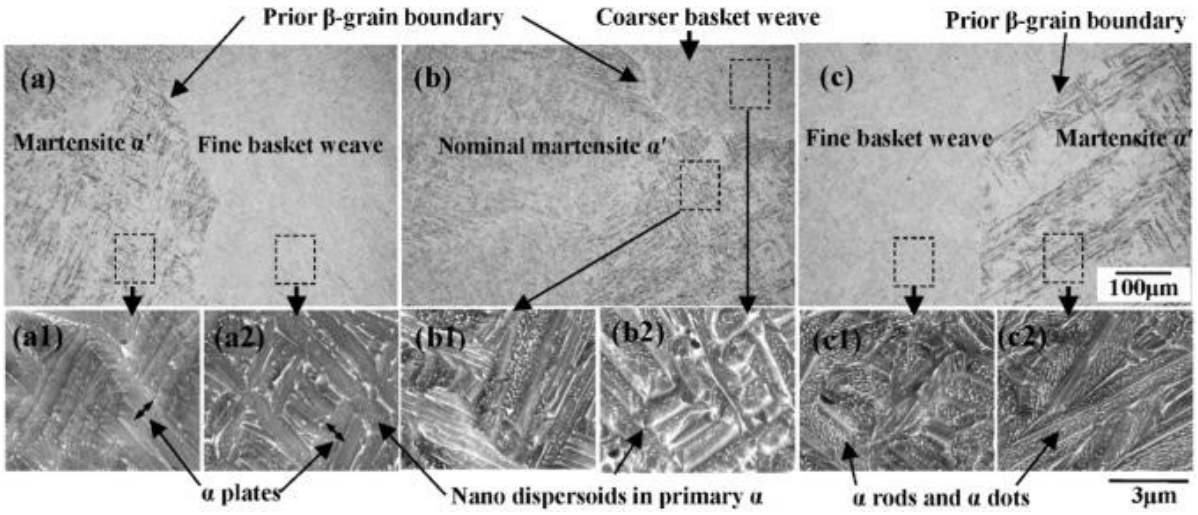

Figure 2-2 Optical microstructure of the deposited wall (from Lin, et al.[64]): (a) the bottom region; (b) the middle region; (c) the top region.

Table 2-3 summarizes the microstructure and mechanical property data (tensile strength, yield strength and elongation) of Ti6Al4V samples fabricated using various WAAM technologies [62, 64, 67-73]. The as-forged and as-cast minimum specifications from ASTM standards are also listed for comparison. As shown in **Figure 2-3**, the tensile property of asfabricated Ti6Al4V samples is close to that of wrought Ti6Al4V and exceeds that of cast Ti6Al4V as specified by ASTM standards. In addition, WAAM fabricated Ti6Al4V samples show anisotropic properties with lower strength and higher elongation values in the build direction (Z) compared to deposition direction (X), which is mainly attributed to the grain size of α lamellae and the orientation of the elongated prior β grains.

Table 2-3 Mechanical properties of titanium alloys fabricated from various WAAM processes

Process	Condition	Microstructure	YS[MPa]	UTS[MPa]	EL[%]	Reported by
Cast	/	/	758	860	>8	ASTM F1108
Wrought	/	/	860	930	>10	ASTM F1472
GTAW	AF	Columnar prior β grains + Widmanstätten α/β	/	929 ± 41[a] 965 ± 39[b]	9±1.2[a] 9±1[b]	Baufeld et al. [13]
	AF	α phase lamella basket weave structures	/	939 ± 24[a] 1033 ±32[b]	16 ± 3[a] 7.8 ± 2.3[b]	Baufeld et al.[67]
	HT (600°C/4h/FC)	lamellar structure	/	972 ± 41[a] 977± 14[b]	12.5 ± 2.5[a] 6 ± 3[b]	
	HT (834°C/2h/FC)	lamellar structure	/	931 ±19[a] 971 ± 28[b]	21 ± 2[a] 14 ± 2[b]	
	AF	Widmanstätten α + banded coarsened lamella α	803 ± 15[a] 950 ± 21[b]	918 ±17[a] 1033 ±19[b]	14.8[a] 11.7[b]	Wang et al.[74]
	AF	/	861 ± 14[a] 892 ± 31[b]	937 ± 21[a] 963 ± 22[b]	16.5 ± 2.7[a] 7.8 ± 2[b]	Brandl et al.[71]
	HT (600°C/2h/FC)	/	891 ± 16[a] 915 ± 14[b]	976 ± 35[a] 981 ± 8[b]	11.6 ± 2.4[a] 6.6 ± 2.6[b]	
	AN(834°C/2h/FC)	/	856 ± 21[a] 893 ± 24[b]	931 ± 17[a] 962 ± 29[b]	20.4 ± 1.8[a] 13.5 ± 2[b]	
Plasma	AF 600°C / 840°C	Widmanstätten α/β + Columnar β grains	/	/	/	Martina et al.[75]
Pulsed-PAM	AF	Prior columnar β + Martensite α'	909 ±13.6[b]	988±19.2[b]	7±0.5[b]	Lin et al.[65]
PAM	AF	Prior columnar β + martensite α'+ fine basket-weave structure	877 ± 18.5[b]	968 ± 12.6[b]	11.5 ± 0.5[b]	Lin et al. [64]

AF: as fabricated, HT: heat treated, AN: annealed; a: In build direction, b: Orthogonal to build direction;

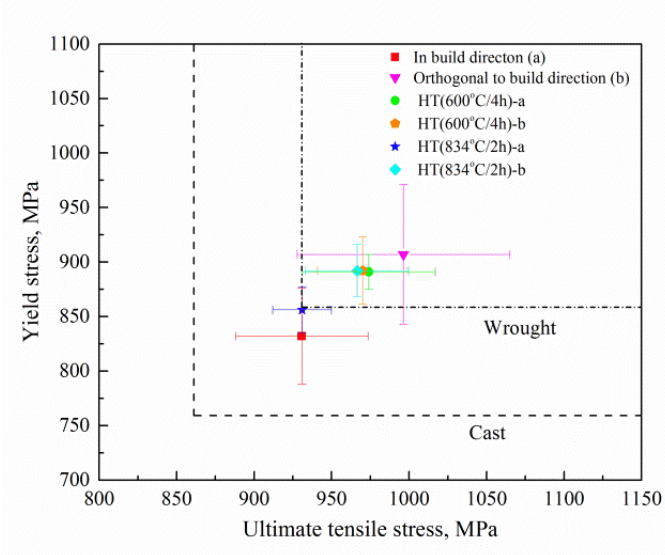

(a)

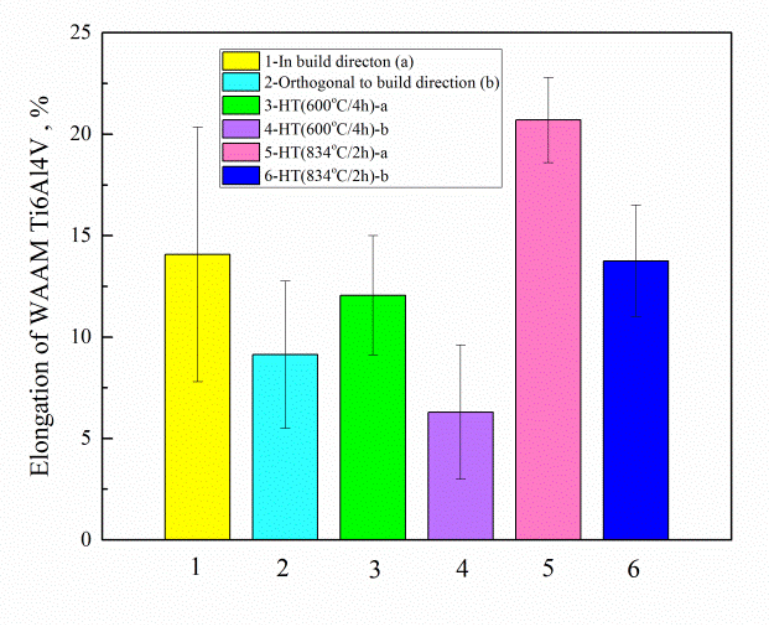

(b)

Figure 2-3 Mechanical property comparison for Ti6Al4V parts fabricated using WAAM: (a) yield and ultimate strength, (b) elongation.

2.2.2 Aluminum alloys and steel

Although fabrication trials for many different series of aluminum alloys, including Al-Cu (2xxx)[76], Al-Si (4xxx)[77] and Al-Mg (5xxx)[41] have been successfully carried out, the commercial values of WAAM is mainly justifiable for large and complex thin-walled structures, since cost of manufacturing small and simple aluminum alloy components using conventional machining processes is low[78]. Using WAAM to fabricate steel is unpopular for the same reason although it is the most commonly used engineering material[79]. Another reason for the poor commercial application of WAAM in aluminium is that some series of aluminum alloys, such as Al 7xxx and 6xxx, are challenging to weld[80] due to turbulent melt pool and weld defects, which frequently occur during the deposition process.

In general, as-deposited additively manufactured aluminum alloy parts have inferior mechanical properties compared to those machined from billet material. In order to achieve

higher tensile strength, most of the as-deposited aluminum parts undergo post-process heat treatment to refine the microstructure. **Table 2-4** lists the yield strength (YS), ultimate tensile strength (UTS), and elongation of WAAM-fabricated 2219 aluminium alloy samples. Due to the uniform distribution of large diamond particles within the microstructure, the sample exhibits lower UTS and YS than that of the wrought part specified by ASTM standard. However, after heat treatment, significant improvement beyond ASTM standard can be observed in both strength and elongation as a consequence of the grain refinement [44].

Table 2-4 Tensile properties of WAAM-fabricated aluminium alloy (2219)

Materials	Process	Condition	Microstructure	YS[MPa]	UTS[MPa]	EL[%]	Reported by
Al6.3Cu	Wrought(2219)	T851	/	267	390	> 4	ASTMB211M[81]
	CMT	AF	Fine dendrites + equiaxed grains	128 ± 2^a 133 ± 5^b	262 ± 4^a 264 ± 2^b	15.8 ± 0.3^a 18.6 ± 1.5^b	Gu et al. [44]
		HT(T6)	Homogeneous dispersed θ precipitates	305 ± 6^a 333 ± 6^b	458 ± 3^a 466 ± 3^b	13.6 ± 0.9^a 14^b	

AF: as fabricated, HT: heat treated; a: In build direction, b: Orthogonal to build direction;

2.2.3 Ni-based superalloys

Ni-based superalloys are the second most popular material studied by the additive manufacturing community research community after titanium alloys, mainly due to their high strengths at elevated temperatures and high fabrication cost using traditional methods. Nickel-based superalloys are widely applied in aerospace, aeronautical, petrochemical, chemical and marine industries due to their outstanding strength and oxidation resistance at temperature above 550 °C. To date, various Nickel-based superalloys, including Inconel 718 and Inconel 625 alloy have been studied after WAAM processing.

The microstructure of WAAM fabricated Inconel 718 parts generally consists of large

columnar grains with interdendritic boundaries delineated by small Laves phase precipitates and MC carbides[82]. Xu et al. [83] reported that columnar dendrite structures decorated with a large amount of Laves phase, MC carbides and Ni_3Nb are also present in WAAM-fabricated Inconel 625 parts, as shown in **Figure 2-4**. It is worth noting that the microstructure can be refined to smaller dendritic arm spacing, less niobium segregation and discontinuous Laves phase in the interdendritic regions using post-process heat treatments, which are beneficial to the mechanical properties.

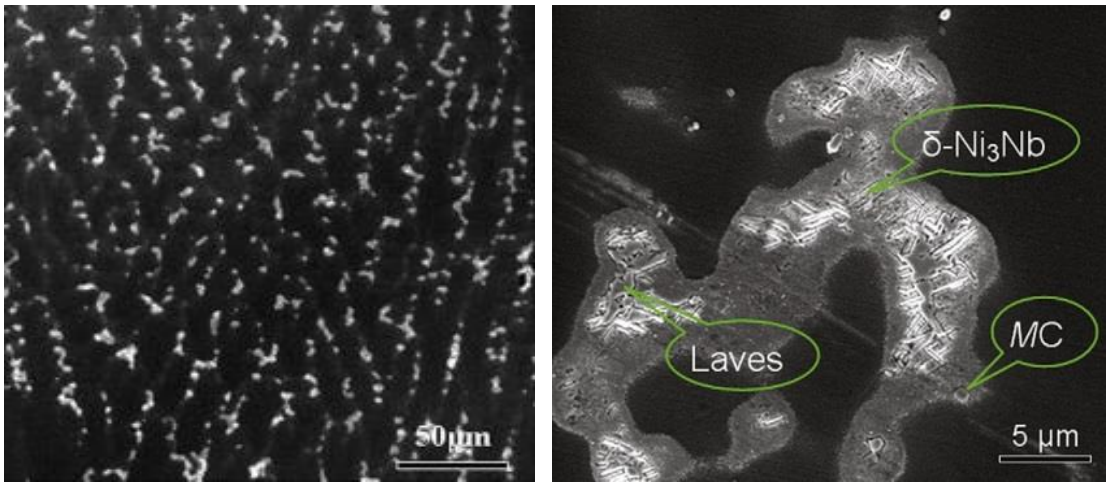

Figure 2-4 The major phases appearing in the as-deposited microstructure of Inconel 625 alloy (from Xu et al. [83]).

Table 2-5 lists the mechanical properties of several Nickel-based superalloys fabricated using the WAAM process. For GMAW-based WAAM-fabricated Inconel 718 alloy, the yield and ultimate tensile strength is 473 ± 6 MPa and 828 ± 8 MPa respectively. These values lie between the minimum values specified by ASTM for wrought and cast materials, whereas the elongation is much lower than the standards for both wrought and cast conditions. As for WAAM-fabricated Inconel 625 alloy, the YS, UTS and elongation all meet the requirement

set by ASTM for cast materials and are slightly lower than those for wrought material.

Table 2-5 Mechanical properties of various Ni-based superalloys using different WAAM processes

Materials	Process	Condition	Microstructure	YS[MPa]	UTS[MPa]	EL[%]	Reported by
IN 718	GMAW	AF	Nb precipitates + dendritic structure	473 ± 6	828±8	28 ± 2	Baufeld. [82]
IN 625	Cast	/	/	350	710	48	ASM[84]
	Wrought	/	/	490	855	50	ASM[84]
	PPAM	AF	Laves phase + columnar dendrite structure	438 ± 38[a] 423 ± 22[b]	721 ± 32[a] 718 ± 19[b]	48.6[a] 49.2[b]	Xu et al. [83]
	PPAW	AF	Laves phase + MC carbides + δ-Ni_3Nb	449	726	43	Xu et al. [85] Xu et al. [85] Wang et al. [86]
	PPAW	IC	Laves phase + NbC carbides	480	771	50	
	GTAW	HT(980°C /STA)	Coarser Laves particles + Nb precipitates	469	802	42	
	CMT	AF	Nb,Mo precipitates + dendrite structure	/	684± 23[a] 722 ± 17[b]	40.13 ±3.7[a] 42.27±2.4[b]	Ding et al. [87]
NiAlCu	CMT	AF	Widmanstätten α + martensite	350 ± 17	667 ± 15	29 ± 2.6	Ding et al. [87]

AF: as fabricated, HT: heat treated, IC: interpass cooling, STA: direct aging;
a: In build direction, b: Orthogonal to build direction,

2.2.4 Other metals

Other metals have also been investigated for potential fabrication using WAAM, such as magnesium alloy AZ31 for automotive applications[88], Fe/Al intermetallic compound [89, 90] and Al/Ti [91, 92] compound, as well as bimetallic steel/nickel [93] and steel/bronze [94] parts for aeronautic industry,. The detailed mechanical properties of these materials fabricated using WAAM are listed in **Table 2-6**. Most of this research has focused on determining the microstructural and mechanical properties of samples taken from simple straight-walled structures, rather than developing a process to fabricate functional parts. Manufacturing

intermetallic parts with accurate pre-designed composition still poses major challenges for the WAAM process.

Table 2-6 Mechanical properties of other metallic materials fabricated using WAAM process

Materials	Process	Condition	Microstructure	YS[MPa]	UTS[MPa]	EL[%]	Reported by
Ti/Al	GTAW	AF	Interdendritic γ structures + fully lamellar colonies	424 ± 30[a] 474 ± 17[b]	488 ± 50[a] 549 ± 23[b]	0.35[a] 0.5[b]	Ma et al. [24]
		HT(1200°C/24h)	Full γ microstructure	425 ± 15[a] 471 ± 14[b]	412 ± 11[a] 472 ± 11[b]	1.1[a] 1.1[b]	
		HT(1060°C/24h)	Fully lamellar structure	487 ± 14[a] 486 ± 12[a]	569 ± 12[a] 590 ± 4[b]	0.30[a] 0.45[b]	
Cu/Al	GTAW	AF	copper twinning	63 ± 2.1[a]	231 ± 2.5[a]	63 ± 4.0[a]	Dong et al. [95]
Fe/Al	GTAW	AF	Columnar Fe_3Al grains	847 ± 2[b]	944 ± 19[b]	3.2 ± 0.1[b]	Shen et al. [89]
Fe/Ni	GMAW	AF	austenite , δ-ferrite in low part; dendritic in up part	/	565±15[a]	/	Takeyuki et al. [93]
Fe/Cu	GMAW	AF	the mixture of α-Fe and ε-Cu	/	305[a]	48.5	Liu et al. [94]

AF: as fabricated, HT: heat treated; a: In build direction, b: Orthogonal to build direction.

2.3 Common defects in WAAM-fabricated component

Although the mechanical properties of components fabricated by WAAM are in many cases comparable to those of their conventionally processed counterparts, there are however some AM processing defects that must be addressed for critical applications. Porosity, high residual stress levels, and cracking, must be avoided, particularly for parts exposed to extreme environments where these defects lead to failure modes such as high temperature fatigue. Defects in WAAM can occur for various reasons, such as poor programming strategy, unstable weld pool dynamics due to poor parameter setup, thermal deformation associated with heat accumulation, environmental influence (such as gas contamination) and other machine malfunctions. As shown in **Figure 2-5**, certain materials tend to be vulnerable to

specific defects. For example, severe oxidization for titanium alloys, porosity for aluminum alloys, poor surface roughness in steel as well as severe deformation and cracks in bimetal components have been found to typically occur. **Table 2-7** lists the major defects that are commonly present in components fabricated using current WAAM techniques. The details of these common defects and their relationship to the materials will be discussed this section.

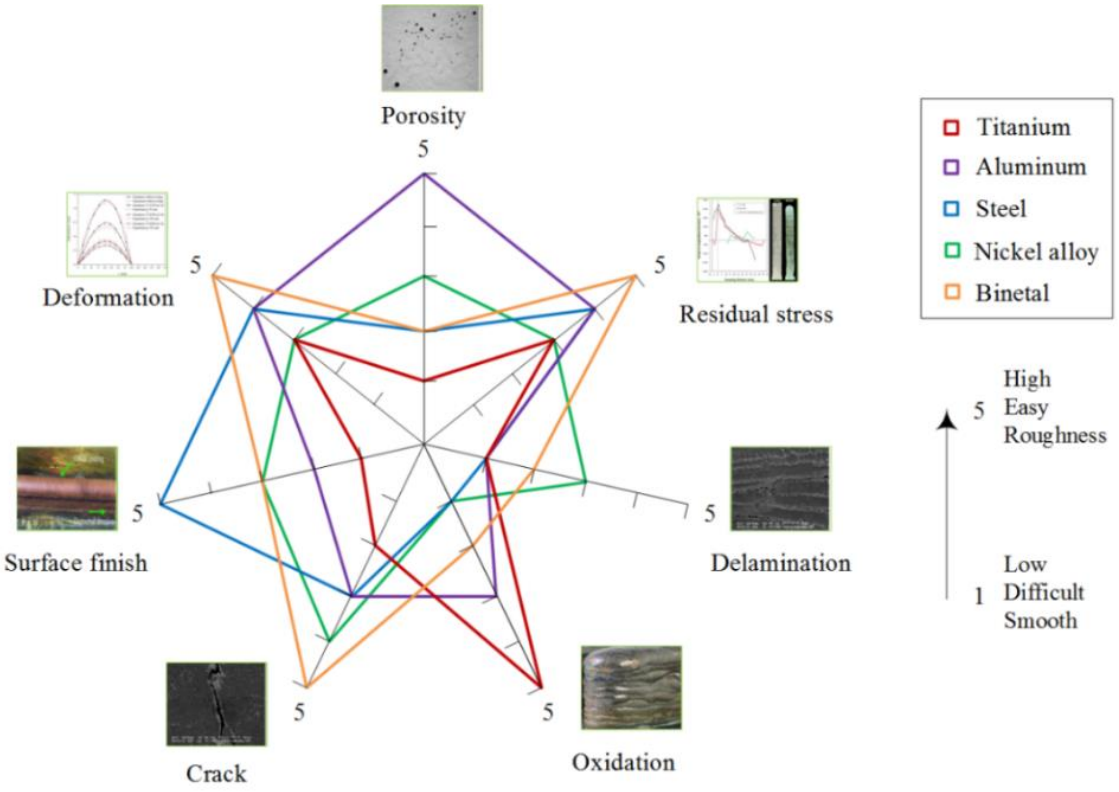

Figure 2-5 The correlation between materials and defects in WAAM process.

Table 2-7 Tendency of various defects in WAAM fabricated parts

Material	Process	Defect of feature						Ref.
		Porosity	Cracking	Delamination	Oxidation	Substrate adherence	Surface finish	
Ti6Al4V	TIG	No	No	No	Light	Good	Smooth	[13]
	Plasma	No	No	No	No	Good	Smooth	[75]
	CMT	No	No	No	Light	Good	Smooth	[96]
	DCEP-GMAW	No	No	No	Light	Medium	Poor	[96]
H08Mn2Si steel	DE-GMAW	low	No	No	No	Good	Waviness	[18]
Copper-coated steel	GMAW	No	No	No	Light	Good	Medium-rough	[97]
ER4043 Al alloy	CMT	High	No	No	Light	Good	Smooth	[77]
	VP-GTAW	No	No	No	No	Good	Medium-rough	[98]
AA2319 Al alloy	CMT	High	No	No	No	Good	Smooth	[99]
	CMT-PADV	No	No	No	No	Good	Smooth	[99]
5356 Al alloy	VP-GTAW	No	Yes	No	No	Good	Smooth	[100]
Inconel 625	PPAD	High	Yes	No	No	Good	Smooth	[83]
	GTAW	No	No	No	No	Good	Smooth	[101]
Inconel 718	GMAW	Medium	Yes	Yes	No	Good	Smooth	[14]
AZ31 Mg alloy	PMIG	No	No	No	Light	Medium	Medium-rough	[88]
Nickel-Al-Cu	CMT	No	No	No	No	Good	Smooth	[87]
Steel–bronze bimetal	GMAW	No	No	No	No	Good	Smooth	[94]
Steel- nickel bimetal	GMAW	No	No	No	No	Good	Medium-rough	[93]
Intermetallic Fe/Al	GTAW	High	Yes	No	Serious	Medium	Medium-poor	[90]
Intermetallic Al/Ti	GTAW	Low	Yes	No	No	Good	Rough	[24]
Intermetallic Al/Cu	GTAW	No	No	Yes	Light	Poor	Rough	[102]

2.3.1 Deformation and residual stress

Like other additive manufacturing process, distortion and residual stress are inherent to the WAAM process and it is impossible to completely avoid its generation. The residual stress can lead to distortion of the part, loss of geometric tolerance, delamination of layers during deposition, as well as deterioration of fatigue performance and fracture resistance of the additively manufactured components. Therefore, control and minimization of deformation and residual stress is a key area if research.

Various types of deformation appear in WAAM fabricated parts, including longitudinal and transvers shrinkage, bending distortion, angular distortion and rotational distortion [103]. The distortions are caused by thermal expansion and shrinkage of the part during repeated melting and cooling processes, which is particularly an issue for large thin walled structures [104]. Residual stress is the stress that remains in the material when all external loading forces are removed. If the residual stress is sufficiently high, it can be a critical influential factor in the mechanical properties and fatigue performance of the fabricated component. If the residual stress exceeds the local UTS of the material, cracking will take place, while if it is higher than the local YS but lower than UTS, warping or plastic deformation will occur [105]. Ding et al. [33] found that the residual stress uniformly distributes across the WAAM deposited wall, and the residual stress in the preceding layer has little effect on the future layers. After release of clamping, however, the internal stress is redistributed with a much lower value at the top of integral part than at the interface to the substrate, resulting in bending distortion of the component. Path planning also involves the distortion and residual stress evolution in WAAM process. If appropriate deposition path designs, it will help in the significant improvement in these defects, especially in large metal fabrication. A detailed overview of the residual stress origin would exceed the scope of this article.

Among all WAAM engineering materials, bimetal components exhibit high levels of residual stress and deformation due to the material thermal expansion difference. Hence, accurate interpass temperature control is needed when bimetal materials are used. WAAM-fabricated Inconel alloy has comparatively lower residual stresses levels, but it is more susceptible to process defects such as delamination, buckling and warping, since its

residual stress is usually higher than the yield stress [106]. Other comparatively softer materials, such as aluminum alloys, easily respond to deformation defects due to their high thermal expansion coefficients. A better understanding pf the effect of material characteristics in WAAM processing is needed for controlling residual stress and deformation during deposition.

Deformation and residual stress are associated with many process parameters, such as welding current, welding voltage, feeding speed, ambient temperature, shielding gas flow rate, etc. There is still a lack of systematic methods for controlling defects through optimized selection or manipulation of these parameters. Fortunately, several post-process treatments that have been proven to effectively mitigate residual stress and deformation, and these will be discussed in later section.

2.3.2 Porosity

Porosity is another common defect in WAAM processing that needs to be minimized due to adverse effects on mechanical properties [107]. Firstly, porosity will lead to a component with low mechanical strength by damage from micro-cracks, and secondly, it usually brings low fatigue property to deposition via spatially with different size and shape distribution. In general, this type of defects are mainly classified as either raw material-induced [108] or process-induced[109].

The WAAM raw material, including as-received wire and substrate, often has a degree of surface contamination, such as moisture, grease and other hydrocarbon compounds that may be difficult to completely remove. These contaminants can be easily absorbed into the

molten pool and subsequently generate porosity after solidification. Among common engineering materials, aluminum alloy is the most susceptible to this defect as the solubility of hydrogen in solid and liquid (0.036 against 0.69 cm3/100 g at a melting point of 660℃, respectively) is significantly different [110]. Even small amounts of dissolved hydrogen in the liquid state may exceed the limit of solubility after solidification, resulting in porosity [111]. Therefore, the cleanliness of raw materials is critical, especially for aluminum alloys.

Process-induced porosity is usually non-spherical, and mainly caused by poor path planning or an unstable deposition process. When the deposition path is complex, or the manufacturing process is changeable, insufficient fusion or spatter ejection is easily produced, creating gaps or voids in these influenced regions.

To control porosity, the following methods can be adopted: (1) an AC GMAW-based process or CMT-PADV based process (cold metal transfer pulsed advanced, a controlled short-circuiting GMAW transfer process) is preferred, especially for aluminum; (2) the highest quality shielding gas, tight gas seals, non-organic piping and short pipe lengths are highly recommended; (3) the wire and substrate surfaces are as clean as possible before fabrication; (4) high quality feedstock should be used; (5) the deposited bead shape needs to be optimized; (6) the thermal profile during processing should be monitored and controlled; (7) post-deposition treatment, such as interpass rolling can be applied.

2.3.3 Crack and delamination

Similar to residual stress and deformation, cracking and delamination not only involves the thermal signature of the manufacturing process, but also relates to the material characteristics of the deposit. Ordinarily, the crack is categorised as either a solidification

crack or grain boundary crack within the WAAM component [105]. The former type of crack depends mainly on the solidification nature of the material and is usually caused by the obstruction of solidified grain flow or high strain in the melt pool [112]. Grain boundary cracking often generates along the grain boundaries due to the differences between boundary morphology and potential precipitate formation or dissolution [113]. Delamination or separation of adjacent layers takes place due to incomplete melting or insufficient re-melting of the underlying solid between layers. Generally, this deficiency is visible and cannot be repaired by post-process treatment. In order to prevent this defect, preprocess treatment such as preheating of the substrate needs to be considered.

Bimetal material combinations, such as Al/Cu, Al/Ti and Al/Fe, are quite susceptible to cracking and delamination when fabricated with the WAAM process. The dissimilar metals have large differences in their mutual solubility and chemical reactivity so that the intermetallic phase-equilibrium is freely broken, thus inducing crack growth along grain boundaries. Also, Inconel alloy readily generates solidification cracking issues due to the existence of liquid film at terminal solidification [101]. Both of these material types should receive particular attention to avoid cracking and delamination.

To control crack defects, corresponding measures can be taken as follows: (1) Mixed wires and optimization of their compositions; (2) Decrease the cooling rate during the deposition process (3) Other measures to improve strength rather than solution treatment.

2.4 Current methods for quality improvement in WAAM process

Generally, WAAM parts require post-process treatment to improve material properties, reduce surface roughness and porosity, and remove residual stress and distortions. By

appropriate application of post process, the majority of issues that influence deposition quality can be mitigated or eliminated. Presently, several post-process treatment technologies have been reported to improve part quality in the WAAM process. This section will review these post-process techniques, both their features and limitations.

2.4.1 Post heat treatment

Post-process heat treatment is widely used WAAM to reduce residual stress, enhance material strength and as a method of hardness control. The selection of a suitable heat treatment process depends on additive the target material, additive manufacturing methods, working temperature and heat treatment conditions. If the heat treatment state is set incorrectly, the probability of cracking will increase under mechanical loading, as the combination of existing residual stress with load stress exceeds the material's design limitation.

As summarized above, after heat treatment, the mechanical strength of WAAM-fabricated parts improved significantly, with increase of 4%, 78%, 5% and 17% being reported for titanium alloy, aluminum alloy, Nickel-based superalloys and intermetallic Ti/Al alloy, respectively. In addition, post-process heat treatment plays an important role in grain refinement, especially for WAAM-fabricated aluminum and Inconel alloy [67].

The decision to use post-process heat treatment depends on the material alloying system and also the pre-heat treatment state. Generally, high carbon content materials must be heat treated, while a few materials can be damaged by this technique. Therefore, the utilization of post heat treatment process to WAAM component needs to consider the specific material and its application.

2.4.2 Interpass cold rolling

Rolling of the weld bead between each deposited layer has been shown to reduce residual stresses and distortion [114]. Interpass cold rolling not only lowers residual stress, but also brings more homogeneous material properties. In the WAAM process, the thermal gradient with deposition layers and alternate re-heating and re-cooling process result in the target part having anisotropic microstructural evolution and mechanical properties. The cold rolling technique significantly reduces microstructural anisotropy through plastically deforming the deposition. **Figure 2-6** shows the schematic diagram of an interpass cold rolling system developed at Cranfield University. A slotted roller is used o refine the microstructure and enhance tensile strength in the longitudinal direction by supporting external force [115, 116]. As shown in **Table 2-8**, both ultimate tensile strength and yield strength in the build direction were improved through interpass cold rolling, which contributes to more homogeneous material properties in the target component.

Interpass cold rolling also can play a critical role in the healing of hydrogen porosity in WAAM-fabricated aluminum parts. Generally, high dislocation density is produced by the rolling process. These dislocation can act as preferential sites for atomic hydrogen absorption [117] and as well as ‘pipes’ for the hydrogen, allowing to diffuse to the surface [118]. **Table 2-9** summarizes the outcomes documented in the literature, in terms of the pore incidence and size distribution in aluminum components fabricated using WAAM with interpass cold rolling. The porosities existing in as-fabricated component can be reduced or even eliminated when interpass cold rolling is applied [75].

This technique is only feasible for simple deposited parts, such as straight walls, due to

the geometrical limitation of the rolling process. For more complex components with curves and corners, special flexible tooling need to be developed to achieve an effective rolling process, thus limiting the range of industrial application. Cold rolling technique will also reduce residual stress, but the ability to reduce overall part distortion is yet to be proven [26, 119].

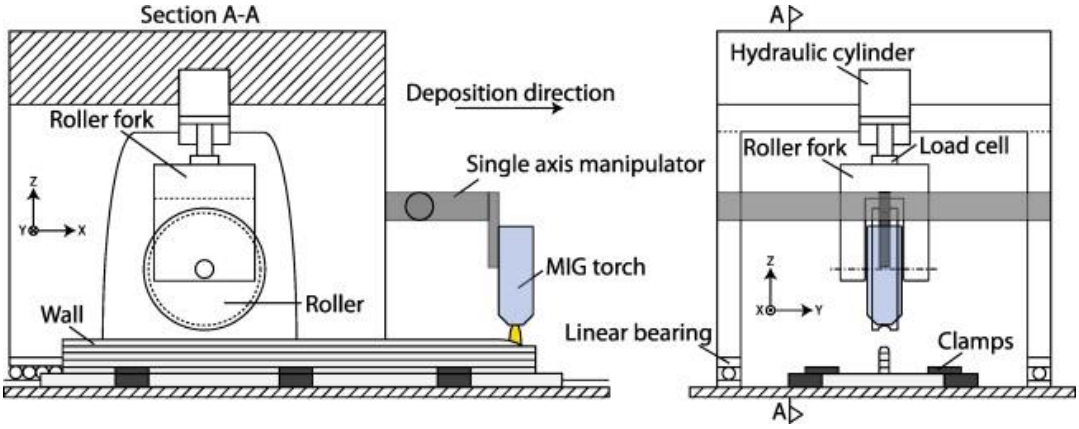

Figure 2-6 Schematic diagram of WAAM with cold rolling process [104]

Table 2-8 Material properties of component fabricated using WAAM with interpass cold rolling

Materials	Condition	Microstructure	YS[MPa]	UTS[MPa]	EL[%]	Hardness[HV]	Ref.
Ti6Al4V	AF	Widmanstätten α + Martensite	807 ± 2[a] 853 ± 10[b]	903 ± 3[a] 945 ± 6[b]	22.8 ± 0.2[a] 13.8 ± 1.2[b]	/	[114, 116, 120, 121]
	RL:50	Grain size decrease from average 200μm to 100μm	916 ± 22[a] 911 ± 11[b]	1022 ± 3[a] 1006 ± 5[b]	14.2 ± 1.3[a] 10.0 ± 0.5[b]	/	
	RL:75		993 ± 31[a] 1028 ± 5[b]	1078 ± 3[a] 1077 ± 18[b]	13.0 ± 1.0[a] 13.1 ± 1.8[b]	/	
Al 2319	AF	/	132	260	15.5	/	[120]
	RL:15		145	274	13	/	
	RL:30		190	288	10.3	/	
	RL:45		244	304	7.3	/	
AISI 301LN	AF	Austenite phase	292	697	54	220	[115]
	CR:20	transformed to α'-rnartensite + deformed austenite	750	1034	23	345	
	CR:40		1239	1321	6	456	
	CR:60		1529	1062	3	522	
	CR:80		1900	1925	2	610	
Al-6.3Cu	AF	Fine dendrites + equiaxed grains	128 ± 2[a] 133 ± 5[b]	262 ± 4[a] 264 ± 2[b]	15.8 ± 0.3[a] 18.6 ± 1.5[b]	68.3	[44]

	RL:15	With the increase load, the grain size is decreased with freeform deformation	142 ± 4[a] 146 ± 3[b]	270 ± 7[a] 271 ± 9[b]	14.6 ± 0.4[a] 15 ± 1.4[b]	77.4	
	RL:30		188 ± 4[a] 195 ± 2[b]	286 ± 3[a] 293 ± 6[b]	12 ± 0.6[a] 13.2 ± 0.2[b]	90.1	
	RL:45		241 ± 2[a] 249 ± 1[b]	312 ± 8[a] 323 ± 9[b]	7.4 ± 0.6[a] 8.6 ± 0.4[b]	102.3	

AF: as-fabricated; RL: Rolling loads (KN); CR: Cold reduction (%);
a: In build direction, b: Orthogonal to build direction.

Table 2-9 The distribution of porosity in aluminum part using WAAM with cold rolling.

Materials	Condition	Layers	Height (mm)	Deformation (%)	Number of pores (in area of 120 mm^2)	Pores diameter (mm)	Reported by
Al 2319	AF	21	49.4	/	614	13.5	Gu et al.[76]
	RL:15	25	50.6	13.9	192	12.5	
	RL:30	30	49.4	30.0	5	8.8	
	RL:45	38	49.8	44.2	Elimination	Elimination	
Al 5087	AF	30	49.5	/	454	25.1	
	RL:15	35	49.6	14.1	336	13	
	RL:30	45	51	31.3	11	9.6	
	RL:45	55	49.5	45.4	Elimination	Elimination	

AF: as-fabricated; RL: Rolling loads (KN);

2.4.3 Interpass cooling

Recently, interpass cooling has been developed and evaluated at the University of Wollongong. **Figure 2-7** presents the schematic diagram of a WAAM system with interpass cooling. The moveable gas nozzle, which supplies argon, nitrogen or CO2 gas, is used to provide active, or forced, cooling on the fabricated part during and/or after deposition of each layer. Using such rapid cooling, the in-situ layer temperature and heat cycle can be controlled within a range to obtain the desired microstructure and mechanical properties. This process may also potentially reduce residual stress and distortion, although this aspect has not been investigated.

An initial feasibility study shows promising results when using forced interpass cooling

with compressed CO2 to fabricate Ti6Al4V thin-walled structures, as shown in **Figure 2-8**. It was found that interpass cooling produces less surface oxidation, refined microstructure, improved hardness and enhanced strength. In addition, manufacturing efficiency is significantly improved due to the reduction of dwell time between deposited layers. More detailed research findings will be presented in future.

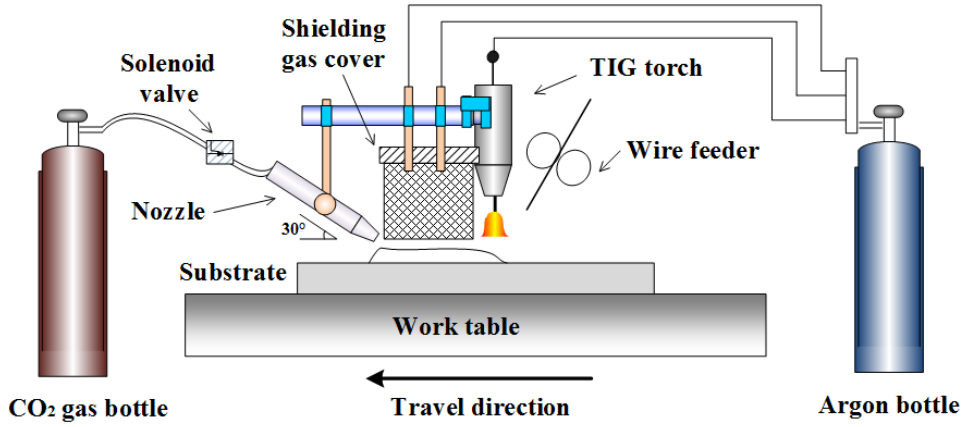

Figure 2-7 Schematic diagram of the combined WAAM gas cooling process

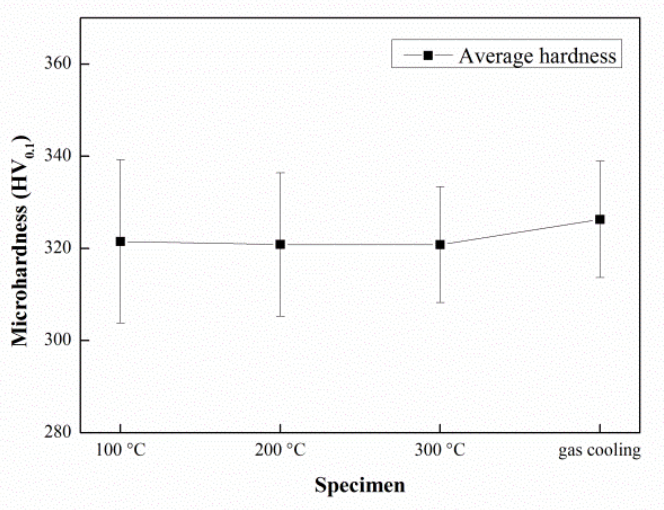

(a)

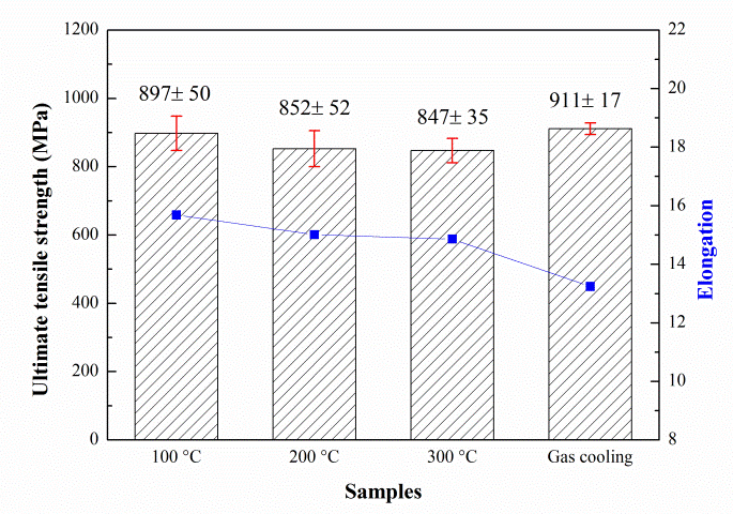

(b)

Figure 2-8 Mechanical properties of Ti6Al4V part produced by WAAM with interpass cooling using CO_2 gas:(a) Hardness; (b) Tensile strength and elongation

2.4.4 Peening and ultrasonic impact treatment

Peening and ultrasonic impact treatments (UIT) have been used in welding applications to reduce local residual stress and improve weld mechanical properties. Both techniques are cold mechanical treatments that impact the weld surface using high energy media to release tensile stress by imposing compressive stress at the treatment surface. Usually, the mechanical peening process produces compressive stresses at a limited depth below the component surface, such as around 1–2mm in carbon steels [122]. Ultrasonic impact treatment produces grain refinement and randomizes orientation, thus contributing to mechanical strength improvement. It is reported that after ultrasonic impact treatment, the surface residual stress of WAAM-fabricated Ti6Al4V part can be reduced to 58% and the microhardness can be increased by 28% compared to the as-fabricated sample. Also, the surface-modified layers undergo plastic deformation with significant grain refinement and dense dislocations [123]. The ultrasonic impact treatment is limited by penetration depth,

which is up to 60 μm below surface. Therefore, although both techniques are good post-process treatments, they have negligible effect on internal residual stresses of large metal part fabricated using WAAM.

2.5 Summary and scope of this work

A review of recent technology development in WAAM process is presented with a focus on the microstructure, mechanical properties, process defects and post-process treatment. In combination of materials characteristics and WAAM techniques features, a quality-based framework will be proposed in final section of this thesis, aiming to achieve high-quality and defect-free WAAM components.

Chapter 3 EXPERIMENTAL INSTRUMENTS AND METHODOLOGIES

In this chapter, the experimental instruments and methodologies used in the thesis will be briefly illustrated, and the details, such as experimental parameters, will be displayed in the following chapters.

3.1 Materials

The materials used in this study were commercial ASTM B863 grade 5 Ti-6Al-4V alloy wire with a diameter of 1.2mm and ASTM B265 grade 5 Ti-6Al-4V sheet with dimensions of 200 mm × 150 mm × 6 mm. The chemical composition is listed in **Table 3-1**.

Table 3-1 Chemical composition of Ti-6Al-4V (wt.%).

Composition	Al	V	C	Fe	H	N	O	Ti
Wire (ASTM B863)[124]	6.20	4.0	0.08	0.40	0.015	0.05	0.20	Bal.
Substrate (ASTM B265)[125]	6.10	4.0	0.08	0.30	0.015	0.03	0.20	Bal.

3.2 Experimental instruments

The apparatus used in this thesis mainly consists of a 200A-rated GTAW power source, “cold” wire feeder, water cooling unit and travel mechanism, as shown in **Figure 3-1**. A 150 mm long trailing gas shield was placed behind the GTAW torch to provide localized protection against oxidation during the cooling process.

(a)

(b)

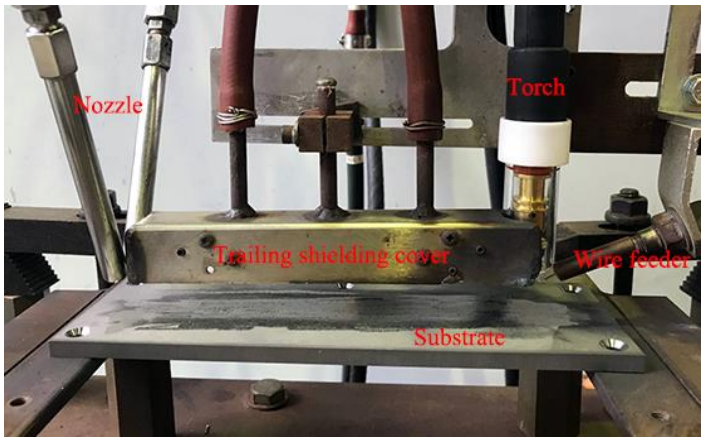

(c)

Figure 3-1 The apparatus used in this work: (a) 200A-rated GTAW power source; (b) wire feeder; (c) travel mechanism and trailing gas shield

3.3 Process monitoring

During manufacturing process, a high speed camera designed to record the dynamic arc and the metal transfer process at a frame rate of 1 kHZ, as shown in **Figure 3-2**. the AF-S NIKKOR 70-200mm*1:4 ED VR camera lense was used. The experimental data obtained from the high speed camera profiler was processed using MATLAB.

Figure 3-2 High speed camera used in this study

An infrared (IR) pyrometer system with an optical fiber was used to measure the temperature of the substrate and the deposited part during manufacturing, as shown in **Figure 3-3**. The temperature of the pyrometer system was read by the developed LabView software.

Figure 3-3 IR pyrometer used in this study

A 3D laser profile scanner with a resolution of 0.02 mm was adopted to measure the deformation of samples, as shown in **Figure 3-3**. To improve measurement accuracy which

involves random errors, each sample profile was scanned 200 times. The experimental data obtained from the laser profiler was processed using MATLAB.

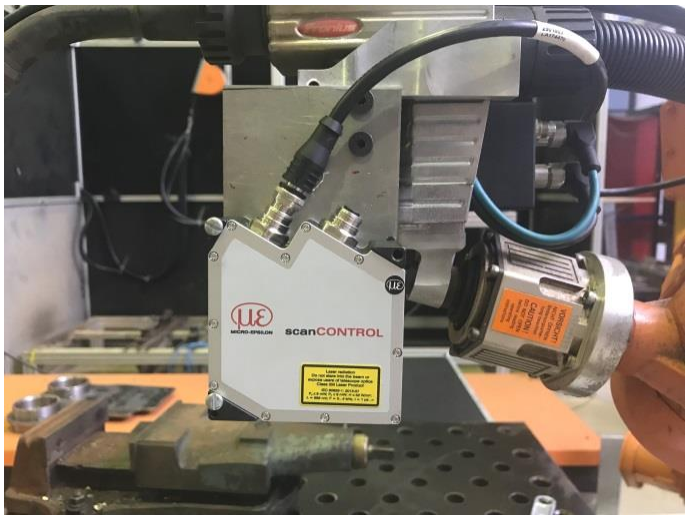

Figure 3-4 3D laser scanner used in this work

3.4 Metallography

After sample preparation, microstructural characterization of the specimens was carried out using stereo microscopy, optical microscopy (OM) and scanning electron microscopy (SEM). Chemical composition of precipitates was analysed by energy dispersive spectroscopy (EDS) detectors, which are attached to SEM.

3.4.1 Sample preparation for metallography

The specimens for microstructural observation (OM and SEM) were cut using a Wire Electrical Discharge Machining. Afterwards, these specimens were hot mounted with a CitoPress-20 hot mounting press (**Figure 3-5**), and then polished in a standard metallographic way by Struers automatic polisher Tegrapol 21 (**Figure 3-6**). The detailed grinding and polishing procedures are provided in Table 3-2. After that, the specimens were etched in

Kroll's reagent solutions that consist of 100ml distilled water (H2O), 5ml concentrated nitric acid (HNO3) and 3ml 3% hydrofluoric acid (HF).

Figure 3-5 Struers CitoPress-20

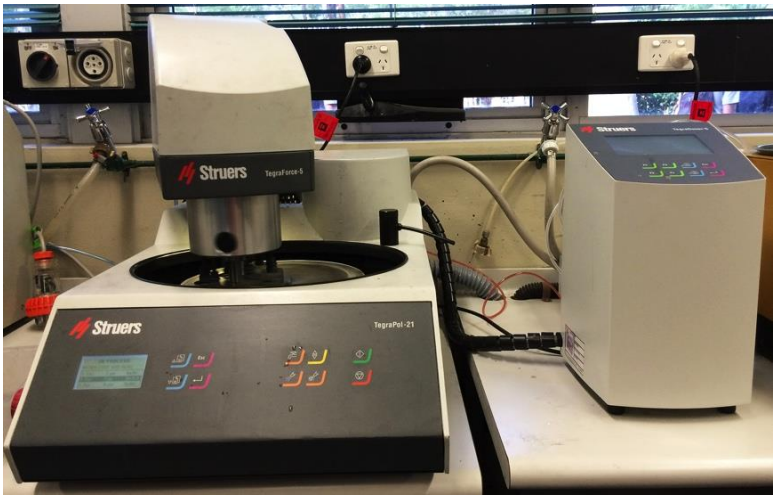

Figure 3-6 Struers Tegrapol-21

Table 3-2 Sample preparation procedures for microstructural analysis.

Procedure	Surface	Force, N	Time, minute	Solution
Grinding	1200# SiC paper	25	2	Water
Polishing	15μm MD-Pan cloth	25	15	Water-based lubricant
Polishing	0.25μm MD-Chem cloth	25	10	50% OPS

3.4.2 Stereo microscopy and optical microcopy (OM)

Based on visible light and a series of lenses, a Leica M205A stereo microscopy (**Figure 3-7**) was used to acquire images of cross-section of specimens and a Leica DMR optical microcopy (**Figure 3-8**) was used to magnify images. The horizontal and vertical section is for microstructure observation, including precipitation and grain size. The grain size was measured by the software of Image 2 using planimetric method.

Figure 3-7 Leica M205A stereo microscopy

Figure 3-8 Leica DMR optical microscopy

3.4.3 Scanning electron microscopy (SEM)

SEM is a type of electron microscope through scanning the surface of a sample with a focused beam of electrons. In this thesis, a JEOL 7500 operating SEM equipped with an energy dispersive X-ray spectrometer (EDS) was used to observe the fracture surfaces of tensile specimens, as shown in **Figure 3-9**. Atomic concentrations of precipitates were analysed by EDS if special composition of phase on fracture surfaces of specimens needs to be further confirmed.

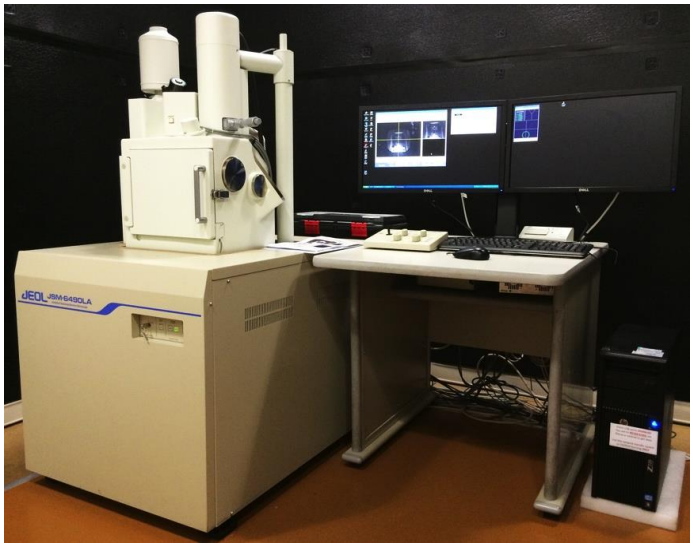

Figure 3-9 JEOL JSM-7500 SEM

3.4.4 X-ray diffraction (XRD)

X-ray diffraction (XRD) was used to determine the phase constitution of specimens. In this thesis, XRD testing was performed on a GBC MMA X-ray diffractometer using monochromatic Cu Kα radiation (wavelength λ = 1.5418Å) at an accelerating voltage of 35 kV and a current of 28.6 mA with a scanning step of 0.02º and a scanning speed of 4 º/min in the range of 30º ~ 90º, as shown in **Figure 3-10**.

Figure 3-10 GBC MMA X-ray diffractometer

3.5 Mechanical properties

Mechanical properties of the specimens were measured, focusing on tensile strength and hardness testing and aiming at evaluating the strength, hardness and ductility properties under different WAAM process.

3.5.1 Tensile testing

In this thesis, tensile tests were conducted using a MTS 370 (**Figure 3-11**) at room temperature. The ultimate tensile strength (UTS), yield strength (YS) and elongation were measured during test. The diagram of machined specimens for tensile testing is shown in **Figure 3-12**, and the detailed dimension data is listed in **Table 3-3**.

Figure 3-11 MTS370 tensile machine

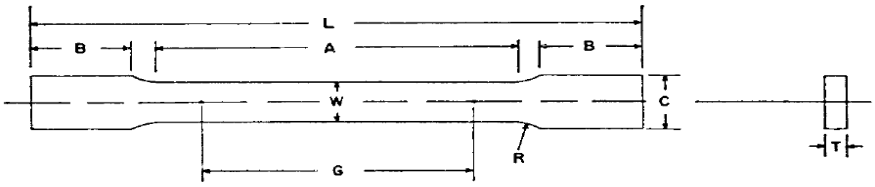

Figure 3-12 The diagram of machined tensile specimen.

Table 3-3 Dimensions for tensile specimen.

Standard specimens, Sheet-type	Dimension
G-gage length	10.0 ± 0.10 mm
W-Width	2.0 ± 0.25 mm
T-Thickness	1.5 mm
R-Radius of fillet, min	2.0 mm
L-Over-all length, min	34.0 mm
A-Length of reduced section, min	2.0 mm
B-Length of grip section, min	10.0 mm
C-Width of grip section, approximate	8.0 mm

3.5.2 Hardness testing

The Vickers hardness testing was performed on a Via-F Vickers innovative automatic tester (**Figure 3-13**) with a load of 0. 98 N and a dwell time of 10 s according to ASTM:

F2924 standard. Specimen preparation should be performed in accordance with standard guide for preparation of metallographic specimens. The corresponding results were presented graphically.

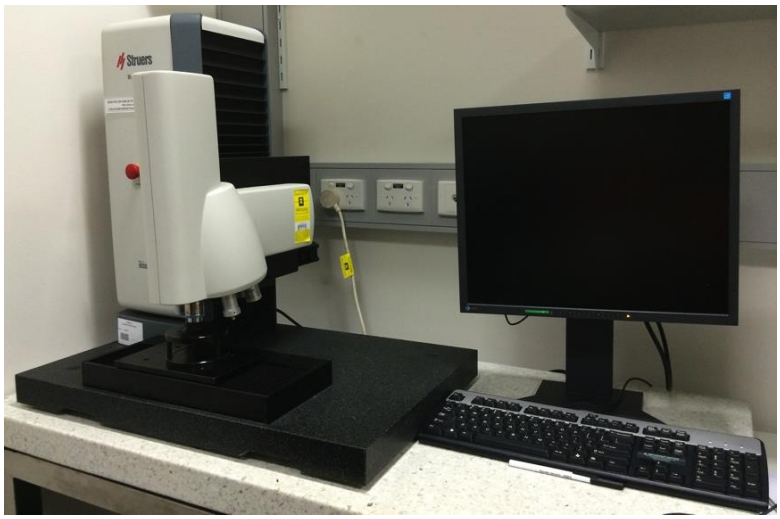

Figure 3-12 The Vickers innovative automatic testers

3.6 Corrosion resistance

The electrochemical corrosion tests were conducted on a CHI 600C electrochemical working station (manufactured by CH Instruments, Inc.) with a conventional three-electrode cell in 3.5 wt.% NaCl solution at room temperature. A platinum sheet and saturated calomel electrode (SCE) were used as counter electrode and reference, respectively, as shown in **Figure 3-14**.

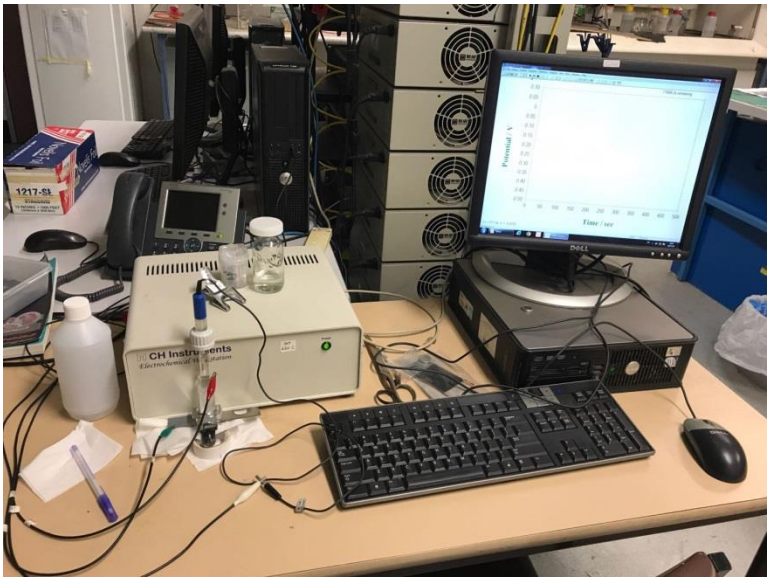

Figure 3-13 Electrochemical workstation

3.7 Summary

This chapter insulates the commonly used experimental instruments and methodologies in the thesis. The particular and detailed experimental procedures as well as experimental results will be presented and discussed in the relative chapters

Chapter 4 PROCESS STABILITY

4.1 Introduction

The heat accumulation is a critical factor that influences the stability of the WAAM process in terms of the geometrical accuracy, deposition defects, microstructural evolution and material properties of as-fabricated parts. Ma et al. [92] carried out an experiment in which a simple Ti-Al part was fabricated using GT-WAAM. It was found that the alpha phase fraction in the microstructure decreases by nearly threefold when the interpass temperature changes from 100℃ to 500 ℃, which results in a decrease in hardness values. Shen et al. [126]investigated the fabrication of Fe-Al materials using a similar WAAM process and reported that poorly controlled interpass temperature is likely to produce longitudinal cracking and high residual stress in the first few layers. In addition, considerable research has focused on arc stability and metal transfer behaviour of the WAAM process. Wang et al. [86]claims that during the arc-wire deposition process, the distance between the trailing end and center of molten pool was increased by 1.95 mm from 1st layer to 5th layer due to the increased heat accumulation. Similar results could also be found in earlier literature regarding the analysis of thermal behaviours during multi-layer rapid prototyping fabrication[127]. Another study conducted by Denlinger et al. [43] found that the distortion and residual stresses in as-fabricated titanium and nickel alloy parts were significantly affected by the inter-layer dwell time that is directly related to the thermal characteristics. Zhou et al. [128]developed a three-dimensional model to simulate the arc shape and metal transfer behaviours occurring in the WAAM process. The distribution of thermal conductivities and

molten pool characteristics for single-bead as well as overlap deposition were investigated. Their results show that the high temperature region of the molten weld pool for overlapping deposition is narrower than that of single-bead deposition, due to the smaller net heat flux of overlapping deposition. Although these simulation and experimental studies have provided some useful information, the underlying mechanisms of arc characteristics and metal transfer behavior associated with heat accumulation are still poorly understood due to the complexity of the WAAM process.

This section investigates the influence of heat accumulation on process stability during the fabrication of Ti6Al4V parts using GT-WAAM with localized gas shielding. The difference in temperature variations between the substrate and in-situ layers is discussed. The results provide insight into the way in which the interpass temperature is measured. Furthermore, the surface morphology, geometrical features, arc characteristics and metal transfer behaviours in different layers during deposition are compared to identify variation trend associated with heat accumulation. Although the research outcomes are not a direct physical explanation of the thermal mechanism, this section offers better understanding of the effects of heat accumulation on process stability of the wire arc additive manufacturing process, which will benefit further process optimization and control.

4.2 Experimental Procedures

4.2.1 Experimental setup

The GT-WAAM system used in this section, as shown in **Figure 4-1**. The wire filler was fed into the front of the weld pool at an angle of 60° to the GTAW torch, which produces a

stable metal transfer condition. Welding grade argon (99.995% purity) is used for both torch and trailing shield. A build wall was produced by depositing 15 passes on the as-received substrate plate. The main process parameters are listed in **Table 4-1**.

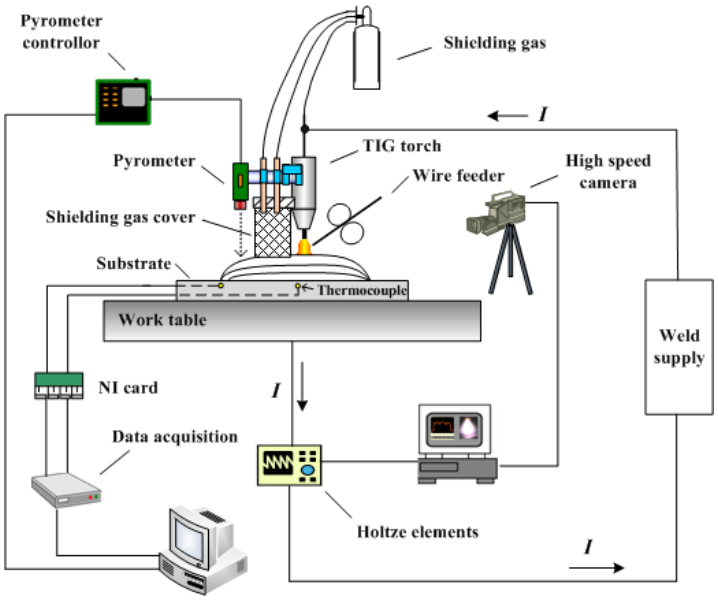

Figure 4-1 Schematic illustration of GT-WAAM process

Table 4-1 Process parameters for GT-WAAW

Process parameters	Details
Deposition current	110 A
Arc voltage	12 V
Travel speed	95 mm/min
Wire feed speed	1000 mm/min
Distance between the electrode and workpiece	3 mm
Angle between the electrode and the filler wire	60°
Flow rate of argon in GTAW torch	10 L/ min
Flow rate of argon in trailing shield	10 L/ min
Post flow shielding time	30 seconds
Dwell time between layers	180 seconds

4.2.2 Measurement of interpass temperature

Thermocouples and an IR pyrometer were used to measure the temperature of the substrate and the deposited part, respectively. **Figure 4-2a** shows the operating principle of

the measurement system. Two thermocouples were fixed on the substrate for monitoring the substrate temperature, and the IR pyrometer was positioned to measure the in-situ layer temperature immediately before deposition of the subsequent layer. The specific measurement locations are shown in **Figure 4-2b**.

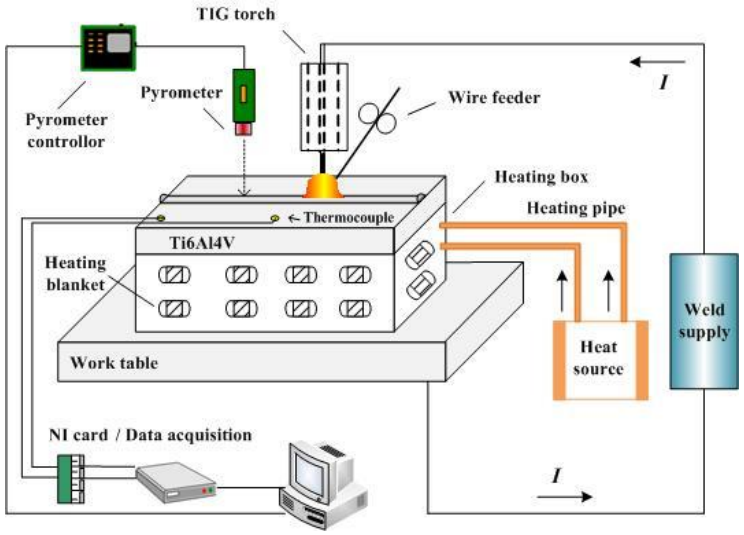

(a)

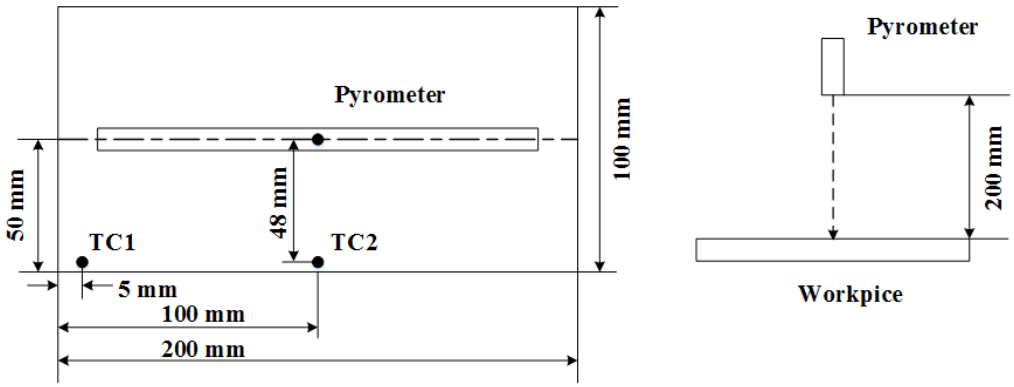

(b)

Figure 4-2 Schematic diagram of the temperature measurement system: (a) overall system (b) measurement locations for the pyrometer and thermocouples (TC)

The material emissivity was calibrated before using the infrared pyrometer since the emissivity of the material varies with bulk, surface roughness, oxidization, and especially with surface temperature, as reported by Hagqvist et al.[129]. The temperature (T_{IR}) from a

signal-wavelength IR pyrometer is expressed as[130]:

$$T_{IR} = \frac{CT}{C - \lambda T ln(\varepsilon F \gamma)} \tag{4-1}$$

where T is the nominal absolute temperature, ε is the emissivity of the material surface, F is the ratio of the capturing field of view of pyrometer, γ is the attenuation caused by the media (air) from sample to the pyrometer sensor, λ is the wavelength of the pyrometer, and C is the second radiation constant(C=1.4387 × 10^4 μm·K). For a small emissivity error, $\Delta\varepsilon$, the following expression describes the magnitude of the temperature error [130]:

$$\Delta T = \frac{\lambda T^2}{C} \cdot \frac{\Delta \varepsilon}{\varepsilon} \tag{4-2}$$

A number of calibration tests were carried out on a single deposited Ti6Al4V bead (smooth silver surface) that was continuously heated from 50 ℃ to 500 ℃, followed by natural cooling process back to room temperature, as shown in **Figure 4-3**. Two thermocouples were attached on the bead surface as the temperature reference for calibration. As no shielding gas was used during this calibration, slight discoloration due to oxidation on the Ti6Al4V bead surface was observed, which provides an appropriate simulation for the actual heating and cooling cycle during actual deposition. Through multiple tests, a constant emissivity of 0.45 was determined to minimize the temperature measurement errors due to small variation in emissivity compensation. **Figure 4-3** shows the temperature calibration curves from both pyrometer and thermocouples (actual temperature) with emissivity value set as 0.45. It can be seen that the relationship between temperature acquired from pyrometer and actual temperature can be expressed as the following 2nd order polynomial relationship:

$$\mathrm{y} = -0.0007x^2 + 1.3223x - 16.07 \tag{4-3}$$

where x is the temperature acquired from pyrometer using a constant emissivity of 0.45, and y is the actual temperature of the metal measured with thermocouples. Using the calibration formula from Eq.3, it was found that the largest temperature measurement error from 50 ℃ to 500 ℃ is less than 10 ℃.

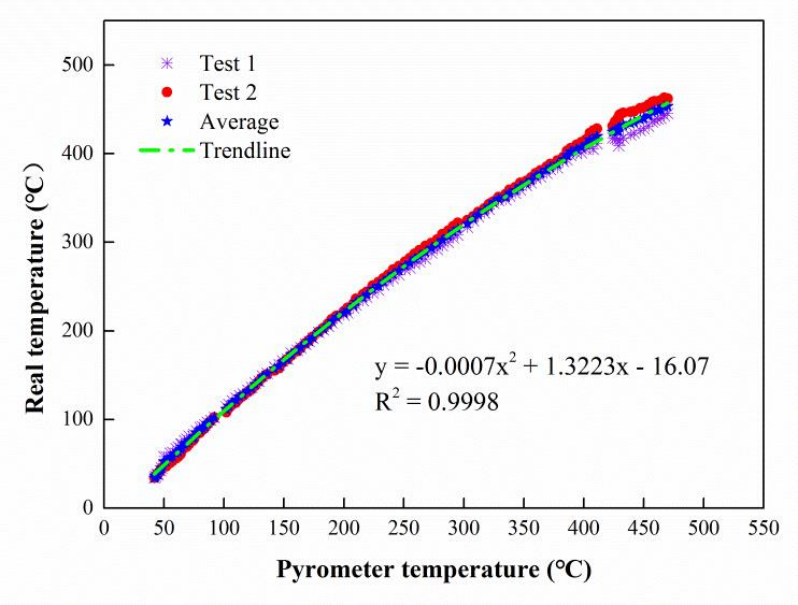

Figure 4-3 Pyrometer calibration curve for Ti6Al4V using fixed emissivity of 0.45

4.3 Results and discussion

4.3.1 Interpass temperature and heat accumulation

Figure 4-4 shows the variation in temperature at both substrate and in-situ layer immediately before each subsequent deposition pass. It can be seen that the average substrate temperature experiences a rapid increase during the first five passes, and then reaches an equilibrium value. In contrast, the interpass temperature continues to climb up to 15 passes. Previous researchers have used the substrate temperature as a key variable for investigating the thermal behaviour of additive manufacturing processes, as claimed by Ding et al. [33] and

Denlinger et al.[43] However, based on the experimental outcomes from this study, it is evident that there is a large discrepancy between the temperature measured at the substrate and the actual interpass temperature, particular if the dwell time between layers is short. If the temperature measured at substrate is taken to be the interpass temperature, it will cause large errors. Direct measurement of the layer surface temperature using noncontact IR pyrometer provides far more accurate and reliable data.

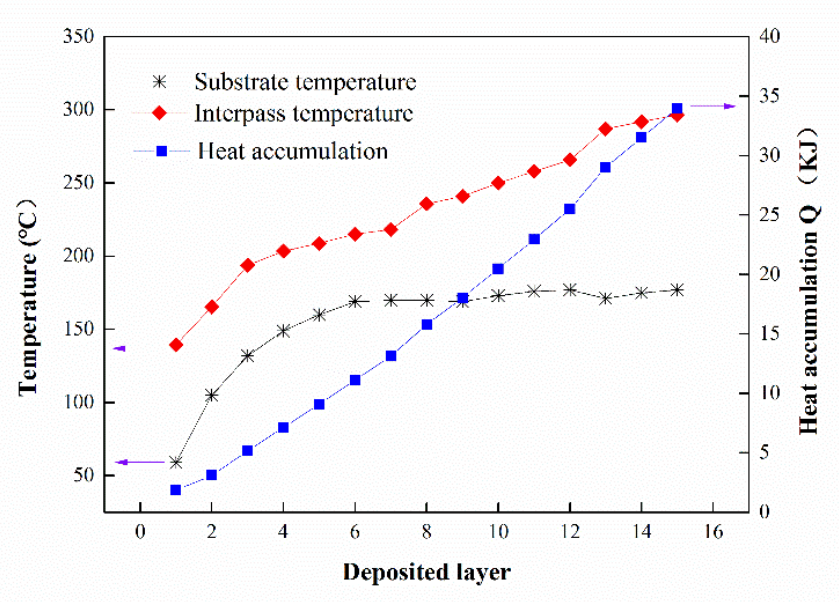

Figure 4-4 The variation in temperature and heat accumulation during fabrication

In order to estimate heat accumulation quantitatively, the equation of Specific Heat Capacity is utilized to calculate the heat accumulation at each layer and is expressed as:

$$Q_j = C \cdot \sum_{j=1}^{n} m_j \cdot \Delta T = C \cdot \sum_{j=1}^{n} m_j \cdot (T_j - T_1) \tag{4-4}$$

$$m_j = \rho \cdot \pi r^3 \cdot v \cdot t_j \cdot \varepsilon \tag{4-5}$$

where C is the heat capacity of Ti6Al4V, approximately 0.619J/(g·K), m is the mass of j^{th} deposited layer, T_j is the interpass temperature of j^{th} layer, ρ is the density of Ti6Al4V, r is

the diameter of the welding wire, v is the wire feeding speed, t_j is the wire feeding time for j^{th} layer, and ε is the material efficiency, which is between 0.95 to 0.98 for the GT-WAAM process. During fabrication, the difference in interpass temperature between subsequent layers determines the final heat accumulation of the as-fabricated part. The detailed data for each layer are listed in **Table 4-2** and the heat accumulation results are presented in **Figure 4-4**. The heat accumulation increased almost linearly with the number of layers as expected.

Table 4-2 Detailed process data for heat accumulation calculation.

i	1	2	3	4	5	6	7	8	9	10	11	12	13	14	15
t/s	95	94	97	98	98	97	98	99	98	95	94	95	93	93	90
m/g	7.57	7.49	7.73	7.81	7.81	7.73	7.81	7.88	7.81	7.57	7.49	7.57	7.41	7.41	7.17
T/℃	139	165	194	204	209	215	218	236	241	250	258	266	287	292	296
Q/KJ	1.85	3.12	5.16	7.14	9.10	11.13	13.13	15.80	18.04	20.49	22.94	25.49	29.00	31.51	33.99

4.3.2 Bead appearance and geometrical features

Figure 4-5 compares the appearance of the first layer with that of the top layer. The surface of the first layer shows a clean silver surface with no sign of oxidation (**Figure 4-5a**), whereas obvious oxidation can be observed at the top layer. This phenomenon indicates that interpass temperature has increased with increasing build height due to the heat accumulation.

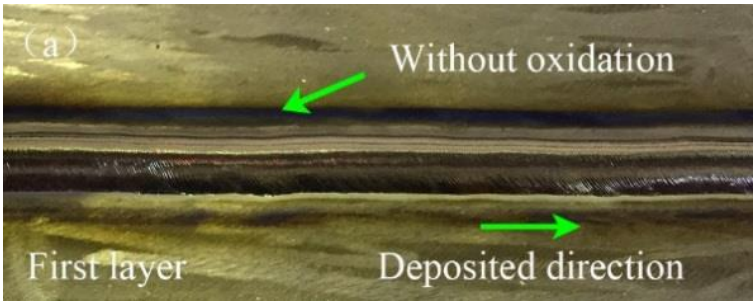

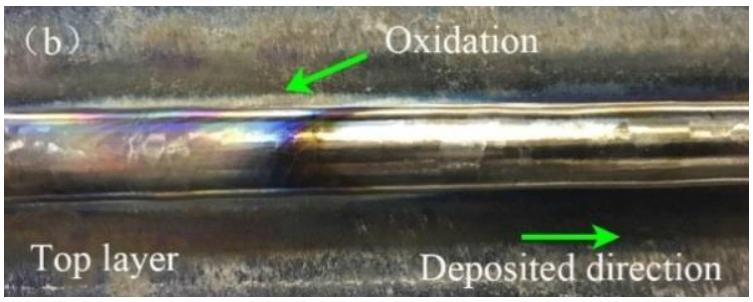

Figure 4-5 The bead appearance of (a) the first layer, (b) the top layer

Hong and Shin [131] pointed out that the appearance of Ti6Al4V alloy can be used for visual assessment of surface imperfections, degree of oxidation as well as the effectiveness of inert gas shielding against atmospheric contamination. As for the surface discoloration, the surface color changes from silver, light straw through dark straw, light blue, dark blue, to grey and powdery, in order of increasing oxidation and contamination. As shown in **Figure 4-5**, the surface colors for the base layer and the top layer are silver and dark blue or gray, respectively, which indicates heavy oxidation on the surface of the top layer. Wang et al. [132] mentioned that surface oxidation was sensitive to temperature and oxygen concentrations in the atmosphere. With an increasing number of deposited layers during GT-WAAM of Ti6Al4V, the surface of freshly deposited layers are exposed to increasingly higher interpass temperatures with a constant interlayer dwell time due to the heat accumulation effects, which produces increasingly severe oxidation. Hence, where a Ti6Al4V part is fabricated using localized gas shielding in an otherwise open atmosphere, it is necessary to control the interpass temperature to ensure that surface oxidation of the most recent deposit is kept at an acceptably low level, to avoid further contamination of the next deposited layer.

Figure 4-6 shows the width of the cross section of the as-fabricated wall along the build

height, which experiences a sharp increase from the 1st layer to the 5th layer. In the first few layers, heat is readily conducted to the substrate, leading to a relatively faster cooling rate and narrower bead. As the wall is built up, the conductive thermal resistance to the substrate is significantly increased. Titanium alloys exhibit poor thermal conductivity, so a decreasing fraction of the heat input from the welding process is conducted away through the substrate (which is now at an elevated temperature). An increasing amount of heat is dissipated to the surrounding atmosphere via convection and radiation, but these temperature-reducing mechanisms are less effective than direct conduction to a cool substrate, which leads to the slower heat dissipation condition of the molten pool and wider bead at higher layers. As more layers are deposited with a fixed dwell time, the deposition width of the wall becomes steady as the heat input and dissipation reach a balance.

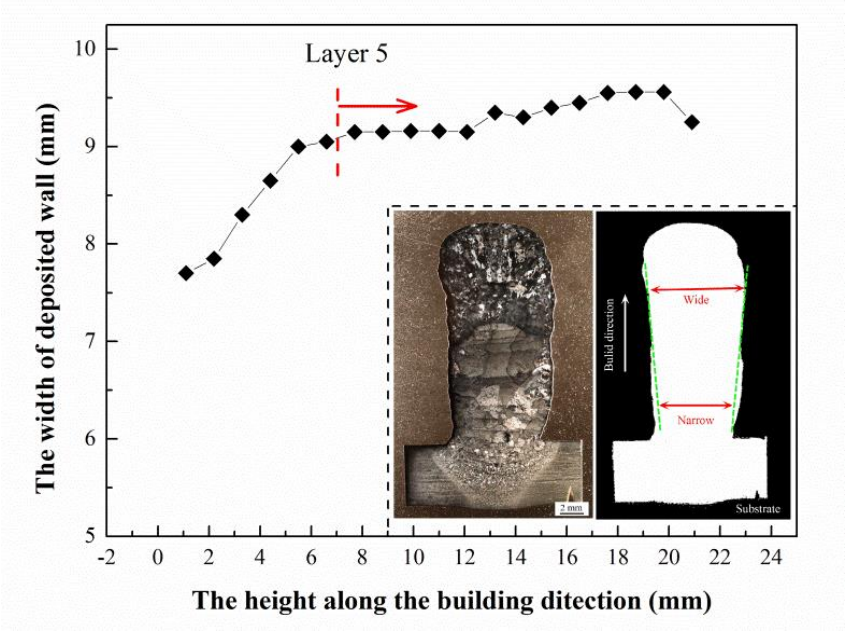

Figure 4-6 Width of the build cross-section along the building height

4.3.3 Stability of weld pool and arc behaviour

4.3.3.1 Arc behaviours

Arc profiles acquired from the high speed camera system were processed using MATLAB, and the arc length measured at each layer is presented in **Figure 4-7**. It can be seen that the average arc length of the first few layers increases with the increasing number of deposition layers, then it tends to be stable, which is consistent with the change in the bead geometry as shown in **Figure 4-6**. The error bar in the **Figure 4-7**, represents the measurement errors of arc length using a total of 500 photographs for each layer.

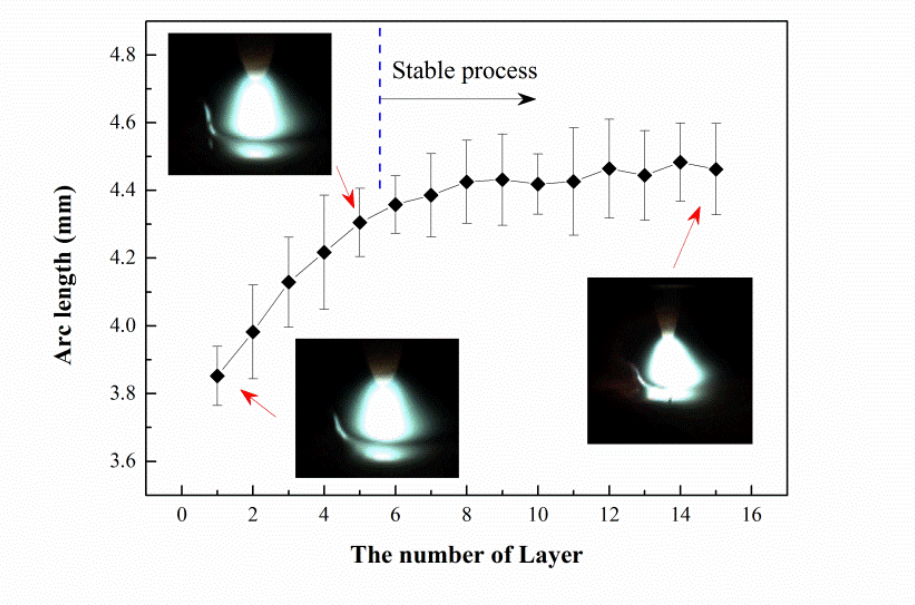

Figure 4-7 The arc shape evolution in GT-WAAM of Ti6Al4V

In general, the arc length is determined by the distance between tungsten tip and molten pool surface. For the GT-WAAM process using localized shielding, even though slight oxidation occurs at the upper layers, the upper surface is still relatively flat and will not be the cause of an inconsistent arc length. However, an obvious expansion of arc profile in the first few layers was observed, as shown in **Figure 4-7**, which indicates that the distance between

tungsten tip and molten pool increases significantly due to the considerable change in bead geometry. According to Wahab et al.[133], the mathematical model of heat transfer in the molten pool is expressed in the following form:

$$k\frac{\delta^2 T}{\delta x^2} + k\frac{\delta^2 T}{\delta y^2} + k\frac{\delta^2 T}{\delta z^2} + k\frac{\delta Q}{\delta t^2} = \rho C\frac{\delta T}{\delta t} \tag{4-6}$$

With the boundary conditions represented as:

$$k\frac{\delta T}{\delta n} + h(T - T_0) + \sigma\varepsilon(T^4 - T_0^4) = 0 \tag{4-7}$$

Based on the assumption of a quasi-steady state approximation, equation (4-7) can be rearranged as follow:

$$k\frac{\delta^2 T}{\delta x^2} + k\frac{\delta^2 T}{\delta y^2} + k\frac{\delta^2 T}{\delta z^2} - \mu\frac{\delta Q}{\delta x} = -\mu\rho C\frac{\delta T}{\delta x} \tag{4-8}$$

where Q is the internal heat energy released or consumed per unit volume ($J{\cdot}mm^{-3}$), T is the temperature related to the heat accumulation, T_0 is the ambient temperature, t is time, k is thermal conductivity ($W{\cdot}(mm{\cdot}°C)^{-1}$), r is density, C is specific heat of the material ($J{\cdot}(g{\cdot}°C)^{-1}$), h is a convection coefficient, σ is the Stefan Boltzman constant and ε is emissivity. As presented by numerical simulation from these conductive models, more heat energy from the arc and molten pool can increase molten pool length and width, which has also been reported by Wang et al.[86]. According to the law of mass conservation, the height of molten pool will decrease in order to make up for the increase in its width and length. In this study, the arc length increased with the variation in bead geometry at first few layers. After five layers' deposition, it stabilizes with further deposition due to constant bead geometry associated with heat equilibrium, as shown in **Figure 4-8**. This is in good agreement with the

change in bead width along the building height as depicted in **Figure 4-7**.

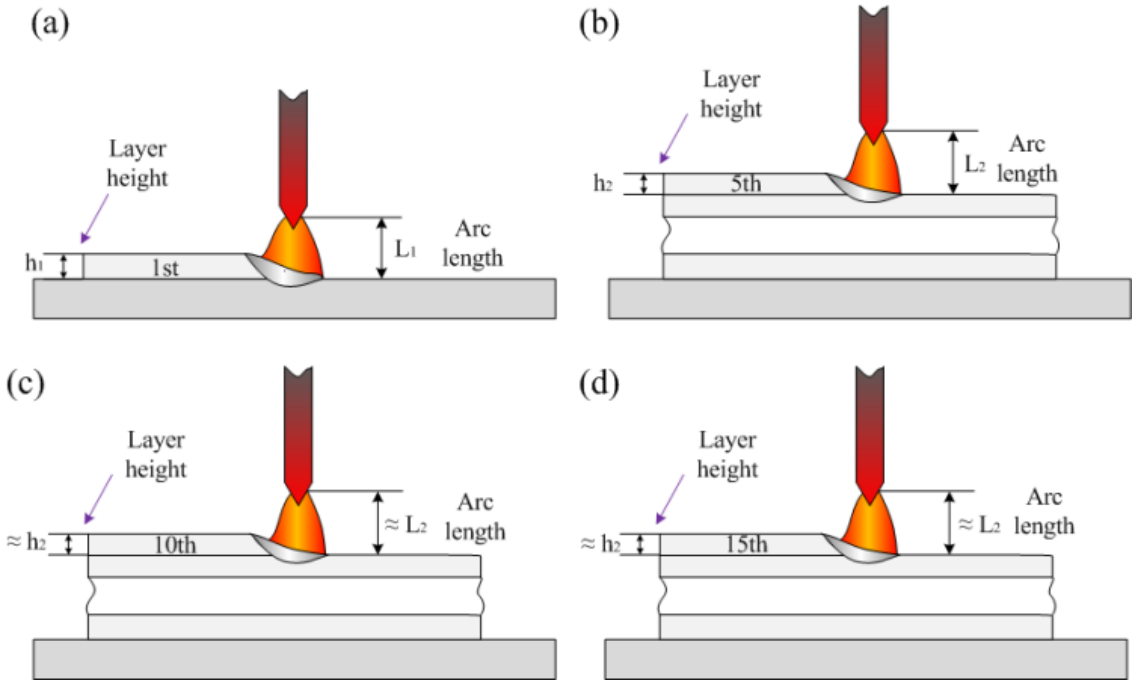

Figure 4-8 The schematic diagram of the changes in arc length and bead height for different layers: (a) layer 1, (b) layer 5, (c) layer 10 and (d) layer 15

In addition, according to findings from Zhou et al.[128], metal vapor produced from the molten pool tends to increase the heat and radiation loss in low temperature areas of the arc, leading to potential arc constriction. To be specific, the isotherms shrinking toward the arc center implies that intensified metal vapor could induce changes in the arc behavior at different layers due to accumulated heat serving as a preheating heat source, which contributes to the melting process of filler and base layer[134]. Therefore, the variation in arc shape can be explained through the combined effects of deposited layer geometry and arc constriction although it has no direct link with heat accumulation in the additive manufacturing process.

4.3.3.2 Metal transfer behaviours

As mentioned above, with increasing built height, the arc shape expands slightly in first few layers and then becomes nearly constant. This phenomenon also has certain impact on the metal transfer behaviour, which has a direct influence on the bead formation and geometrical accuracy of the deposited metal. In terms of cold-wire GTAW, the metal transfer modes can be mainly categorised into four types: intermittent wire melting, uninterrupted bridging transfer, interrupted bridging transfer and free flight transfer[135]. For the GT-WAAM process, the uninterrupted bridging transfer mode forms a smooth and consistent layer appearance, while the irregular free flight mode tends to produce humps and hollows on the surface, as reported by Geng et al.[41].

Figure 4-9 tracks the specific metal transfer process at different layers. It can be seen that the metal transfer state changes with increasing number of layers, especially in the first few layers. At layer 1 where deposition is on the substrate, the metal transfer is through uninterrupted bridging transfer mode, while it gradually changes into interrupted bridging mode in layer 5. **Figure 4-10** provides more detailed images of the metal transfer at specific stages during the deposition. It can be observed that the width of liquid bridging decreased gradually from 1st to 5th layer, which indicates that the distance between the tungsten tip and molten pool has increased due to the change in bead geometry. Furthermore, the free flight transfer mode was occasionally observed in the upper layers due to some distortion of the part under the successive thermal cycles.

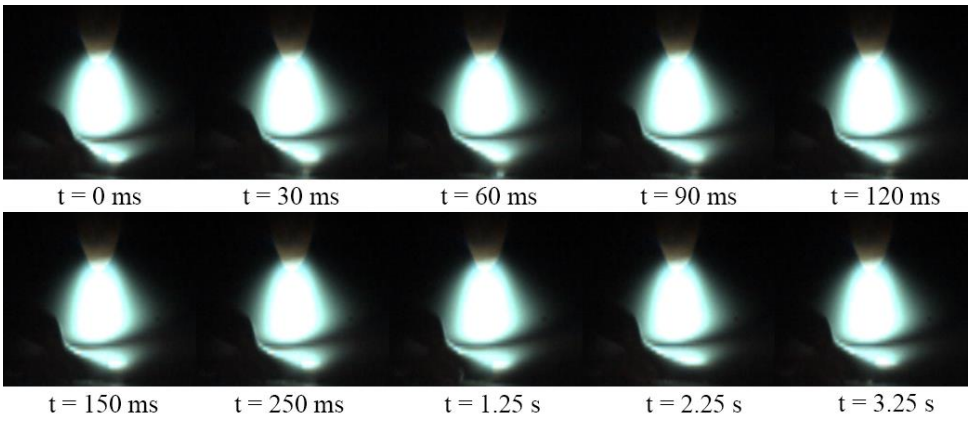
t = 0 ms
t = 30 ms
t = 60 ms
t = 90 ms
t = 120 ms
t = 150 ms
t = 250 ms
t = 1.25 s
t = 2.25 s
t = 3.25 s

(a)

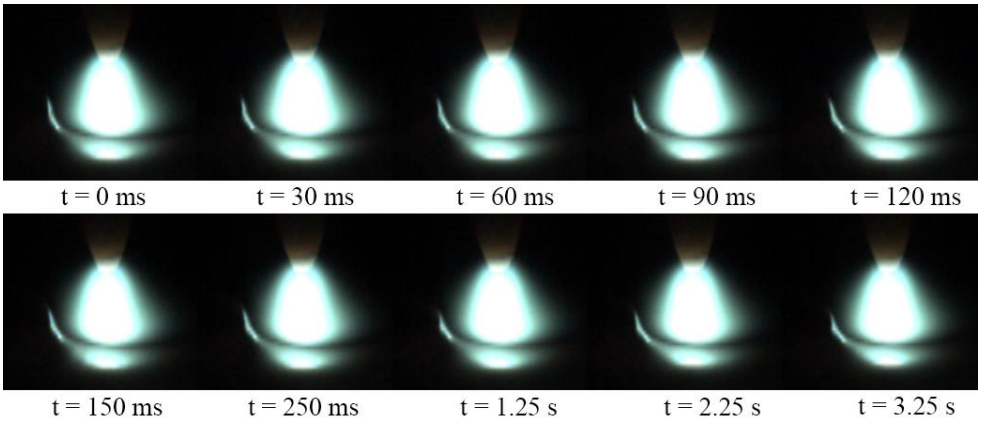
t = 0 ms
t = 30 ms
t = 60 ms
t = 90 ms
t = 120 ms
t = 150 ms
t = 250 ms
t = 1.25 s
t = 2.25 s
t = 3.25 s

(b)

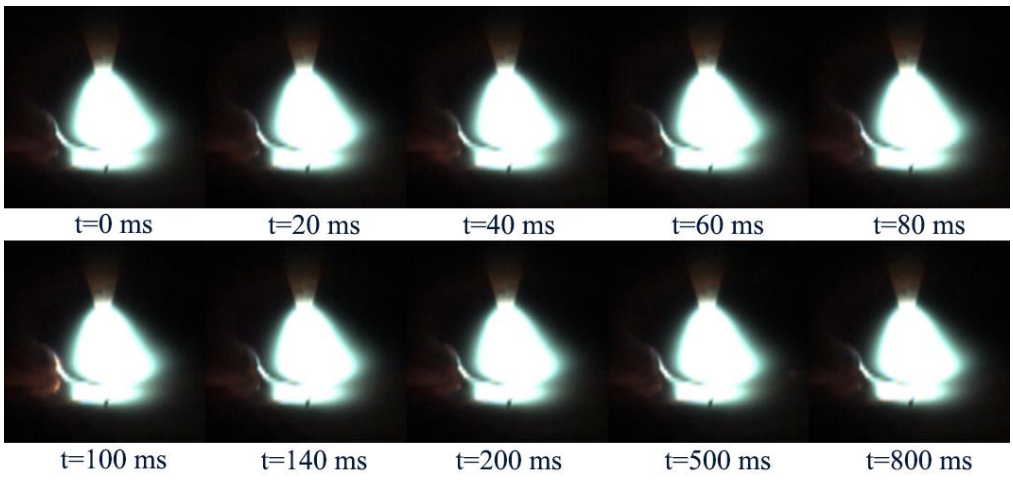
t=0 ms
t=20 ms
t=40 ms
t=60 ms
t=80 ms
t=100 ms
t=140 ms
t=200 ms
t=500 ms
t=800 ms

(c)

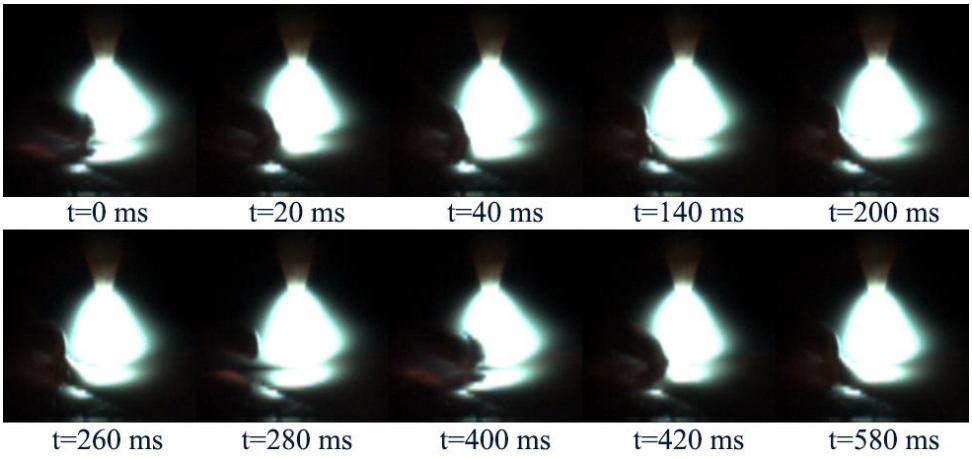

(d)

Figure 4-9 Metal transfer process at: (a) layer 1, (b) layer 5, (c) layer 15; (d) Interrupted transfer occurring from layer 5 to 15

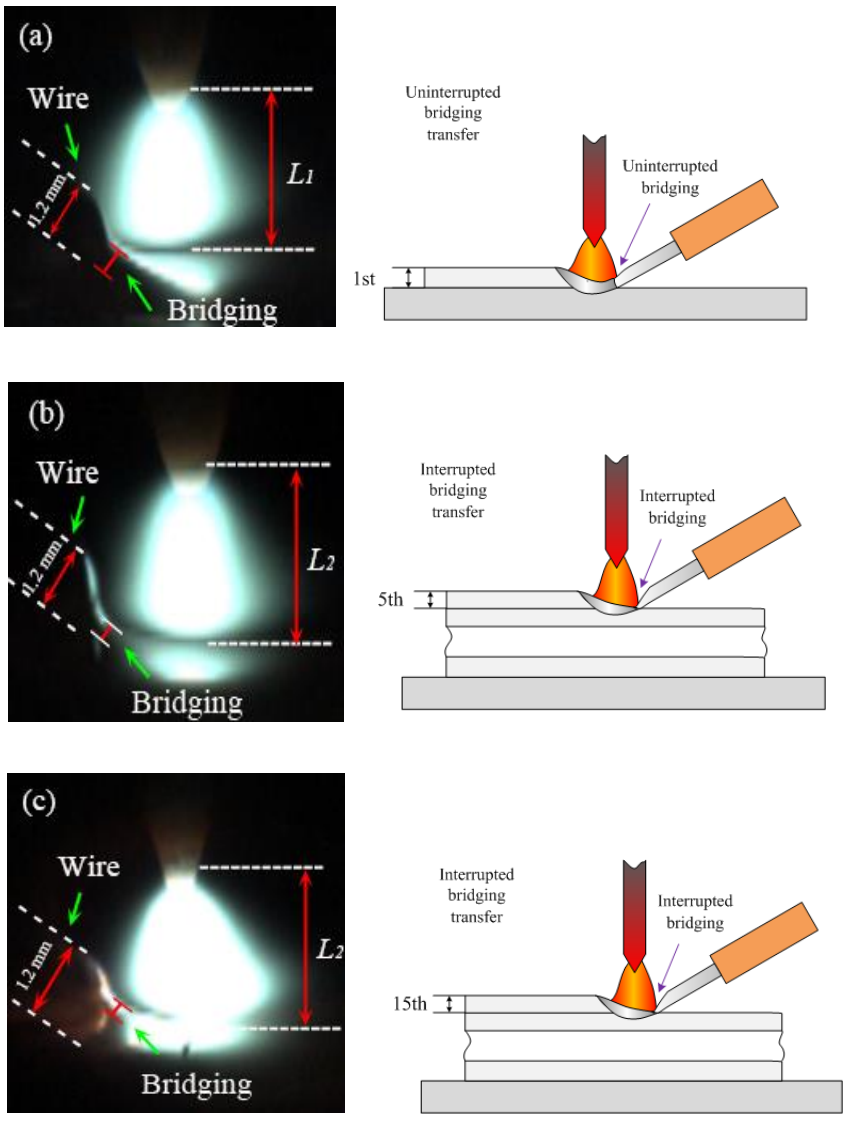

Figure 4-10 Metal transfer behaviour at different layers: (a) layer 1; (b) layer 5; (c) layer 15

It is worth noting that the metal transfer frequency has also experienced a slight increase due to the variations in arc profiles, as shown in **Figure 4-9**. Considering that the variation in the arc shape and molten pool geometry occurs, the forces acting on the droplet also change significantly during the build-up. According to the static force balance theory introduced by Waszink and Graat [136], the major forces acting on the droplet include gravity (F_g), electromagnetic force (F_{em}), surface tension (F_σ) vapor jet force (F_v), and plasma drag force (F_a). For the GTAW-AM process, the balance of these forces determines the metal transfer process, as described in **Figure 4-11.** The detaching force (F_d) is defined as the resultant force on the droplet in the vertical direction, which can be derived by the following expression[137]:

$$F_d = (F_g + F_{em} + F_a + F_p cos60°) - (F_v + F_\sigma Sin30°)$$

$$= \frac{4}{3}\pi r_d^3 \rho_d g + \frac{\mu_0 I^2}{4\pi}\left(\frac{1}{2} + ln\frac{r_u}{r_i}\right) + F_p cos60° + C_d A_p \left(\frac{\rho_f v_f^2}{2}\right) \quad (4\text{-}9)$$

$$-\frac{m_0}{d_f} LJ - 2\pi R\sigma sin30°$$

where F_p is the driving force of feed wire, r_d is the droplet radius, ρ_d is the density of droplet, g is the gravitational constant, μ_0 is the magnetic permittivity, I is the welding current, r_i is the exit radius of the current path, r_u is the entry radius of the current path, which is equal to the radius of anode area, C_d is the drag coefficient, A_p is the projected area on the plane perpendicular to the fluid flow, ρ_f and v_f are the density and fluid velocity of the plasma, respectively, m_0 is the total mass vaporized per second per ampere, I is the welding current, J is the vapor density, R is the radius of the electrode, and σ is the surface tension coefficient. As the constriction of the arc induces an increase in electromagnetic force (F_{em}) acting on the

droplet at the first few layers, the requirement of gravitation force (F_g) for the droplet is reduced according to equation (9). Therefore, the droplet in the liquid bridging area would be detached at a smaller size and the metal transfer frequency increased accordingly.

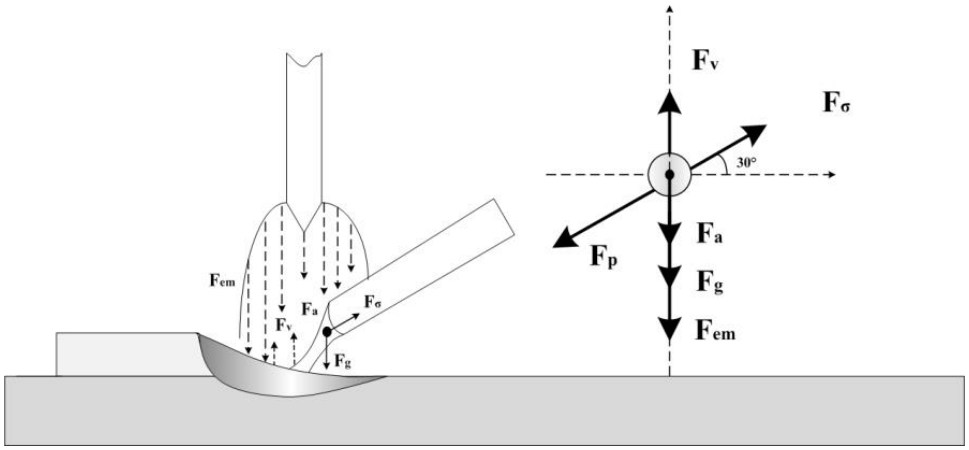

Figure 4-11 Forces acting on droplet during Ti6Al4V GT-WAAM process

4.4 Conclusion

In this section, Ti6Al4V alloy has been used as the build material for the GT-WAAM process using localized gas shielding. Based on the in-situ measurement of the temperature at each layer, the effects of heat accumulation on stability of deposition, oxidation, geometrical shape, arc characteristics and metal transfer behaviour were investigated. The main conclusions are drawn as follows:

(1) By using a noncontact IR pyrometer for direct temperature measurements at the deposition location on the wall, more accurate and reliable information on interpass temperature can be obtained when compared to measurements from thermocouples attached at preset locations on the substrate, due to the existence of heat accumulation.

(2) Due to the changes in heat dissipation path along the deposition height and

decreasing cooling rates, the bead geometry varies in the first few layers, which leads to slight changes in the distance between electrode and molten pool.

(3) The slight variation in arc shape and metal transfer behaviour along the building height can be explained by the combined effects of both increased distance between electrode and the surface of molten pool as well as arc constriction resulting from intensified metal vapor, even though it is not directly related to the thermal behaviours in the WAAM process.

In summary, the influence of heat accumulation on the deposition stability is proven to be very significant during the TiAl64V GT-WAAM process using localized shielding. Therefore, to achieve better geometry and more stable metal transfer, interpass temperature must be strictly controlled during the WAAM of Ti6Al4V.

Chapter 5 MATERIAL PROPERTIES

5.1 Introduction

Complex thermal behaviour during fabrication plays an import role in material properties of components manufactured using Wire Arc Additive Manufacturing (WAAM) technology. It has been demonstrated that the WAAM process is capable of producing high-quality Ti6Al4V components with comparable mechanical properties to those produced by conventional manufacturing processes[26]. However, the control of thermal behaviour, which influences microstructural evaluation, oxidation and defect generation, is a challenging task.

Recently, through numerical simulation, Vastola et al.[138] reported that heat can transfer through several deposited layers to induce microstructural evolution during the electron beam melting (EBM) additive manufacturing (AM) process. Romano et al. [139] investigated the temperature distribution and geometry of deposited Ti6AL4V using both laser and EBM AM processes. Their results show that the heat accumulated within the immediate area of the laser beam will result in a wider melt pool. However, the temperature distribution of EBM is more even because of the higher effective conductivity of the powder bed. Li and Gu [140] observed that during the selective laser melting (SLM) process, heat accumulation can affect the average temperature of the titanium powder bed, leading to a change of geometrical shape and poor accuracy. Wu et al.[141] also found that the heat accumulation will affect the geometry accuracy of the as built component in WAAM Ti6Al4V process, which indicates the importance of in-process temperature monitoring and control. Although the effects of thermal history, such as process temperature and cooling rate, on morphology and properties

of materials have been studied by many researchers, little attention has been paid to the influence of heat accumulation in gas tungsten wire arc additive manufacturing (GT-WAAM) for Ti6Al4V alloy fabrication. It is believed that the microstructure of deposited part would be influenced when the heat accumulates during manufacturing process, which eventually has negative effects to the component property. A better understanding of the underlying mechanism will be beneficial from the perspective of optimizing microstructural control.

In the present section, heat accumulation during GT-WAAM process using Ti6Al4V was calculated by using in-situ interpass temperature measurements from an IR-pyrometer. The surface oxidation, microstructure, grain size, crystalline phase and mechanical properties from various locations of the deposited wall were investigated and discussed in terms of the heat accumulation. Fracture experiments of the corresponding locations were also conducted to reveal the correlation between microstructure and mechanical properties, and to assess the possibilities of fabricating Ti6Al4V parts using WAAM with localized gas shielding.

5.2 Experimental Procedures

5.2.1 Experiment setup

A schematic diagram of experimental system used for this study is shown in **Figure 5-1**. The GTAW process is locally shielded using welding-graded (99.995%) argon to prevent oxidation of the deposited material. Both filler wire and substrate plate are Ti6Al4V. The diameter of the filler wire is 1.2 mm and the dimension of the substrate plate is 200 mm × 150 mm × 6 mm (length × width × thickness). The process parameters used for deposition are provided in **Table 5-1**.

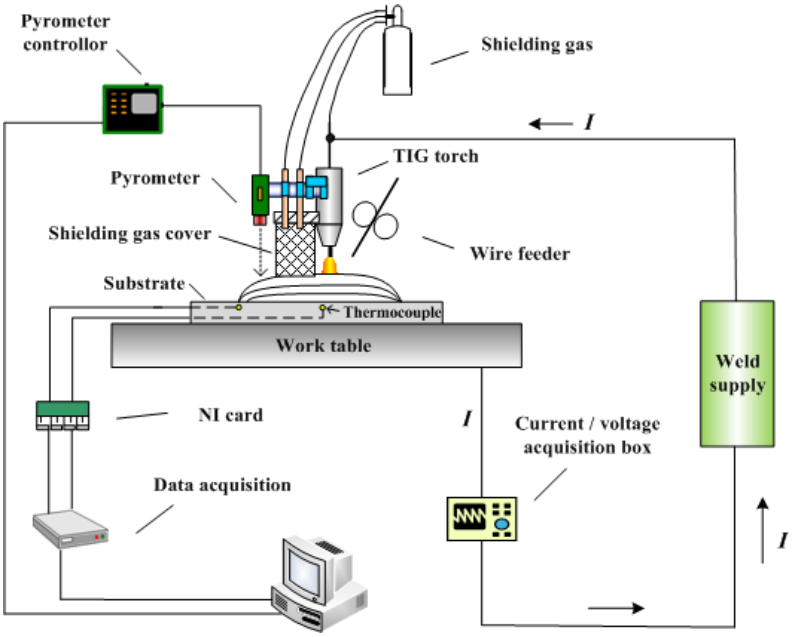

Figure 5-1 Schematic diagram of the GT-WAAM system

Table 5-1 Process parameters for WAAM deposition

Process parameters	Details	
Deposition power	Current	110A
	Arc voltage	12V
Speed	Travel speed	95mm/min
	Wire feed speed	1000mm/min
Distance and angle	Electrode to workpiece	3 mm
	Electrode to filler wire	60°
Flow rate(argon)	GTAW torch	10 L/ min
	Trailing shield	10 L/ min
Time	Post flow duration	35 seconds
	Dwell time between layers	125 seconds

5.2.2 In-situ interpass temperature measurement

In order to accurately measure the in-situ process temperature, thermocouples and an IR pyrometer were used, as shown in **Figure 4-2**. Two thermocouples were fixed on the substrate for continuous monitoring of the substrate temperature, and an IR pyrometer was

installed above the middle of deposited layer to measure the in-situ layer temperature immediately after deposition.

Since the emissivity of the measured material is an essential measurement parameter, the IR pyrometer needs to be calibrated in order to obtain an accurate temperature value. Several calibration tests were carried out in the range of 50℃ to 500℃, and an emissivity of 0.45 was established as the best fit to the temperature measurements from the thermocouples.

5.2.3 Heat accumulation calculation

The equation of Specific Heat Capacity Q_j was used to calculate heat accumulation during the WAAM process, as follows[141]:

$$Q_j = C \cdot \sum_{j=1}^{n} m_j \cdot \Delta T = C \cdot \sum_{j=1}^{n} m_j \cdot \left(T_j - T_1\right) \quad (5\text{-}1)$$

$$m_j = \rho \cdot \pi r^3 \cdot v \cdot t_j \cdot \varepsilon \quad (5\text{-}2)$$

where C is the heat capacity of Ti6Al4V, approximately 0.619J/(g·K), m is the mass of j^{th} deposited layer, T_j is the interpass temperature of j^{th} layer, ρ is the density of Ti6Al4V, r is the diameter of the filler, v is the wire feed speed, t_j is the deposition time for j^{th} layer, and ε is the material efficiency, which is between 0.95 to 0.98 .

Figure 5-2 shows the temperature changes in both substrate and upper-most deposited layer during the fabrication process. It can be seen that after a few layers, the average substrate temperature stabilizes, while the temperature climbs quickly in deposited layers indicating the heat accumulation within the wall. Notably, the temperature difference between the substrate and wall continues to increase after the fifth layer, and approaches a stable value after thirteen layers. Based on equations (5-1) and (5-2), the detailed values of heat accumulation are also presented in **Figure 5-2** in blue.

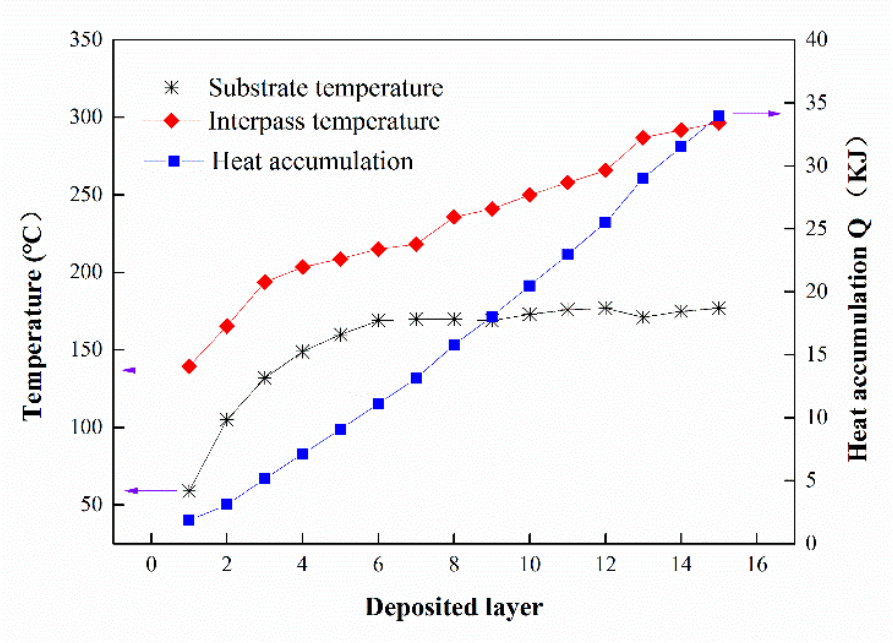

Figure 5-2 The variation of temperature and heat accumulation in this study

5.2.4 Material characterization techniques

After grinding and polishing, the deposited specimens were etched in Kroll reagent (2% vol HF, 6 vol% HNO_3 with balance H_2O) according to standard procedures for microstructure observation using a Leica DMR optical microscope (OM). X-ray diffraction (XRD) measurements were performed on a GBC MMA X-ray diffractometer using monochromatic Cu Kα radiation at an accelerating voltage of 35 kV and a current of 28.6 mA with a scanning step of 0.02º and a scanning speed of 4 º/min in the range of 30º ~ 90º. Tensile tests of rectangular specimens (sample gauge length: 12 mm; width: 2 mm) were carried out on a MTS370 load unit at a crosshead speed of 0.4 mm/min at room temperature [24]. The fracture surfaces of tensile specimens were analyzed using a JEOL JSM-6490LA Scanning Electron Microscopy (SEM) with an Energy Dispersive Spectrometer (EDS) at 20KV.

5.3 Results and Discussion

5.3.1 Microstructure evolution

It is well known that for alpha+beta Ti6Al4V alloy, the thermal history determines the formation of phases structures, including primary alpha, lathlike alpha, colony alpha and hcp martensite alpha (alpha'), grain boundary alpha, acicular alpha and prior beta phases [73].

Figure 5-3 illustrates the microstructural distributions in the cross-section of the as-built specimen and **Figure 5-4** displays the detailed optical micrographs at the marked locations. Due to the high cooling rate for the first few layers from direct contact with substrate, the martensite alpha composed of long orthogonally oriented martensitic plates was formed into lathlike matrix structures[142], as shown in **Figure 5-4a**. In general, this lathlike alpha tend to grow in a long and narrow shape in the direction perpendicular to the liquid/solid interface driven by the maximum temperature gradient during the solidification process[73]. As further layers are deposited, more heat is accumulated in the wall and the process cooling rate continue to reduce so that a fully lamellar alpha morphology is preferentially formed, interwoven with basketweave structures (**Figure 5-4b** and **c**)[143]. At the top layers, large colony alpha, which is decorated within prior beta grains and grain boundary alpha phase (**Figure 5-4 d, e** and **f**), are formed. With the increase of heat accumulation, the process temperature exceeds beta transus temperature T_β (995°C[144]) at the uppermost layers. In combination with a slow cooling rate, this results in the coarse colony alpha structures [145]. It is worth noting that all regions on the fabricated wall have finer grains than that of the base metal (BM) (**Figure 5-4 b**), which is reflected in differences of the mechanical properties of these regions.

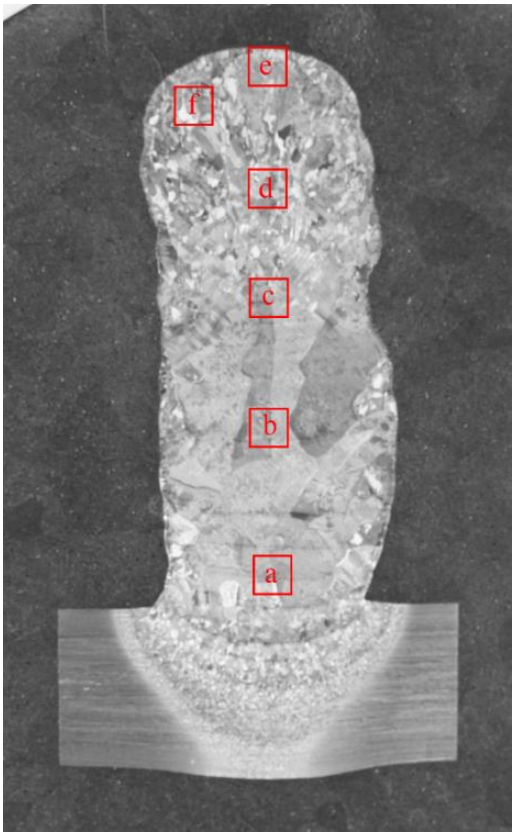

Figure 5-3 Cross-sectional macrograph of the deposited wall.

(a)

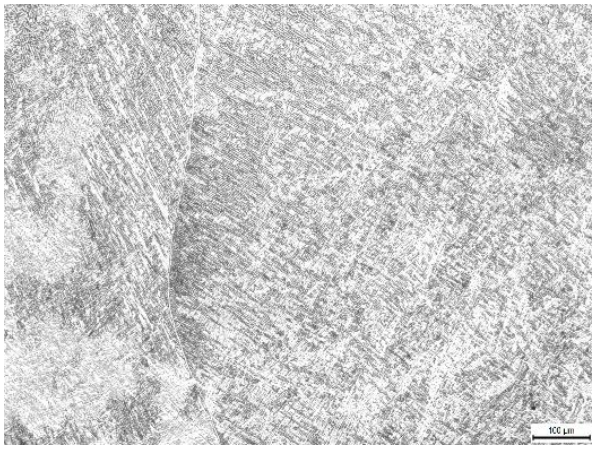

(b)

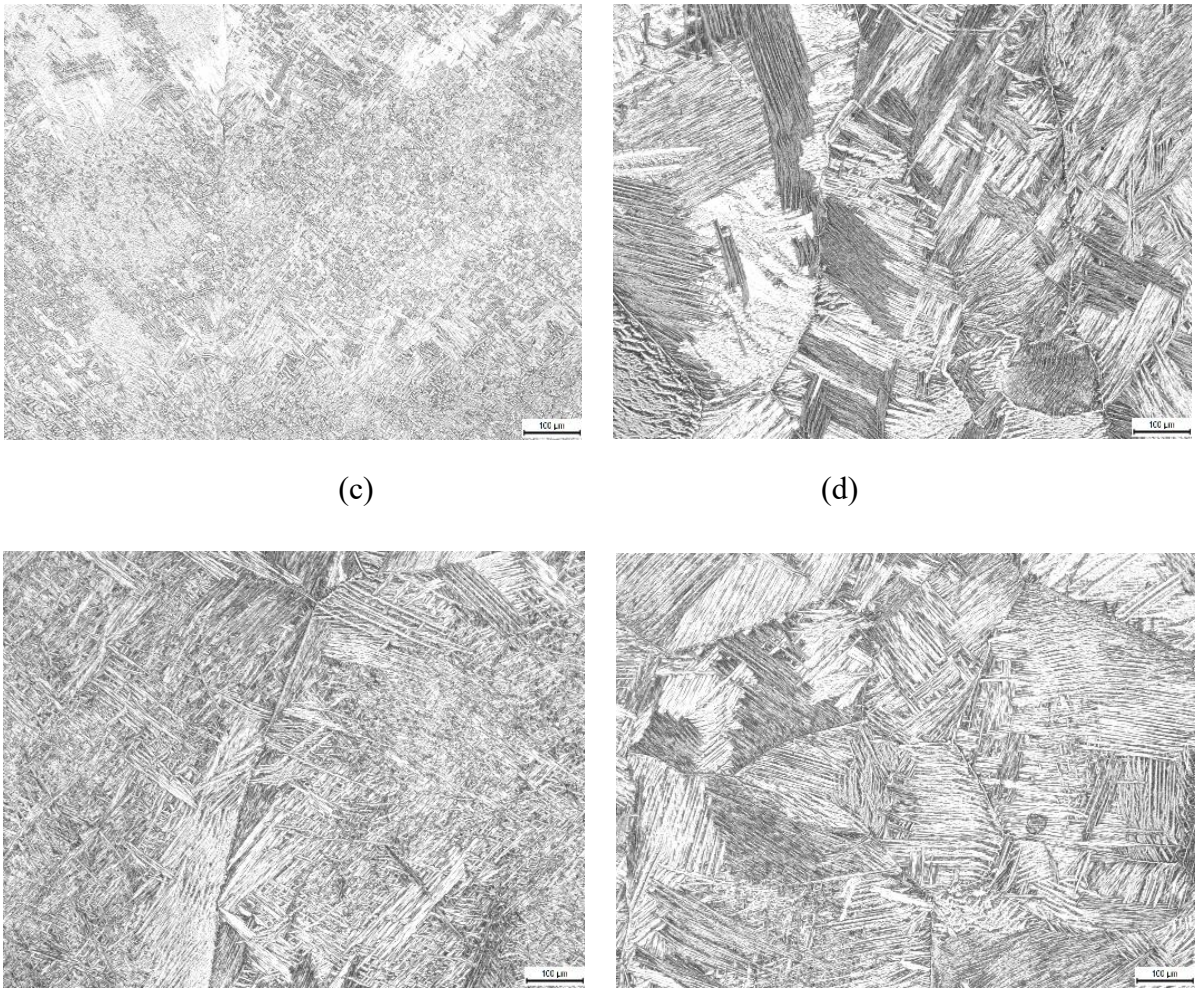

(c) (d)

(e) (f)

Figure 5-4 Optical micrographs of the corresponding regions: a, b, c, d, e, f in **Figure 5-3**

Figure 5-5 shows the optical micrographs in the horizontal plane at four different heights. It can be seen that the microstructures in the horizontal plane and the vertical plane display a similar tendency along the building direction: lathlike matrix structure, lamellar structures, basketwave structures and colony alpha structures in the order of M1, M2, M3, and M4, as shown in **Figure 5-5** (c) to (f) respectively. In particular, the average width of alpha lamellae at M1, M2 and M3 were about 1.89 μm, 1.80 μm and 0.89 μm respectively, as shown in **Fig.5-6**, indicating that alpha grains from the areas at bottom to middle regions have been refined by the thermal cycling. Due to accumulated heat serving as a preheating

process, which contributes to the melting process of filler and base layer, the comparatively higher temperature at M3 regions brings a higher density of dislocation nucleation, which can additionally assist in the process of recrystallisation and creation of fine alpha grains.

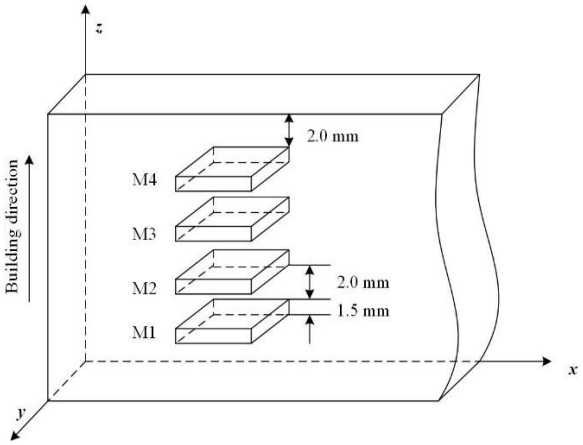

(a)

(b)

(c)

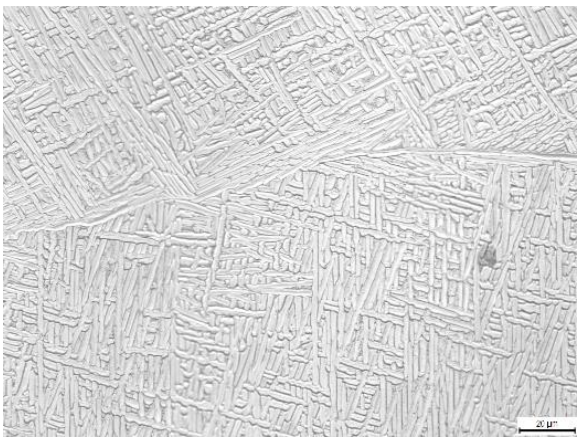

(d)

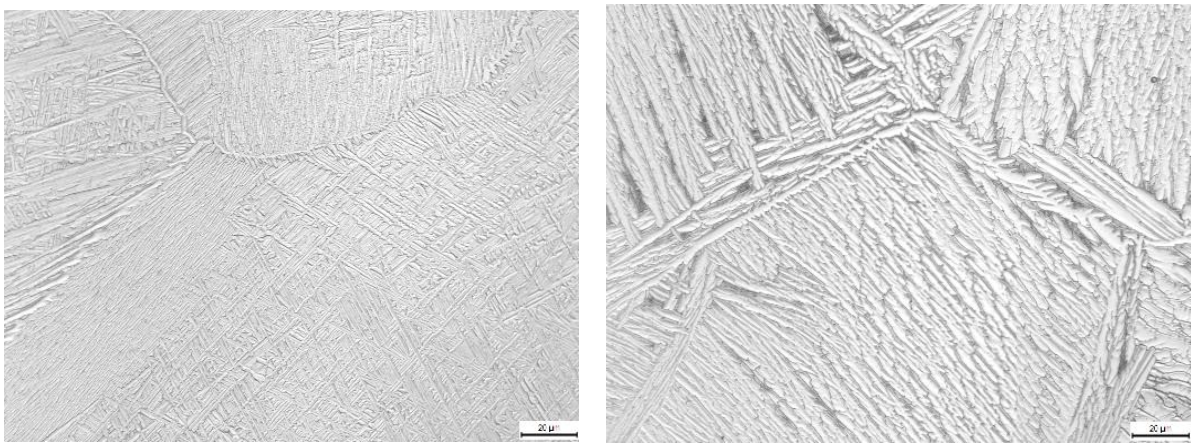

(e) (f)

Figure 5-5 Optical micrographs of selected samples in different horizontal planes: (a) schematic of the sample locations; (b) base metal; (c) M1; (d) M2; (e) M3; (f) M4.

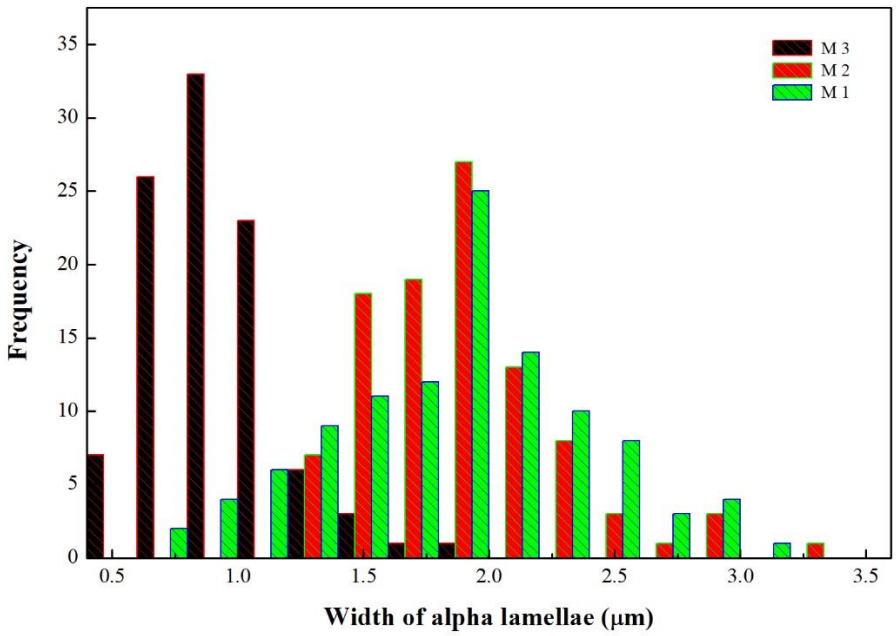

Figure 5-6 Statistical distributions of the width of alpha lamellae for M1, M2 and M3

As a brief summary, the microstructural evolution of Ti6AL4V parts fabricated by GT-WAAM can mainly be divided into four sections in order from bottom to top: lathlike matrix structure, lamellar structure, basketwave structure and colony alpha structures.

5.3.2 Phases characteristics and transformation

The same specimens used for micrographs were also used for XRD refinement measurement to estimate the preferred orientation and the crystal phase of the deposited Ti6Al4V alloy. As shown in **Figure 5-7**, the diffraction patterns for M1to M4 presents ten broad peaks at 35.36°, 38.46°, 39.76°, 40.44°, 53.24°, 56.94°, 63.46°, 70.92°, 74.66°, 76.52°, corresponding to α {101}, α {002}, β {110}, α {101}, β {101}, β [125], α {112}, α {101}/β {211} and α {112} based on the analysis using Jade software.

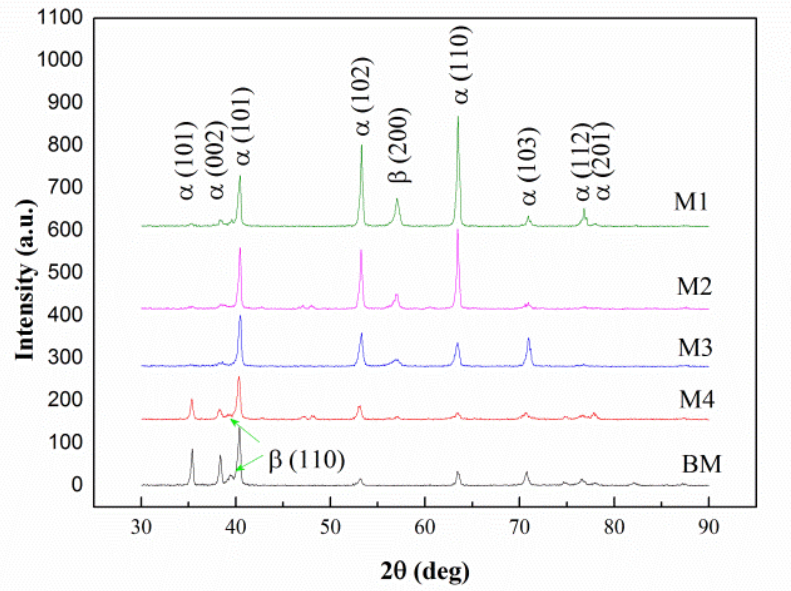

Figure 5-7 XRD spectrums of M1, M2, M3 and M4

It is well known that the grains have their own preferred orientation of growth, namely preferred-growth, dendritic-growth, and easy-growth directions. As can be seen from the Full Width at Half Maximum (FWHM) of different peaks in the XRD patterns of **Figure 5-7**, for the peaks of β {110} plane are almost invisible compared to α {101} peaks, which is attributed to the fact that the β-Ti phase is usually too minor or absent to be detected by X-ray.

With the increase of building height, the volume fractions of α {102} and α {110} decrease significantly, indicating that more lamellar alpha phases are transformed into colony alpha phase during the solidification process. It is worth mentioning that there is no obvious preferred alignment direction for alpha lamellae in both vertical and horizontal planes due to the generation of crystallographic texture along the columnar growth [74, 146].

5.3.3 Mechanical properties

At room temperature, the as-received base metal exhibits a yield strength (YS) of 884 ± 27 MPa, an ultimate tensile stress (UTS) of 995 ± 29 MPa and a total elongation of about 18.6%. **Figure 5-8** shows the tensile test results of WAAM samples at eight locations along the height of the wall. From locations S1 to S4, the YS varies slightly in the range of 892MPa and 844 MPa, while the UTS varies between 958MPa and 1049MPa, which are comparable to the base metal values. However, the mechanical properties are significantly degraded after S4 (approximately 8mm above the substrate), where the interpass temperatures exceeds 200°C. The fracture of these samples occurred in the linear elastic stage, as shown in **Figure 5-8b**, which indicates an obvious decrease in the elongation and reduction of area in these regions.

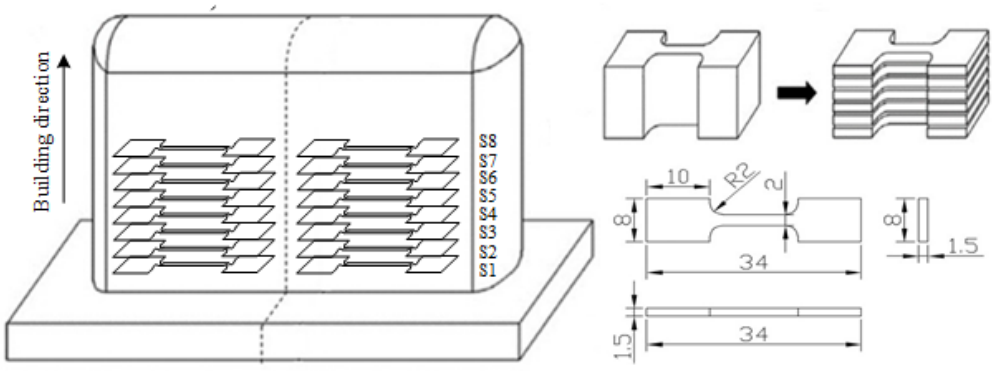

(a)

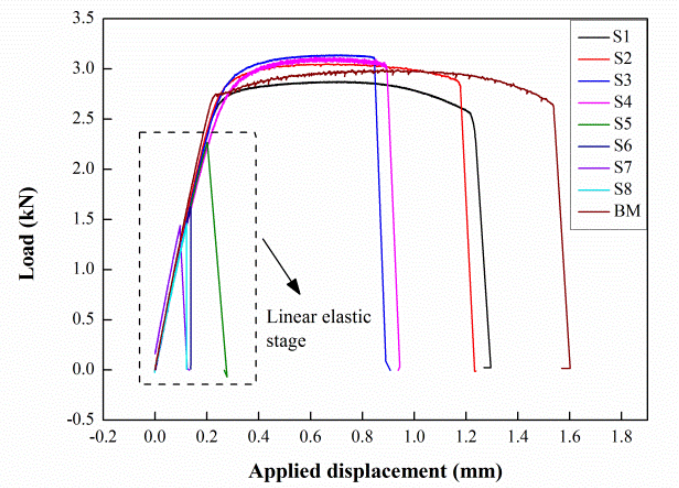

(b)

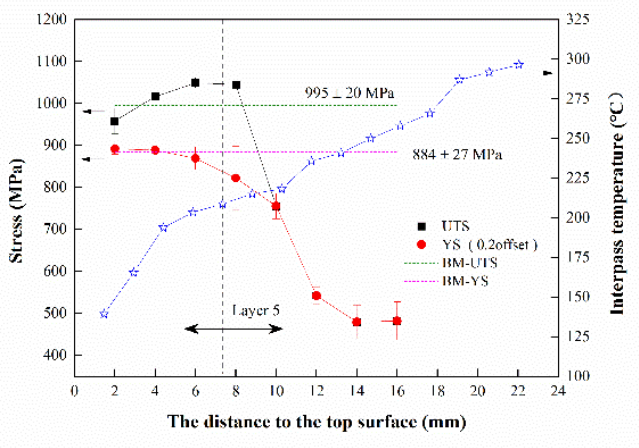

(c)

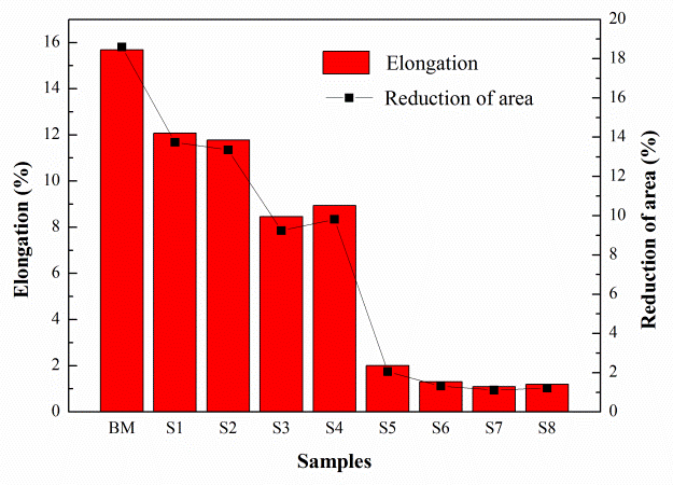

(d)

Figure 5-8 Mechanical test results of the selected samples in horizontal plane of the deposited wall: (a) the locations of tensile samples; (b) load-displacement relationships; (c) ultimate tensile strength and yield strength; (d) elongation and reduction of area

For Ti6Al4V alloy with a lamellar microstructure, the yield strength is primarily related to the solid solution strengthening, including alpha plate boundary spacing and interstitial solute level [147]. In the lower regions, the high interstitial content in both lathlike matrix structure and lamellar structure is positive for improving YS and UTS. However, for the regions where interpass temperature is above 200°C, more acicular and colony alpha were formed, resulting in a decrease of interstitial content and alpha lamellae boundary spacing, which deteriorates the mechanical strength. However, the precipitous drop in both YS and UTS are mainly contributed by the oxidation due to the high interpass temperature. When the interpass temperature is over 200°C, the trailing shield is not sufficient and a superficial oxide coating can be clearly observed. As the interpass temperature increased, heavier oxidation could be observed visually.

5.3.4 Facture behaviours

Figure 5-9 shows the appearance of tensile failure after uniaxial tension tests. It can be recognised that the samples from S1 to S4 present obvious lamellar tearing and neck contraction in fractural locations, while the samples from S5 to S8 break with no deformation, which is in line with the elongation results in the previous section.

Figure 5-10 further displays the fractographs of these tensile specimens. The shear lips can be clearly observed on samples S1 to S4, especially for S1 with a large number of dimples in lower regions, which illustrates a typical ductile fracture. Due to rapid heat dissipation into the substrate in the first few layers, alpha lamellae structures were formed. The areas of interphases decreased, resulting in the promotion of void growth [148] and generation of a number of dimples. However, samples S5 to S8 show more brittle cleavage

morphology in response to fracture, which is contributed from the increase of colony alpha structures decorated within beta grains and pinning effects with carbon and oxygen solute. According to a study of the fracture characteristics for Ti6Al4V parts fabricated using LSM, it was found that the tensile fracture mainly occurred following the beta grain boundary as well as concomitantly generated internal cracks [149]. As shown in **Figure 5-11**, the cracks that appear in S7 indicate that intercrystalline fracture occurs and the tensile strength is greatly reduced. Furthermore, the alpha phases decorated at the prior beta grain boundary also have significant effects on the fracture features [147]. To be more specific, the alpha grain boundary is much softer than the beta grain, which results in the interface at phase boundaries being more brittle in the fracture tests[149]. Therefore, the regions where more beta grains have formed exhibit cleavage fracture features, and this also explains why the elongation of these regions is very low with fracture failure.

In addition, through EDS analysis, two important interstitial elements, carbon and oxygen, are observed in the fractural surface of upper regions, which indicates potential chemical reactions of Ti with O_2 and CO_2 from the surroundings. This induces the pinning effects with carbon and oxygen solute atoms in the microstructures [150], leading to unacceptably low ductility in the influenced regions as well as fracture failure at the linear elastic stage.

The critical ductility factor, reduction of area, can also be used to distinguish the fracture features. For a tensile specimen with reduction of area greater than 5%, it would be defined as ductile fracture; otherwise it would be classified as brittle fracture. From **Figure 9d**, it can be seen that samples S1 to S4 undergo more than 5% reduction of area, which indicates that

these locations within the fabricated wall should exhibit ductile fractures, as compared to samples S5 to S8. These results also explain why regions along the building direction have different fracture features. It is evident that during the manufacture of Ti6Al4V with the GT-WAAM process using localized gas shielding, the changes in oxidation and microstructural evolution that are caused by altered thermal behaviours have a significant negative impact on the mechanical properties of fabricated parts.

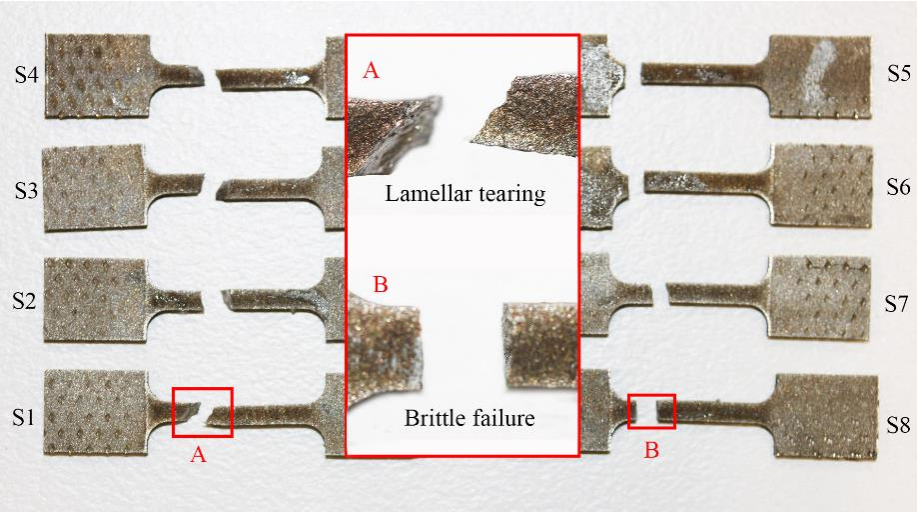

Figure 5-9 The fracture appearance of the tensile specimens

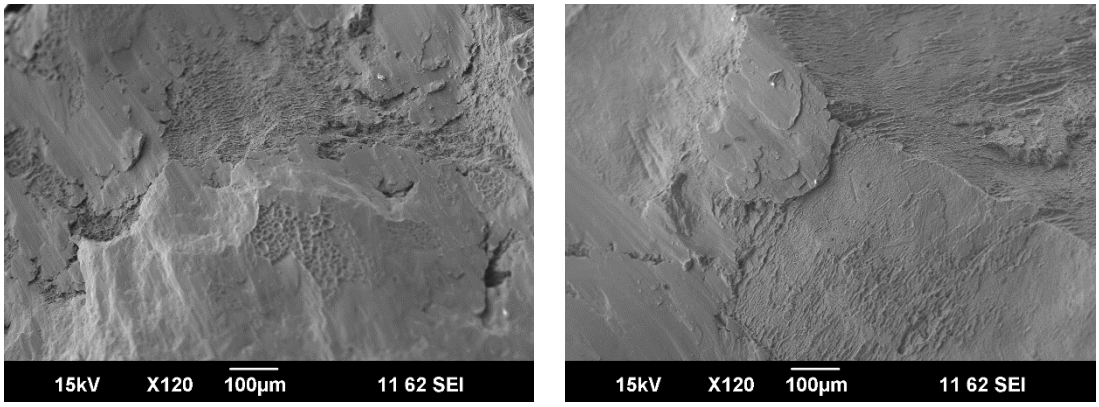

(a) (b)

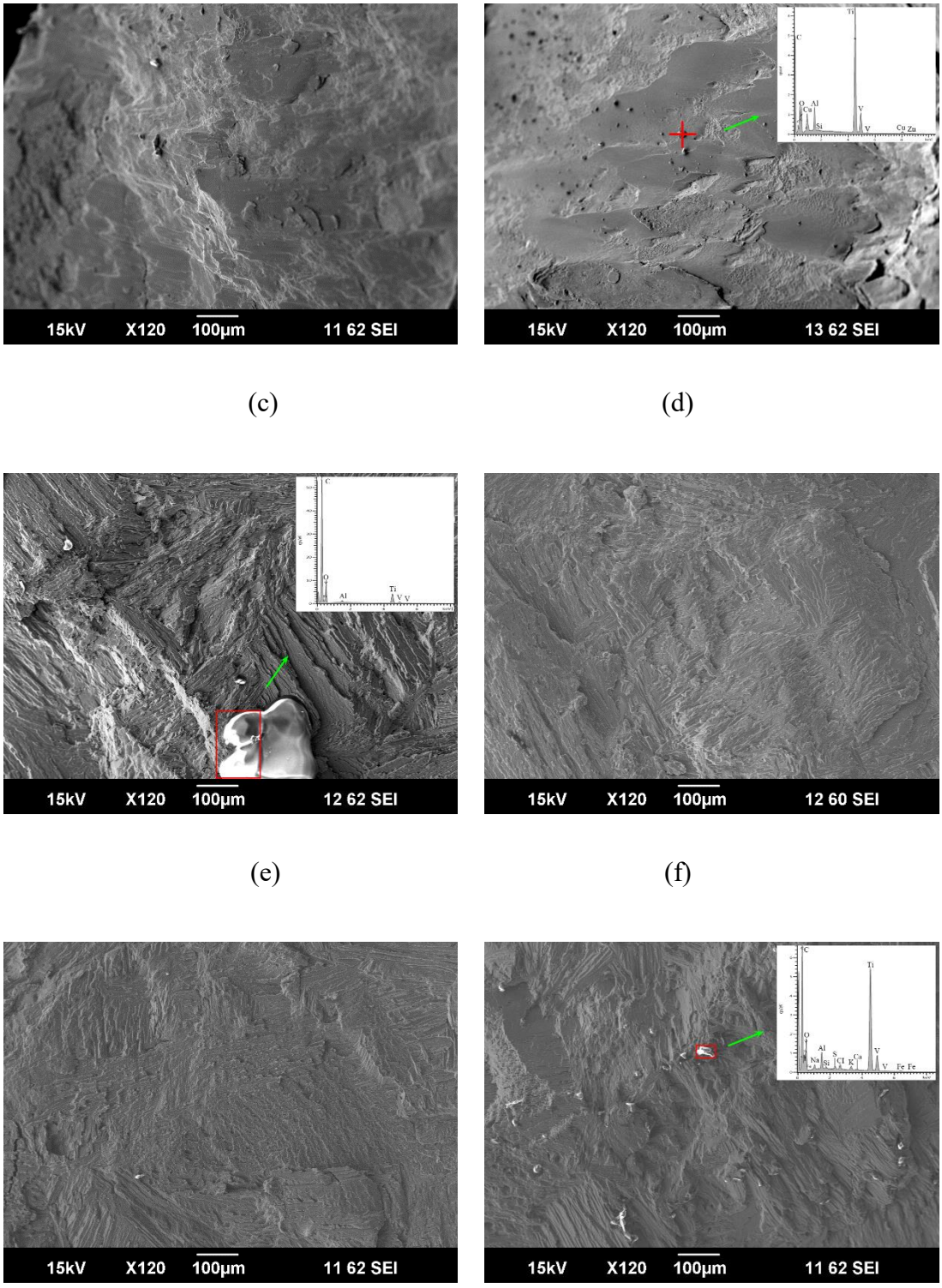

Figure 5-10 High-magnification fractographs of corresponding tensile samples: (a) S1; (b) S2; (c) S3; (d) S4; (e) S5; (f) S6; (g) S7; (h) S8.

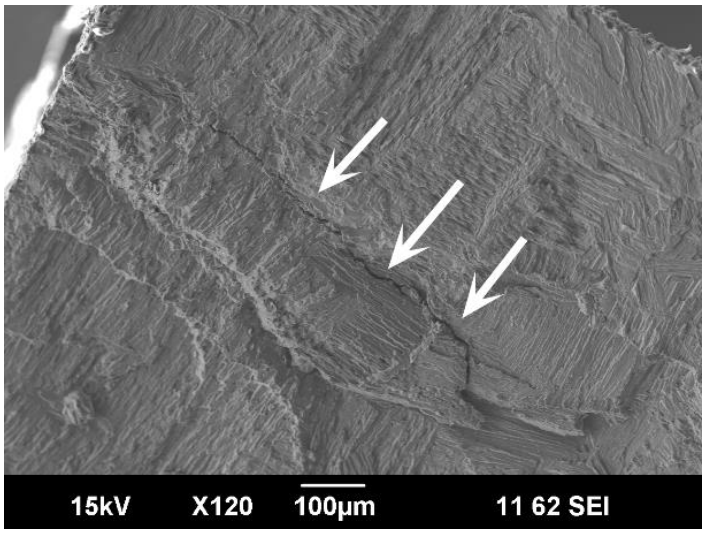

Figure 5-11 Axial crack in fracture surface of S7

5.4 Conclusion

In this section, Ti6AL4V alloy was fabricated by the GT-WAAM process using only localized gas shielding. Based on the in-situ temperature measurement at each layer, the heat accumulation during the deposition process was calculated. OM, XRD, SEM, EDS and standard mechanical test investigations were performed, and demonstrated that the microstructural morphology, crystalline phase, mechanical properties and fracture feature features varies are all changed as heat accumulates along the building direction. The findings include:

(1) To obtain favorable mechanical properties, limiting interpass temperature to 200°C is desirable for Ti6Al4V fabrication when using WAAM technology with localized gas shielding.

(2) The microstructural evolution influences the mechanical properties and fracture features of the as-fabricated part through the phase transition in the development of lathlike matrix structure, lamellar structure, basketwave structure and colony alpha structure along the

building height. The control of colony alpha structure formation is beneficial to the improvement of ductility.

(3) The discrepancy of the mechanical properties in different locations along the deposited wall can be explained by the dominant effects of oxidation and the partial influence from microstructural evolution that are collectively determined by the layer's interpass temperature.

In summary, a better understanding of the effects of heat accumulation on material properties during the WAAM process will benefit future process control, improvement, and optimization.

Chapter 6 CORROSION RESISTANCE

6.1 Introduction

For many applications, corrosion resistance is a primary consideration because it often determines the service life of the component. A number of studies have assessed the corrosion behaviour of Ti-6Al-4V under various conditions. Dai et al. [151] evaluated the corrosion resistance of selective laser melted (SLM) Ti-6Al-4V in NaCl solution, and found that the SLM-produced samples had poorer resistance to corrosion than commercial grade 5 wrought alloy due to the acicular α' martensite formed within the microstructures. The authors further reported that anisotropic corrosion behaviour exists in SLM-fabricated Ti-6Al-4V alloy[152]. In 1 M HCI solution, corrosion resistance in the planes perpendicular to the build direction is superior to that in planes parallel to the build direction, while in 3.5 wt.% NaCl solution, the corrosion resistances show only a very slight difference. Recently, a group of electrochemical corrosion tests in NaCl solution were carried out by Yang et al.[153] to compare the corrosion resistance of Ti-6Al-4V specimens that were processed by SLM, SLM followed by heat treatment (SLM-HT), WAAM and also traditional rolling conditions. The SLM-HT sample exhibited the highest corrosion resistance, followed by rolled, WAAM and finally SLM. The differences in performance were attributed to the formation of distinctive microstructures by the different manufacturing processes. In the cause of WAAM-produced Ti-6Al-4V, the corrosion mechanism is still not well understood due to its complex microstructural distribution and limited information reported in earlier literature. It is believed that the electrochemical corrosion resistance of WAAM-fabricated Ti-6Al-4V has anisotropic

characteristics due to its directional microstructures. A better understanding of the underlying mechanism may be beneficial from the perspective of optimizing microstructural control in the WAAM process.

In this section, a comprehensive investigation on the electrochemical corrosion behaviour of WAAM-fabricated Ti-6Al-4V part has been conducted by means of optical microscopy (OM), X-ray diffraction (XRD), hardness testing, potentiodynamic polarization and electrochemical impedance spectroscopy (EIS) analysis. Specimens were produced from the fabricated part in orientations parallel and perpendicular to the build direction, to assess the influence of directional microstructure on corrosion behaviour. Samples were also taken from the build substrate, to assess the comparative corrosion behaviour of conventional roll-processed or wrought Ti-6Al-4V. The findings provide an insight into the corrosion mechanism of WAAM fabricated Ti-6Al-4V, which gives direction to future improvements of process control and optimization.

6.2 Experimental Procedures

6.2.1 Sample and solution preparation

The apparatus used in this study mainly consists of a 200A-rated GTAW power source, “cold” wire feeder, water cooling unit and travel mechanism, as shown in **Figure 6-1**. The feedstock was commercial ASTM B863 grade 5 Ti-6Al-4V alloy wire with a diameter of 1.2mm deposited onto a Ti-6Al-4V substrate with dimensions of 200 mm × 150 mm × 6 mm to ASTM B265 specification. A straight wall structure of 150 mm in length, approximately 10 mm in width and fifteen layers in height was fabricated with the prepared GT-WAAM system

using localized gas shielding. The process parameters are provided in **Table 6-1**. Welding grade argon (99.995% purity) was used for both GTAW torch and trailing shield. After deposition, the fabricated wall was sliced into two groups of specimens: vertical planes (VP) and horizontal planes (HP), respectively, as shown in **Figure 6-2**. In addition, the same size of specimen was cut from the substrate base metal (BM) and used as a third investigation group.

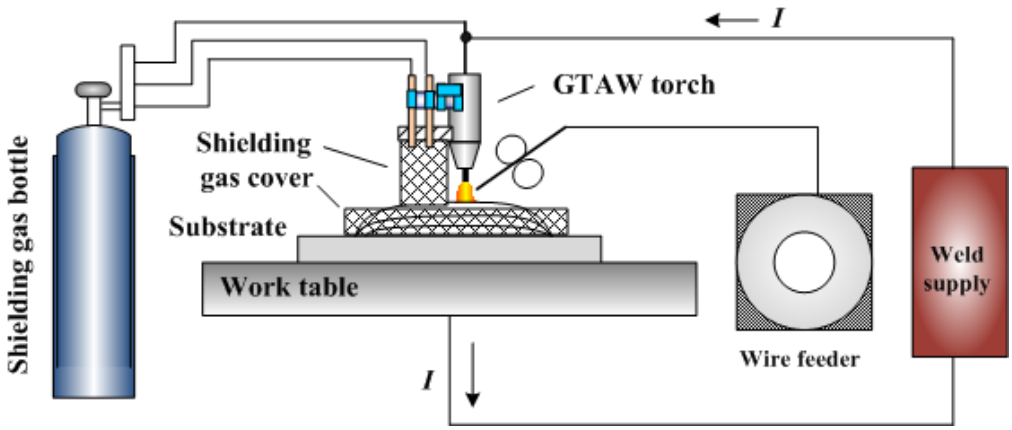

Figure 6-1 Schematic diagram of GT-WAAM system

Table 6-1 Process parameters for GT-WAAM deposition

Process parameters	Details
Deposition current	110 A
Arc voltage	12 V
Travel speed	95 mm/min
Wire feed speed	1000 mm/min
Distance between the electrode and workpiece	3 mm
Angle between the electrode and the filler wire	60°
Flow rate of argon in GTAW torch	10 L/ min
Flow rate of argon in trailing shield	10 L/ min
Post flow duration	35 seconds
Dwell time between layers	125 seconds

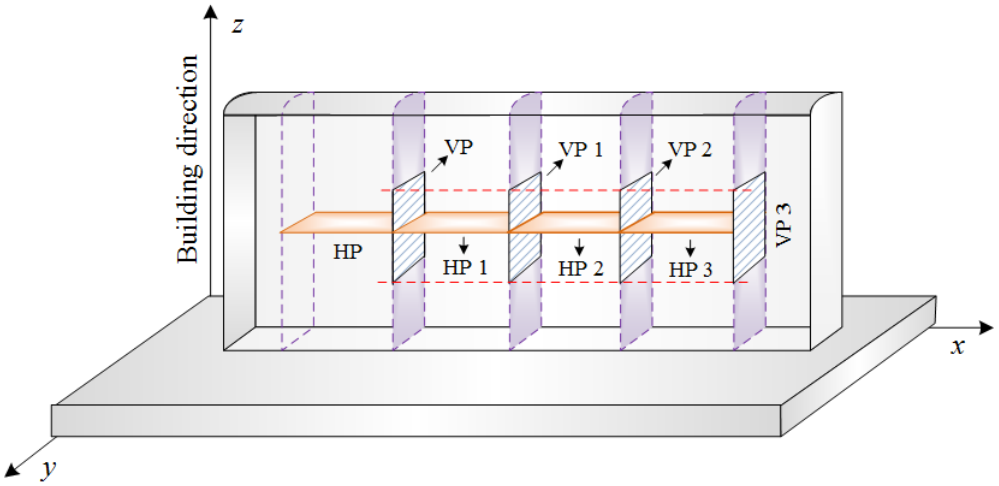

Figure 6-2 Three-dimensional diagram of WAAM-fabricated Ti-6Al-4V wall showing orientation of specimen planes

6.2.2 Material analysis

The extracted specimens for microstructural observation were hot mounted, ground and polished according to standard procedures, and then etched in Kroll's reagent containing 2% vol HF, 6 vol% HNO_3 with balance H_2O. The microstructures were observed using a Leica DMR optical microscope (OM). Qualitative micro-analysis of phases constituents were determined by grazing-incidence X-ray diffraction (XRD) with a GBC MMA X-ray diffractometer using monochromatic Cu Kα radiation at an accelerating voltage of 35 kV and a current of 28.6 mA in scanning steps of 0.02º and a scanning speed of 4 º/min in the range of 30 ~ 90º. Vickers hardness testing was performed with a DuraScan 70 automatic hardness tester using a test load of 0.98 N and a dwell time of 15 s according to ASTM: F2924. The average value of ten measurements was taken as the hardness for each specimen.

6.2.3 Electrochemical measurements

All the samples to corrosion test were subjected to grinding with 220 # SiC paper for 5 minutes, followed by polishing with different size of clothes from 9 μm down to 1μm (standard metallographic method for Ti6Al4V alloys) using Struers Tegrapol 21 automatic grinder and polisher. The electrochemical tests included open circuit potential (OCP), potentiodynamic polarization and electrochemical impedance spectroscopy (EIS). All the electrochemical experiments were conducted on a CH Instruments 600C electrochemical station with a conventional three-electrode cell in 3.5 wt.% NaCl solution at room temperature. A platinum sheet and saturated calomel electrode (SCE) were used as counter electrode and reference, respectively. The electrochemical active surface area of working electrodes was kept at 0.2 cm^2. Before polarization and EIS tests, the specimens were immersed in solution for sufficient time to obtain a stable OCP. EIS was performed in the frequency range of 0.01Hz to 100 kHz with an amplitude of 10 mV. Subsequently, the potentiodynamic polarization experiments were carried out at ±150 mV versus OCP at a sweep rate of 0.5 mV/s. Strong polarization tests were carried out in the potential range of −1 V to + 2 V at a scan rate of 5 mV/s in 3.5 wt.% NaCl solution. The electrochemical measurements were divided into three groups: vertical plane (VP), horizontal plane (HP) and base metal (BM), each group having three specimens selected from identical planes for checking reproducibility of data.

6.3 Results

6.3.1 Microstructural studies

6.3.1.1 Metallographic microstructure

Figure 6-3 shows the optical micrographs of BM, VP and HP regions of the fabricated specimen. The main microstructure of wrought Ti-6Al-4V alloy presents a mixed α/β equiaxed phase structure distributed uniformly. For the WAAM-fabricated Ti-6Al-4V samples, a secondary α morphology (acicular martensite α') is preferentially formed in HP regions, while a fully lamellar α morphology forms in VP regions, interwoven with a Widmanstätten structure inside the prior-grain boundary α. The microstructure of WAAM-fabricated Ti-6Al-4V is inhomogeneous in both HP and VP regions, which is likely to produce non-uniform properties and performance.

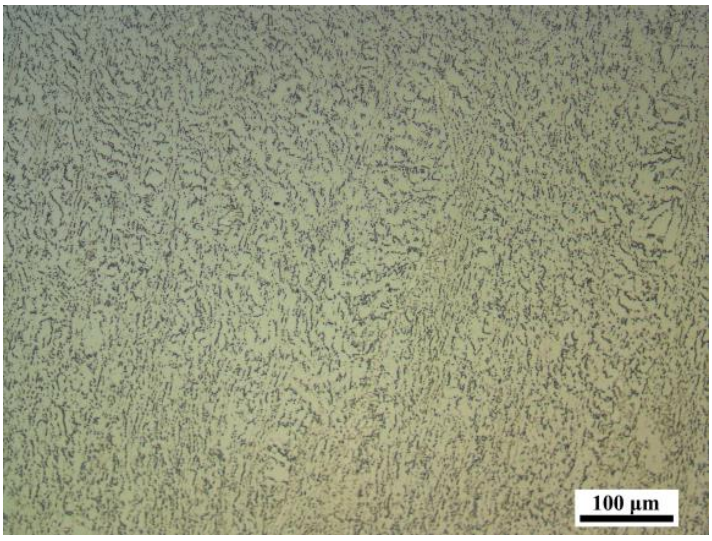

(a)

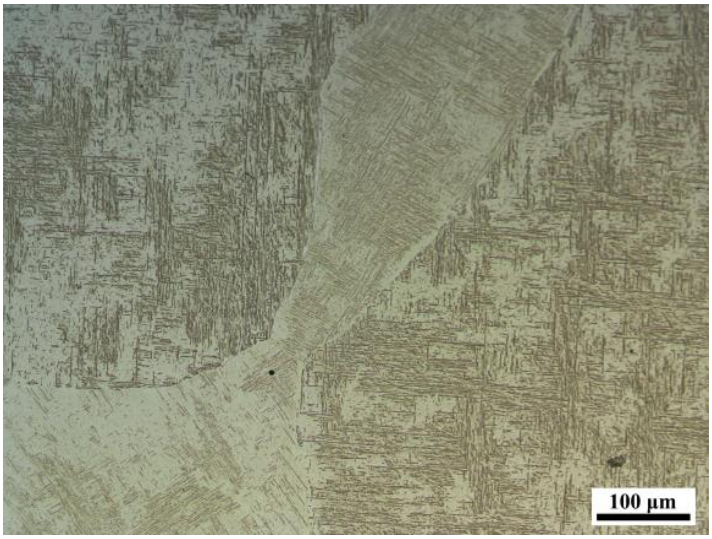

(b)

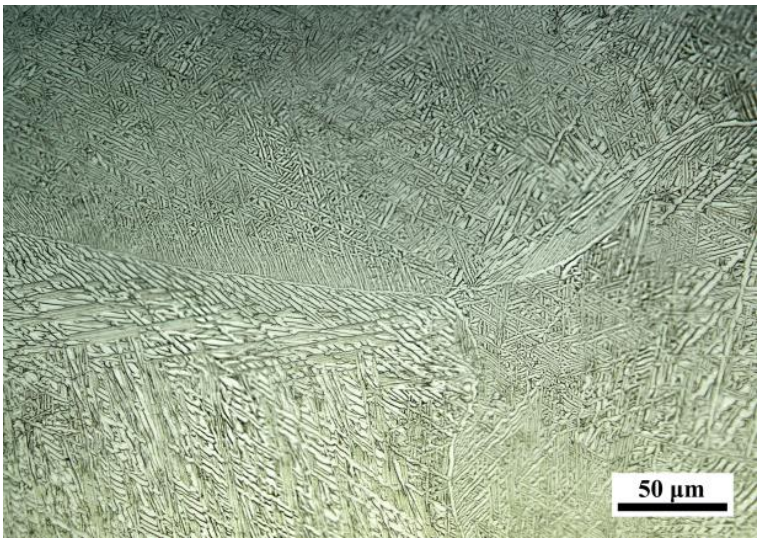

(c)

Figure 6-3 Optical micrographs of three selected specimens: (a) BM region; (b) HP region; (c) VP region.

6.3.1.2 Phase composition

The same specimens used for micrographs were also used for XRD measurement to determine the preferred orientation and the crystal phase of the alloy. As shown in **Figure 6-4**, the diffraction pattern for the BM, HP and VP samples presents eight broad peaks at 35.36°, 38.46°, 40.44°, 53.24°, 63.46°, 70.92°, 76.52°, 87.42° based on analysis using Jade software.

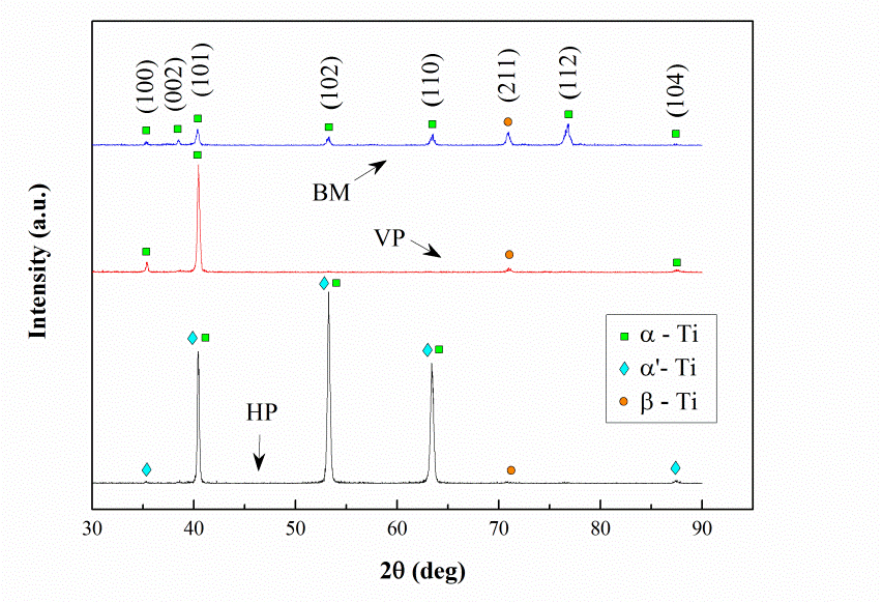

Figure 6-4 The XRD spectrums of three selected specimen from different planes

As can be seen from **Figure 6-4**, the microstructure of the BM sample presents a large number of α-Ti phases. These are replaced by predominantly α'-Ti phases in the HP of WAAM-fabricated Ti-6Al4V samples. It should be pointed out that only small amount of β-Ti phases are observed in the samples, which is attributed to the fact that the β-Ti phase is usually too minor or absent to be detected by X-ray [154]. Although both vertical plane and horizontal plane samples of WAAM-fabricated Ti-6Al-4V have similar microstructural composition, the relative fractions of the phases are still different, especially for the martensitic α' {102} and {110} crystallographic plane, displaying a large volume fraction in HP regions. This indicates that α' {102} and {110} planes are the preferred orientations of growth in the HP regions, which ultimately causes the microstructural evolution to vary along different directions.

6.3.1.3 Mechanical properties

The average hardness distribution of the specimens in the three selected regions for the

corrosion test is shown in **Figure 6-5**. As can be seen, both VP and HP regions have lower average hardness compared to BM regions, possibly due to the microstructural changes in these regions. Even with such a similar microstructural composition between HP and VP regions, discernible differences in average hardness still exist, displaying higher values in VP regions than HP regions. This is attributed mainly to the influences of grain size and phase orientation on dislocation distributions in the different planes.

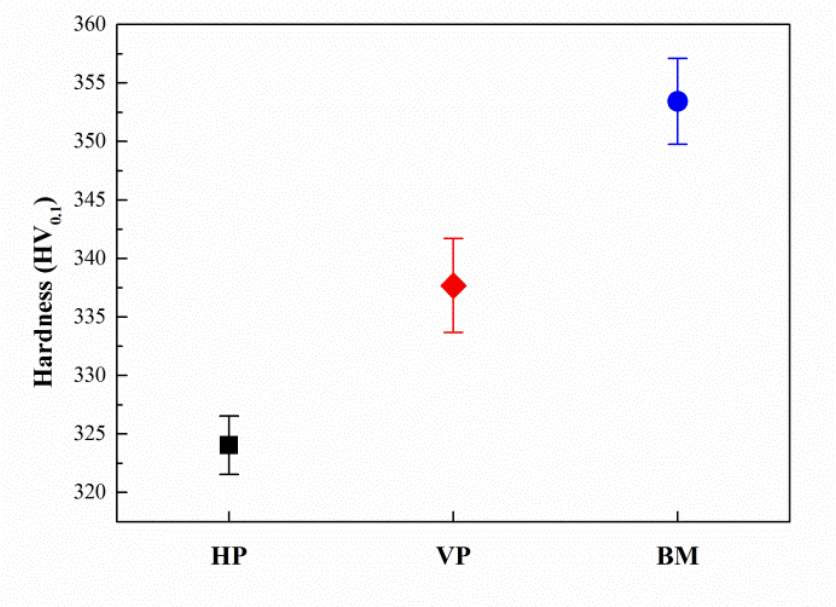

Figure 6-5 Average hardness values of three groups of specimens

6.3.2. Electrochemical studies

6.3.2.1 Open circuit potential (OCP)

Open circuit potential (OCP) is considered as an important parameter in estimating the tendency of metal corrosion. As shown in **Figure 6-6**, before performing other electrochemical tests, the variation of E_{OCP} with time was measured by immersing the samples in 3.5% NaCl solution. The E_{OCP} values of the as-received specimens increase with time, which indicates that the electrochemical process is controlled by the anodic reaction and

a protective oxide film starts to grow on the electrode surface. During immersion in the corrosive media, the newly formed oxide film may be dissolved, and then formed locally again. This simultaneous competition between film formation and dissolution brings an unstable electrochemical process to the electrode surface, consequently leading to fluctuating E_{OCP} values. In comparison to BM and VP samples, HP samples exhibit the most variation of E_{OCP} values owing to less homogeneous microstructures. After a certain immersion time, the oxide film on the electrode surface begins to stabilize and therefore, the E_{OCP} values approach a constant. As the immersion time approaches 60000 s, E_{OCP} values of all investigated samples stabilized at around −0.1 V, with slight differences between fabricated samples and wrought metal. It is well recognized that the nobler, or more positive, OCP indicates greater stability. Hence from **Figure 6-6**, the studied samples exhibit a tendency over time toward decreasing corrosion tendency.

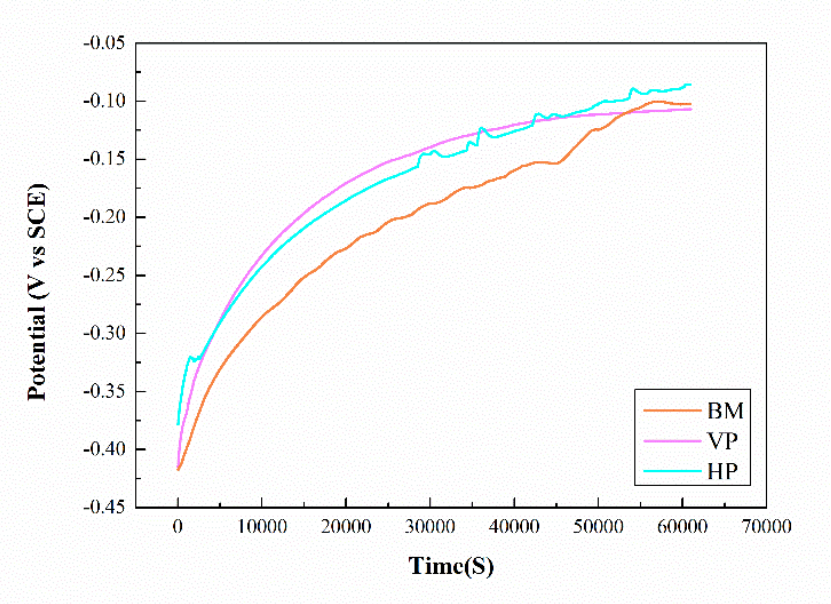

Figure 6-6 Open circuit potential (vs. SCE) of as-received samples in 3.5% NaCl solution.

6.3.2.2 Potentiodynamic polarization

In this study, the potentiodynamic polarization is used to calculate the kinetic parameters, including corrosion current density (I_{corr}), corrosion potential (E_{corr}) and Tafel slopes (b_a and b_c). Tafel extrapolation method was adopted as one of the most commonly used method for titanium corrosion test, including Ti6Al4V [155] and other kinds of titanium-based alloy [156]. Recently, there was report on investigation of corrosion resistance by the method of Tafel extrapolation on Ti6Al4V alloy fabricated by electron beam melting [157]. **Figure 6-7** shows the Tafel extrapolation results of the investigated specimens in 3.5 wt.% NaCl solution, and **Table 6-2** further details the analysis results. As can be seen, HP and VP samples display lower average E_{corr} values (−0.138 V and −0.131 V respectively) compared with the BM sample (−0.117 V), indicating slightly less corrosion resistance for both of them. Regarding the corrosion current density (I_{corr}) which generally reflects the corrosion rate for the materials, HP samples display the highest average I_{corr} value (16.0 nA/cm^2), followed by VP samples (14.2 nA/cm^2) and BM samples (12.1 nA/cm^2). Larger I_{corr} values indicate higher corrosion rates, so the BM samples show a better corrosion resistance compared to the WAAM-fabricated Ti-6Al-4V samples in NaCl solution. By this measure, the VP samples exhibit a lower corrosion rate than HP samples, in general agreement with E_{corr} values. Moreover, the BM samples demonstrate better repeatability in both E_{corr} and I_{corr} values due to more uniform microstructure, while VP and HP samples show greater variation, which is not only related to microstructural heterogeneity but also influenced by grain size and phase orientation. In terms of linear polarization resistance (R_p'), both sets of WAAM-fabricated Ti-6Al-4V samples have lower average values (2.27 MΩ cm^2 for VP, 2.23 MΩ cm^2 for HP)

in comparison to the wrought substrate (2.49 MΩ cm^2 for BM), suggesting poorer corrosion resistance, which is consistent with the results for E_{corr} and I_{corr}.

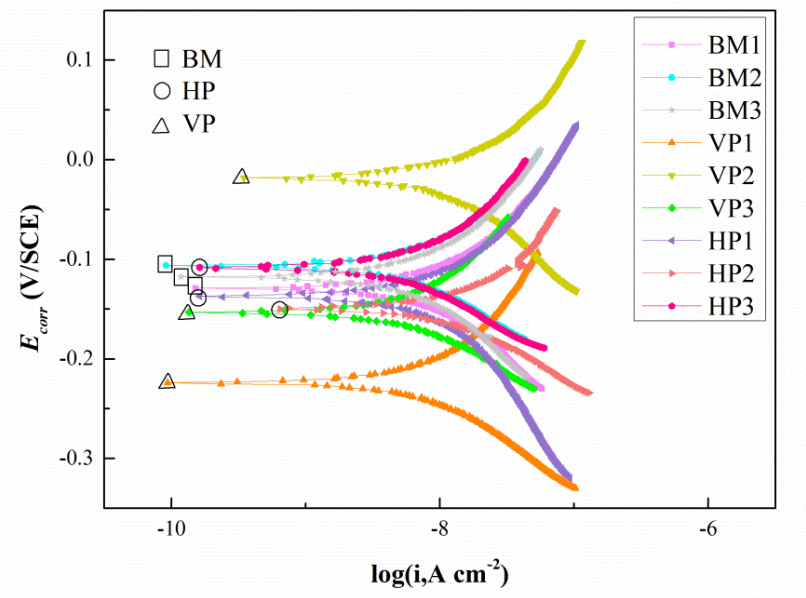

Figure 6-7 Potentiodynamic polarization plots of specimens

Table 6-2 Electrochemical kinetics parameters for test samples

Specimen	E_{corr} (V/SCE)	I_{corr} (nA/cm^2)	b_a (1/V)	$-b_c$ (1/V)	R_p' (MΩ cm^2)
V1	-0.224	11.6	5.19	10.11	2.44
V2	-0.018	20.8	4.83	7.47	1.70
V3	-0.153	10.3	3.77	12.12	2.66
H1	-0.137	19.5	4.32	4.44	2.54
H2	-0.15	20.0	4.86	11.89	1.28
H3	-0.108	8.33	5.99	12.22	2.86
B1	-0.129	15.5	4.06	7.97	2.32
B2	-0.106	8.34	6.78	12.88	2.66
B3	-0.117	12.6	4.61	8.62	2.50

Figure 6-8 shows the strong polarization curves of WAAM-fabricated Ti-6Al-4V and wrought Ti-6Al-4V. These tests were carried out in the potential range of −1 V to + 2V at a scan rate of 5 mV/s in 3.5 wt.% NaCl solution. According to Fig.8, all the investigated

specimens are characterized by one obvious passivation region where the increase of current density with potential is inhibited. When the corrosion potential (E_{corr}) of the electrode surface exceeds 0 V, the potentiodynamic curves deviate from the Tafel anodic line, meaning passivation behaviour begins to occur. In the passive regions, there is a slight difference in passive potential range (ΔE) between WAAM fabricated Ti-6Al-4V and wrought Ti-6Al-4V. To further evaluate the passivation process, the passive current density (i_p) can be identified in the magnified drawing in **Figure 6-8**. If the electrode surface shows higher passive current density, it is less likely to be passivated. As can be seen, HP samples exhibit the highest i_p value, followed by that of VP and BM samples, which suggests the HP samples exhibit a comparatively larger corrosion rate even in passive regions.

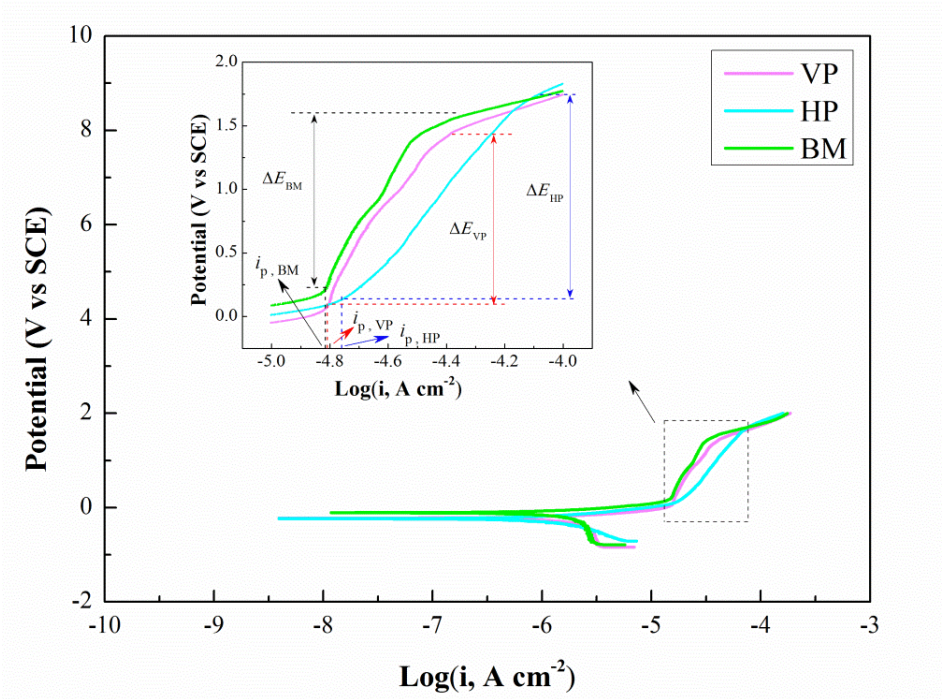

Figure 6-8 Strong polarization curves for WAAM-fabricated Ti-6Al-4V and ASTM standard Grade 5 alloy in 3.5wt% NaCl solution. The inset shows passive region from 0 V to 2 V.

6.3.2.3 Electrochemical impedance spectroscopy (EIS)

Figure 6-9 shows the Nyquist and Bode plots of the VP, HP and BM specimens in 3.5wt% NaCl solution. The equivalent circuit for fitting the EIS data is shown as an inset in **Figure 6-9 (a)**. For all the three sets of samples, since the Nyquist diagram (**Figure 6-9 (a)**) exhibits only an obvious capacitive loop, a Randles circuit with one time constant was selected as the equivalent circuit to fit EIS results. In the equivalent circuit, R_s is the solution resistance, R_f refers to film resistance of the passive film, and the constant phase element (CPE) represents film capacitance, which can be expressed as [158]:

$$Z_{CPE}=Y_0^{-1}(j\omega)^{-n} \tag{6-1}$$

where Y_0 is true capacitance of the passivation layer, j is imaginary unit, ω is angular frequency and n is related to the constant phase angle[159, 160]. The detailed EIS fitting data are summarized in **Table 6-3**. A smaller value of χ^2 indicates a better fit between the equivalent circuit and experimental results.

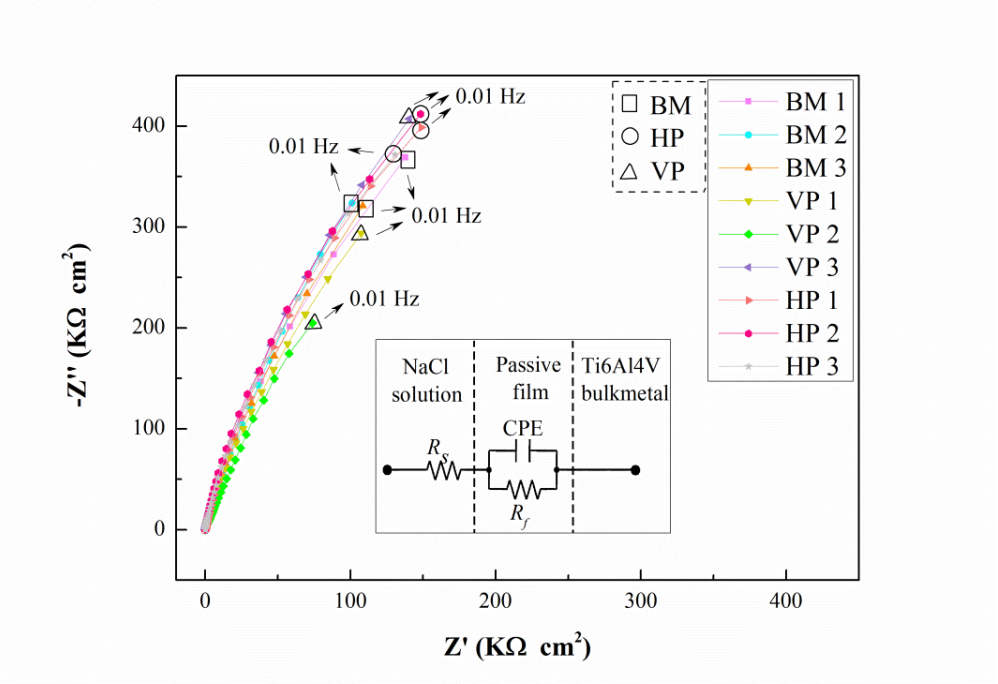

(a)

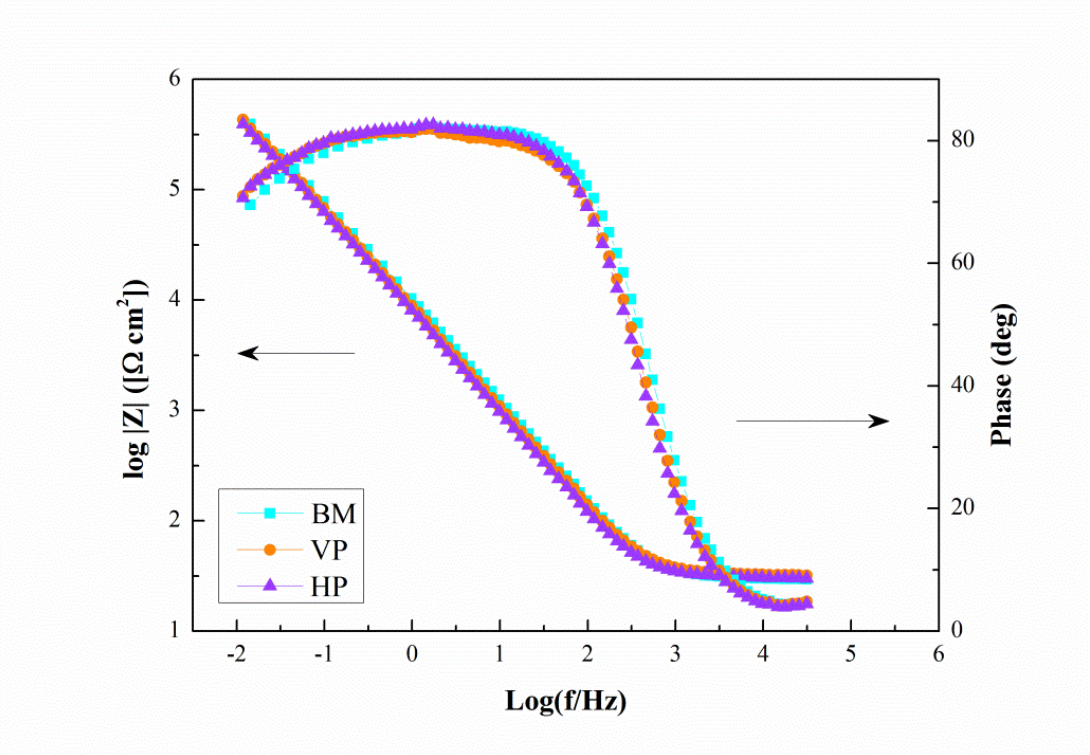

(b)

Figure 6-9 EIS results of test samples: (a) Nyquist plots with inset showing the equivalent circuit: (b) Bode plots.

According to the data listed in **Table 6-3**, for HP, VP and BM samples, the solution resistance (R_s) values in 3.5. wt.% NaCl solution are very similar, however there are significant differences in passive film resistance (R_f).While BM samples display the highest value of R_f (average value 1.68 MΩ cm^2), VP samples exhibit a significantly lower average R_f value (195 kΩ cm^2), but distinctively higher than that of HP samples (average 174 kΩ cm^2). Generally, a higher R_f value of passive film implies better corrosion resistance. Based on these results, WAAM-fabricated Ti-6Al-4V has an inferior corrosion resistance when compared to wrought Ti-6Al-4V. The value of n represents the degree to which the constant phase element (CPE) acts as a purely capacitive element, with diminished contribution of a

resistive component. All the investigated Ti-6Al-4V specimens have *n* values close to the number 1.0, so the CPE in the equivalent circuit closely resembles an ideal capacitor. In order to further evaluate the metal surface condition immersed in NaCl solution, the passive film thickness can be estimated using the parallel plate capacitor equation:

$$d = \frac{\varepsilon \varepsilon_0 A}{C} \tag{6-2}$$

where d presents the thickness of the passive layer, ε is the relative permittivity of the film, ε_0 is permittivity of vacuum, A is the exposed area of the working electrode and C is related to the value of Y_0, CPE. According to this relationship, the passive film produced on the surface of BM specimens (average *Yo* 25.9) is expected to be thicker on average than that of VP specimens (average *Yo* 29.5) HP specimens (average *Yo* 31.8) when evaluated in 3.5 wt.% NaCl solution.

Table 6-3 EIS parameters of equivalent circuit for test samples

Specimen	R_s (Ω cm^2)	CPE, Y_0 (10^{-6}S Sec^n cm^{-2})	n (1/V)	R_f (MΩ cm^2)	χ^2 (10^{-3})	d (nm)
V1	30.4	28.5	0.895	0.137	2.93	61.1
V2	31.0	37.0	0.847	0.148	4.73	47.1
V3	32.0	22.9	0.899	0.301	5.16	75.9
H1	30.2	24.4	0.913	0.173	2.00	71.3
H2	30.8	48.7	0.832	0.125	2.30	35.8
H3	29.6	22.3	0.916	0.185	1.93	77.9
B1	29.5	19.2	0.913	1.47	2.51	90.8
B2	31.2	27.1	0.889	2.04	2.53	64.2
B3	30.5	24.3	0.908	1.52	2.83	71.6

6.4 Discussion

6.4.1. Microstructural evolution

For the VP, HP and BM regions, the main variation in microstructure is the generation of

martensite lamellae α with Widmanstätten structure and acicular α' structure due to the differences in thermal behaviour at each location. As layers are successively deposited during the WAAM process, the cooling rate progressively decreases for higher layers, and this contributes to the variation in microstructural evolution.

The conductive thermal resistance from the uppermost deposited layer to the substrate is significantly increased with increasing wall height. As titanium alloys exhibit poor thermal conductivity, a decreasing fraction of the heat input from the gas tungsten arc welding process is conducted away through the substrate, while an increasing amount of heat is dissipated to the surrounding atmosphere via convection and radiation, which leads to a slower cooling rate in the building direction (VP) than in the travel direction (HP) [141]. Therefore, as shown in **Figure 6-10**, upon high cooling rates from the β phase field, the transformation from β phase to α phase occurs by a displacive transformation to form acicular martensite structures along the travel direction (HP). Generally, these acicular martensite structures consist of mixtures of individual α' plates each belonging to different Burger orientations [161] (**Figure 6-10b**), and will lose their hexagonal structure to a orthorhombic α'' structure with the β stabilizing solute increase [142]. Conversely, due to slow cooling rates along the building direction (VP), the α phase nucleates preferentially at the prior β grain boundaries at first, forming a continuous layer named the grain boundary α (α_{GB}), which always exhibits a Burgers orientation related with one of the prior β grains [162]. Afterwards, the nucleation of α lamellae occurs in the grain interior so that basketwave Widmanstätten α forms in pseudo-random fashion within the remaining β structure (**Figure 6-10c**).

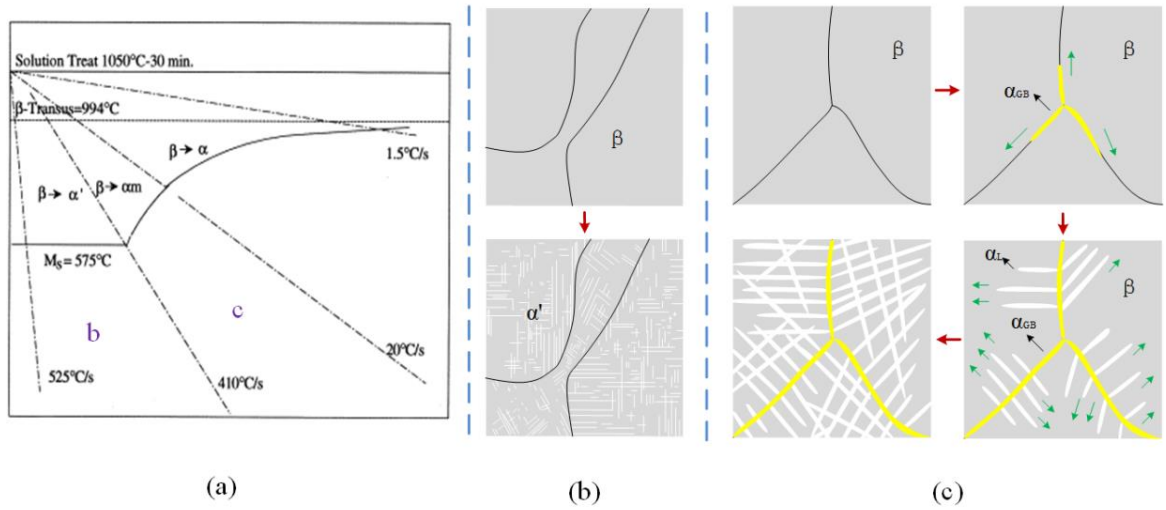

Figure 6-10 Schematic of microstructural evolution for WAAM-fabricated of Ti-6Al-4V: (a) Continuous cooling diagram for Ti–6Al–4V β-solution treated at 1050°C for 30 min (Ms temperature due to Majdic and Ziegler) [142], (b) HP regions, (c) VP regions.

Referring to the hardness measurements in **Figure 6-5**, higher values are measured in the BM samples, followed by VP and then HP. These disparities are obviously associated to the formation of α and α′ martensite microstructure. Generally, the martensitic lamellae α at VP show a higher hardness value in comparison with martensite α′ at HP due to its comparatively larger grain size and the formation of grain boundaries. For Ti-6Al-4V α + β structures, the Vickers hardness decreases with grain size and the thickness of lamellar α phase increasing due to its positively proportional to strength of alloy[163]. Therefore, slightly high hardness value at VP is also beneficial to corrosion resistance improvement.

6.4.2 Electrochemical evaluation

The findings of the electrochemical tests in 3.5 wt.% NaCl solution are useful in assessing the comparative corrosion resistance of the investigated specimens. As described in **Figure 6-6**, rising OCP values indicate that a stable passive film forms on the electrode surface and these passive films play a key role in protecting inner metal from further

corrosion. Potentiodynamic polarization and EIS results suggest that the wrought Ti-6Al-4V possesses higher corrosion resistance than WAAM-fabricated Ti-6Al-4V in which inner planes parallel to the build direction (VP) show slightly better corrosion properties on average than those planes that are perpendicular to the build direction (HP). The electrochemical test results that are critical for an in-depth understanding of the corrosion resistance of WAAM-fabricated Ti-6Al-4V and wrought Ti-6Al-4V are shown in **Figure 6-11**.

In general, material properties are closely related to microstructure, and this is particularly the case for corrosion resistance. For WAAM-fabricated Ti-6Al-4V, the formed lamellae α and acicular α' grains are always present as a non-equilibrium structure that is believed to have a high energy state due to inadequate atomic diffusion during solidification. This attribute ultimately leads to unstable microstructures[74] and produces inferior corrosion resistance, as has been measured in this study using in 3.5 wt. % NaCl solution. Also, for the selective corrosion of α phase and α' phase, the dissolution rate of α phase is lower than that of α' phase on the surface of specimens at open circuit potential due to the comparatively hard grain [164]. Therefore, the HP regions with acicular α' phase, which is in a "higher energy state" and metastable, has inferior corrosion resistance compared to the VP regions with lamellar α structure. It needs to be noted that the greatest difference in these two types of microstructures is their grain size. In corrosive media, both of these massive grains perform as effective buffer films, contributing to the reduction of the galvanic effect between α and β phase. However, in comparison with acicular α' structure, the lamellar α structure possesses a higher density of nucleation sites for passivation during the corrosion process[165], which

leads to a thicker passive film and lower corrosion rate[166]. Accordingly, an averagely better corrosion resistance is obtained in VP regions of WAAM-fabricated Ti-6Al-4V.

For Ti-6Al-4V alloy with α + β microstructure, the Al and V elements are usually acting as respective stabilizers for α phase and β phase, and these segregation of elements always leads to an intrinsic difference in the corrosion resistance of α phase and β phases [167]. In corrosive solutions, if more preferential dissolution of α phases exist, the corrosion rate will be accelerated [168], while β phase is comparatively resistant to corrosion and improves corrosion resistance. Based on the XRD results, although only small amounts of β-Ti phases were detected in all the investigated specimens, difference in the β-Ti phase content still exist. It is observed that more β grains are detected in BM regions, which means enhanced corrosion resistance. Meanwhile, this is also one of the reasons that why the BM samples have higher hardness values than the WAAM-fabricated areas.

In addition, it is worth noting that the microstructural uniformity of investigated specimens not only has a direct effect on the corrosion resistance of the metal, but also brings a serious impact to the repeatability of electrochemical results. In this study, the BM samples have more uniform microstructures than WAAM-fabricated samples, and that is reflected in the consistency and repeatability of measurements. However, even in adjacent regions of fabricated Ti-6Al-4V, the examined microstructure is markedly inhomogeneous, producing significant fluctuations in the electrochemical test results. The surface of samples subtracted from vertical direction (VP), like geological layers, consists of a greater variation of microstructures than that of HP samples. As the active area of corrosion electrodes is relatively small, the greater heterogeneity of VP samples results in the greater variation of

electrochemical corrosion test results. Regardless of the individual, localized influences created by microstructural non-uniformities, the overall findings remain relevant. The anisotropic microstructure resulting from the WAAM processing of Ti-6Al-4V has a significant effect on the corrosion performance. Any future improvement to the process that aims to improve this aspect must address the mechanisms that produce microstructural anisotropy. It is well acceptable that the microstructural evolution is essentially dependent on the thermal history of the process that involves alternate re-heating and re-cooling cycles. That is to say, if the thermal state during deposition is properly controlled, the desired microstructures and more uniform properties with acceptable performance can be achieved. Based on this interpretation, an innovative wire arc additive manufacturing (WAAM) process with interpass heat sink will be further developed, trying to obtain more uniform microstructures and properties through the reasonable control on thermal state to fabricated part.

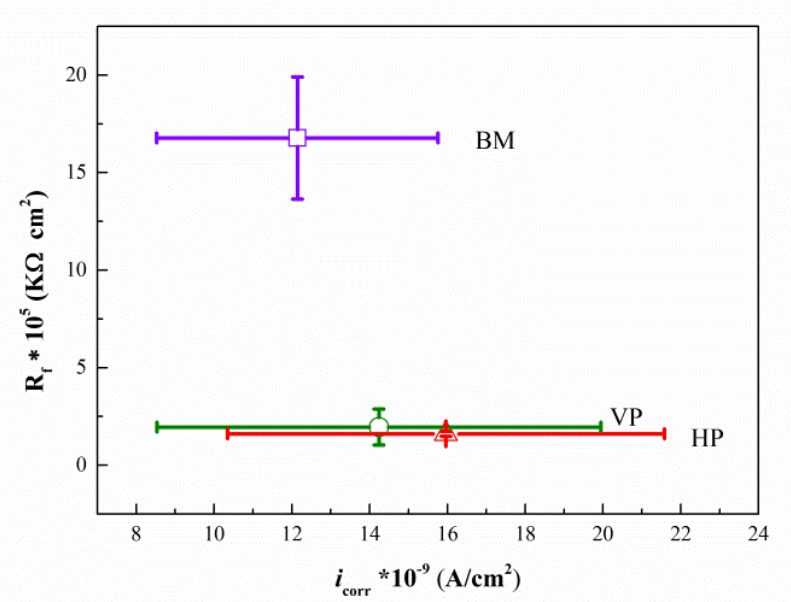

Figure 6-11 The comparison in corrosion resistance of WAAM-fabricated Ti-6Al-4V and wrought base metal in 3.5% NaCl solution.

6.5 Conclusion

The effects of directional microstructures on the corrosion properties of Ti-6Al-4V parts fabricated with wire are additive manufacturing (WAAM) technology have been investigated, and these corrosion properties have been compared against the performance of ASTM standard wrought-Ti-6Al-4 alloy. As the WAAM component is built up from the substrate, the conductive thermal resistance through the deposited material varies along different orientations. A relatively slower cooling rate occurs in the build direction (VP-vertical plane), contributing to the formation of large and hard lamellar α grains that are interwoven with a Widmanstätten structure. Meanwhile, a comparatively faster cooling rate occurs in the travel direction (HP-horizontal plane), producing smaller and softer α' grains. The resulting differences in phase structure, grain size and orientation creates a greater susceptibility to corrosion in the HP orientation compared to the VP orientation, as found by testing in 3.5% NaCl solution. Furthermore, WAAM-fabricated Ti-6Al-4V in both VP and HP orientations exhibits a lower passive film thickness than wrought Ti-6Al-4V, indicating higher corrosion rates and inferior corrosion resistance. In addition, the non-uniform microstructures produced in WAAM fabrication are not only responsible for the anisotropic corrosion behaviour, but also lead to greater variation in corrosion test results. To address this shortfall in the potential service life of additively manufactured Ti-6Al-4V components that are to be used in corrosive environments, further improvement of the WAAM process are needed, to address the mechanisms that produce microstructural anisotropy.

Chapter 7 THE FORCED INTERPASS COOLING

7.1 Introduction

For a Ti6Al4V component that is produced by WAAM, the microstructures are complex, often varying spatially within the deposition due to its complex thermal history that involves alternate re-heating and re-cooling cycles [169]. Even for adjacent regions within a deposit, differences in microstructure still exist, ultimately bringing inhomogeneous material performance to the component. To date, numerous investigations have been carried out to reveal microstructural formation mechanisms through the investigation of thermal history in WAAM deposition, with the aim of offering some helpful directions to solve these problems. For example, Wu et al. [141] observed that heat accumulation during additive fabrication has significant effects on the stability of gas tungsten wire arc additive manufactured Ti6Al4V alloy, which demonstrates the importance of in-process temperature monitoring and control. Suryakumar, et al. [170] claimed that depending on the thermal cycles in WAAM-fabricated steel, coarse grained microstructures with inhomogeneous hardness are formed along the building direction. These findings suggest that there is a tremendous need for microstructural optimization through improvements in process control of additive manufacturing.

As mentioned above, the solidification microstructure, including grain size and morphology, is essentially dependent on the thermal history during the manufacturing process. That is to say, if the thermal state during deposition is properly controlled, the desired microstructures and resulting mechanical properties with acceptable performance can be achieved. Based on this interpretation, recent studies by Henckell et al. [171] have attempted

to employ additional cooling gas for WAAM fabrication of low alloy steel components. Interestingly, applying an additional post-weld cooling gas of nitrogen with 5% hydrogen improves both the layer geometry and mechanical properties through grain refinement and homogenous hardness. Additionally, the different gas types used in deposition produce varying material properties, and further investigations were proposed that would employ carbon dioxide or pure nitrogen. It is well known that CO_2 gas cooling is commonly employed in Low Stress No Distortion (LSND) welding to reduce residual stress and deformation. According to Holder et al. [172], the heat affect zones of DH-36 steel welds show significant changes in hardness when subjected to conventional gas metal arc welding and LSND welding processes. Based on such findings, if CO_2 gas is used to dynamically cool the deposits during the WAAM process, it is possible that similar effects on material properties can be obtained.

In this study, gas tungsten arc welding based WAAM (GT-WAAM) with forced interpass cooling using compressed CO_2 gas is applied to Ti6Al4V, with the aim of improving material properties. The effects on surface oxidation, geometrical features, microstructural evolution, and mechanical properties are investigated through the use of WAAM with and without CO_2 gas cooling. Firstly, the interpass temperature is controlled (i.e. allowed to decrease through natural convection and conduction before deposition of the next layer) to a number of constant values, aiming at an understanding of the effects of interpass temperature on the targeted deposition properties. Subsequently, forced interpass cooling is implemented, aimed at an improvement of material properties. A detailed analysis and discussion of the results is used to assess the possibilities for controlling the properties of WAAM-fabricated Ti6Al4V

by using this method.

7.2 Experimental Procedures

7.2.1 Experiment setup

The apparatus consists of a 200A-rated GTAW power source, “cold” wire feeder, water cooling unit and travel mechanism, as shown in **Figure 7-1**. An IR pyrometer was used to measure the in-situ interpass temperature, thereby controlling the dwell time between deposition of layers. The feedstock used in this study was ASTM B863 grade 5 Ti6Al4V wire with a diameter of 1.2mm, deposited onto a Ti6Al4V substrate with dimensions of 200 mm × 150 mm × 6 mm that conforms to ASTM B265 specification. Three straight wall structures were fabricated at respective interpass temperatures of 100 °C, 200 °C, and 300 °C using the GT-WAAM system with localized gas shielding. The process parameters are provided in **Table 7-1**. Welding grade argon (99.995% purity) was used as the shielding gas for both GTAW torch and trailing shield.

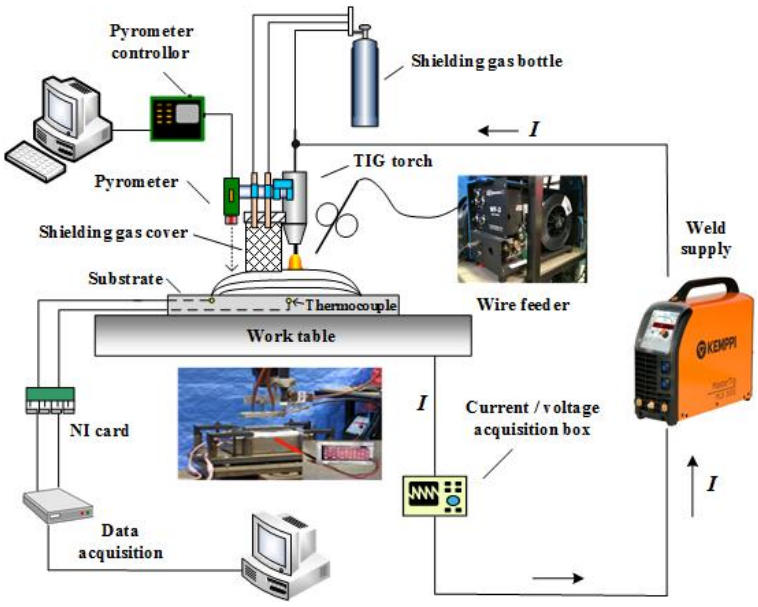

Figure 7-1 Schematic diagram of the GT-WAAM system

Table 7-1 Process parameters for WAAM deposition

Process parameters	Details	
Deposition power	Current	110A
	Arc voltage	13V
Speed	Travel speed	95mm/min
	Wire feed speed	820mm/min
Distance and angle	Electrode to workpiece	3 mm
	Electrode to filler wire	60°
Flow rate(argon)	GTAW torch	15 L/ min
	Trailing shield	10 L/ min
Time	Post flow duration	35 seconds

7.2.2 Forced interpass cooling

In order to evaluate the effectiveness of forced interpass cooling, a commercially-available CO2 cooling spray nozzle was fitted to the GTAW torch as shown in **Figure 7-2.** A flow rate of 215g/min was used to deliver a stable CO_2 cooling stream, according to the manufacturer's specifications. The cooling spray was initiated after deposition of each layer was completed in order to avoid arc disruption caused by the relatively turbulent CO_2 flow. Cooling flow was stopped when the interpass temperature decreased to room temperature.

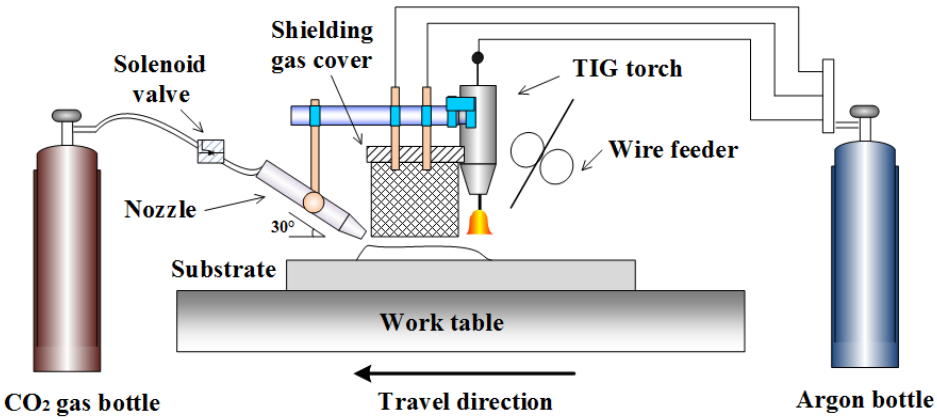

Figure 7-2 Schematic diagram of the GT-WAAM deposition system with forced interpass cooling

7.2.3 Material characterization techniques

Both metallographic specimens and mechanical test samples were extracted from the fabricated Ti6Al4V walls for further investigation. The metallographic specimens were hot mounted, ground and polished according to standard procedures, and then etched in Kroll's reagent containing 2% vol HF, 6% vol HNO_3 with balance H_2O. The macrostructures were examined using a Leica M205A deep field stereoscopic microscope and the microstructures were observed using a Leica DMR optical microscope (OM). Vickers hardness testing was performed with a DuraScan 70 automatic hardness tester using a test load of 100g and a dwell time of 15s according to ASTM: F2924 standard. Tensile tests were carried out at room temperature at a constant crosshead displacement rate of 0.4mm/min using a MTS370 universal testing machine. The tensile test samples extracted from the fabricated walls are shown in Figure 3.

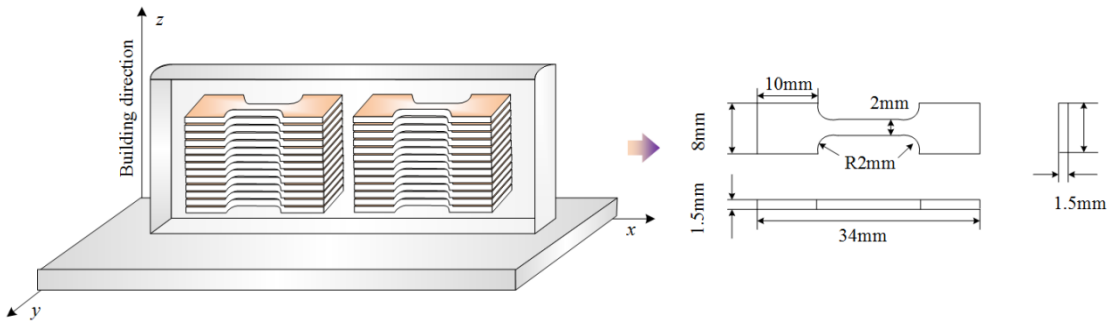

Figure 7-3 Schematic diagram of extracted tensile samples

7.3 Results

7.3.1 Deposition geometry

Figure 7-4 shows the dimensions of WAAM-fabricated Ti6Al4V walls at different

interpass temperature. When the interpass temperature increases from 100°C to 300°C, the height of the deposited wall is reduced by 11.7%, whereas its width increases to 12.2%. Interpass temperature has a significant effect on build geometry, even though all other process parameters are unchanged, including the number of layers. Also, the dimensions of the wall deposited using forced interpass cooling are almost identical to those of the wall built with an interpass temperature of 100 °C. This indicates that forced interpass cooling not only reduces the build time, but also has the advantage of maintaining deposition accuracy.

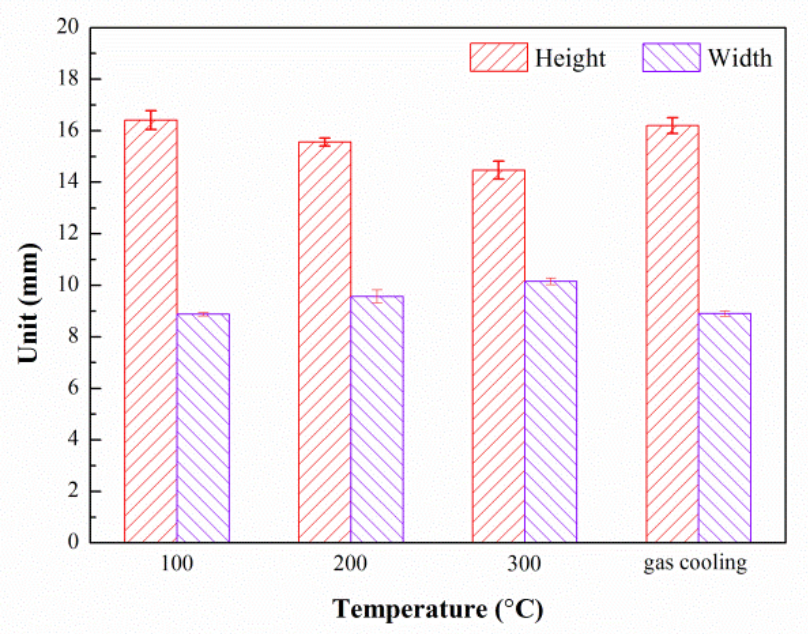

Figure 7-4 Effect of interpass temperature on wall dimensions

7.3.2 Surface oxidation

The images in **Figure 7-5** show that different degrees of surface oxidation can be observed at various interpass temperatures. For **Figure 7-5 (a)**, the interpass temperature is allowed to return to 100 °C through natural convective and conductive cooling. The initially low temperature at the start of the next deposited layer essentially eliminates the effects of

heat input from the newly deposited layer, so the surface of fabrication shows a clean surface with only a very slight sign of oxidation as indicated by the light straw color. As the interpass temperature is increased from 100°C to 200 °C and then 300 °C, more surface oxidation is generated, and the surface colour changes from light straw to dark blue and then powdery grey, indicating unacceptably high levels of surface contamination. For the component produced with forced interpass cooling, **Figure 7-5(d)** shows that the surface has only a small amount of oxidation as indicated by coloration, and possibly better than that of deposition with a naturally-cooled interpass temperature of 100 °C. The potentially better result with forced cooling may be due to superior cooling of the zone beyond the uppermost layer. This would allow the heat input from the newly deposited layer to be better absorbed by the specific heat capacity of the previously deposited material, keeping the surface temperature sufficiently low to avoid absorption of atmospheric oxygen after the shielding gas is turned off at the end welding. These results suggest that rapid CO_2 gas cooling during the dwell interval is beneficial for avoiding post-deposit oxidation titanium when using WAAM with localized gas shielding in an otherwise open atmosphere.

(a)

(b)

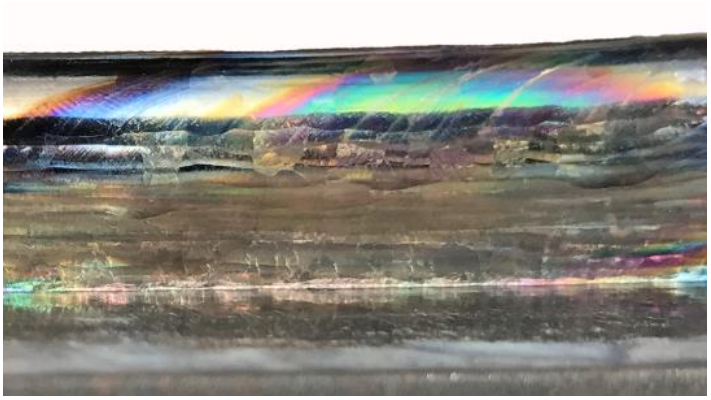

(c)

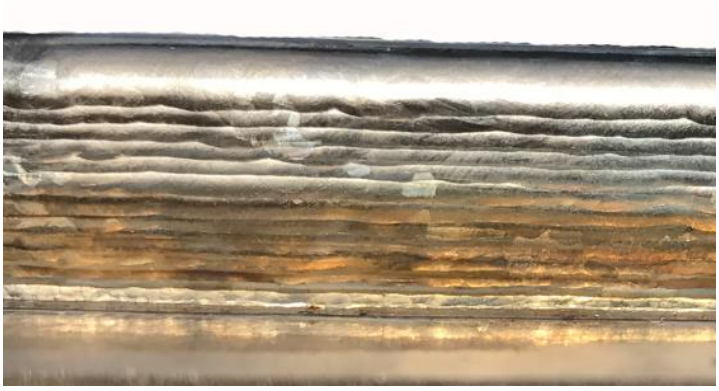

(d)

Figure 7-5 The surface appearance of Ti6Al4V parts fabricated at different process conditions: (a) 100°C; (b) 200°C; (c) 300°C; (d) Forced cooling with CO_2 gas

7.3.3 Macrostructure

Figure 7-6 shows the cross-section macrograph of the four as-fabricated Ti6Al4V walls. Three distinct regions are discernible on the etched cross-section: the substrate regions with

concave bands (R_3), the bottom regions with parallel bands (R_1) and the top regions (R_2) with convex bands.

The concave band is apparently determined by the field of heat affected zone which expands at high interpass temperature on the substrate. However, when the interpass temperature is controlled at 300 °C, there are no obvious convex bands and the microstructure produced in the substrate region is homogeneous, possibly attributing to the large grain growth at low cooling rates. For the parallel bands and convex bands, which are present in the majority of the deposits, their number varies with interpass temperature. **Figure 7-7** further displays the proportion ratio (R_1/R_2) between two types of bands at different process conditions. It can be observed that the number of parallel bands significantly decrease with increasing interpass temperature, while the changes in convex bands is the exact opposite. For the deposit produced using forced interpass cooling, the area of convex bands regions is almost equal to that of parallel bands regions, as shown in **Figure 7-6d** and **Figure 7-7**. The vertical spacing of the bands in the parallel and convex regions of the deposit produced using forced interpass cooling is visibly greater than the spacing of the bands seen in any of the other deposits, considered to be a result of consistently higher cooling rate.

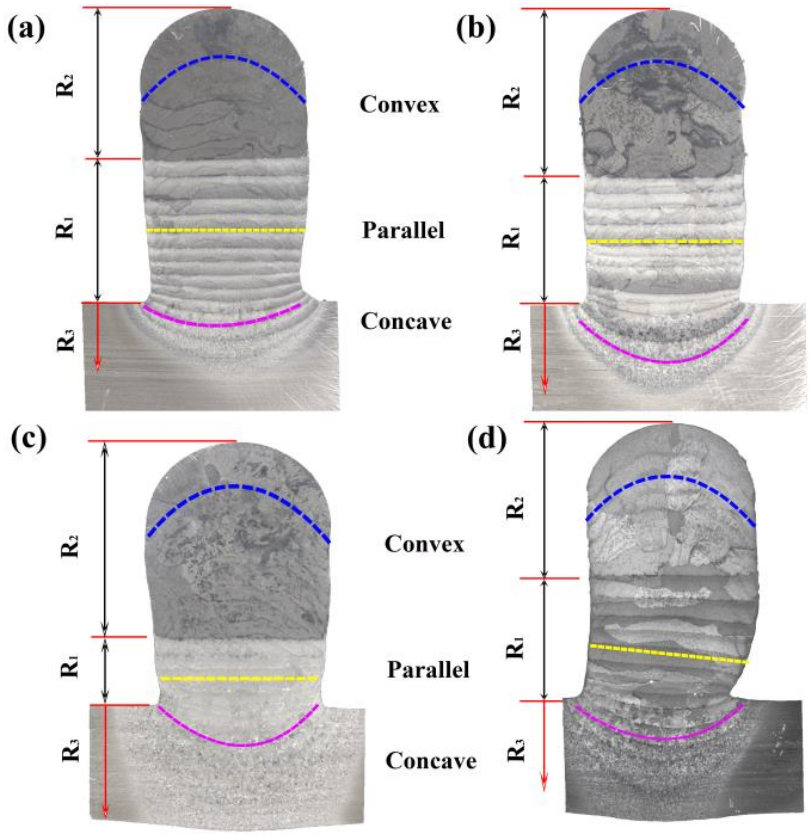

Figure 7-6 The cross-section morphology of Ti6Al4V component fabricated at : (a)100°C; (b) 200°C; (c) 300°C;(d) forced interpass cooling with CO_2 gas

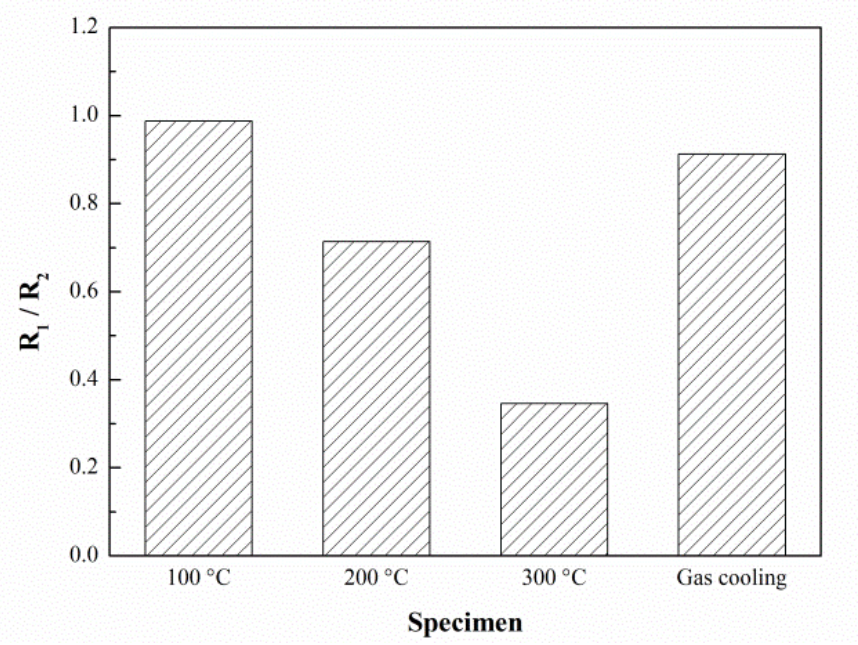

Figure 7-7 The area ratio of parallel band regions and convex band regions for different process conditions

7.3.4 Microstructure

Figure 7-8 shows the microstructure of the as-fabricated Ti6Al4V parts, examined along the building direction. Due to the influences of thermal gradient and solidification rate, near-equiaxed beta grains (**Figure 7-8a**) are formed in the substrate regions, lamellar α interwoven with a coarse Widmanstätten structure are produced in the parallel band regions (**Figure 7-8b**), and acicular α interwoven with a basketweave structure are generated in the convex band regions (**Figure 7-8c**). Similar microstructural evolution has been reported for fabrication using electron beam deposition [173] and laser additive manufacturing [174]. It is well known that deposited Ti6Al4V mainly consists of α', α and β phases, and only α' phase is formed at high cooling rates. As can be seen from **Figure 7-8**, the microstructures and grain size in parallel and convex band regions are not significantly influenced by interpass temperature, possibly due to the similar heat dissipation behaviour at the same locations within each of the produced parts. However, for convex band regions with high interpass temperature, the grains are obviously large and the microstructure is more uniform due to grain growth at low cooling rates. For the part deposited using CO_2 gas interpass cooling, comparatively more acicular α phases can be observed in both convex band and parallel band regions. That is to say, when rapid interpass cooling is applied, the large amount of lamellar α phase would be replaced by acicular α phase, at the same time accompanied with refined grain.

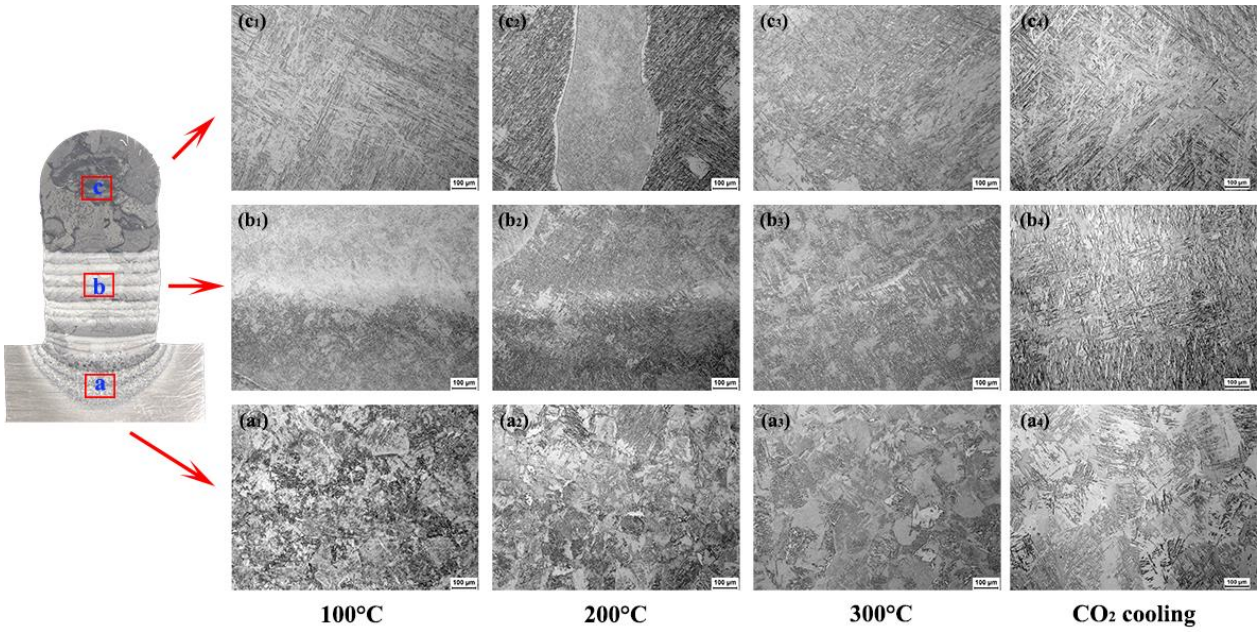

Figure 7-8 The microstructures of parts fabricated under different process conditions

7.3.5 Hardness

Figure 7-9 shows the microhardness distribution along the vertical centerline of the cross-section of the Ti6Al4V parts fabricated under different process conditions. There is no obvious change in the average hardness values when the interpass temperature is increased from 100 °C to 300 °C, but the deposition with CO_2 gas cooling exhibits a slightly higher average hardness value, which is attributed to comparatively more acicular α phase and grain refinement. Despite the markedly different appearances of band structures in the top and bottom regions, the microhardness is almost unchanged, suggesting that the difference in α phase volume is not responsible for the hardness performance, as similarly explained by Baufeld et al [67].

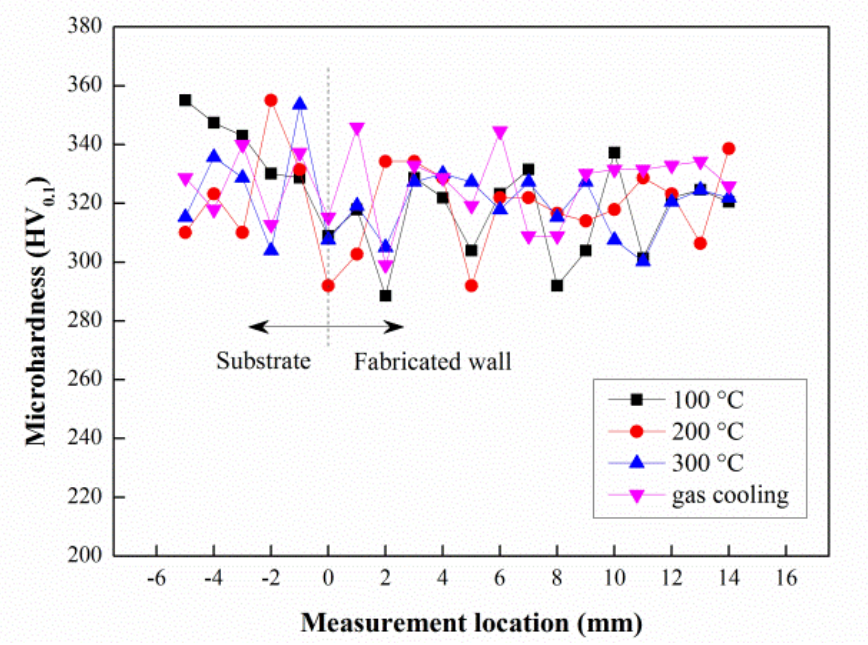

(a)

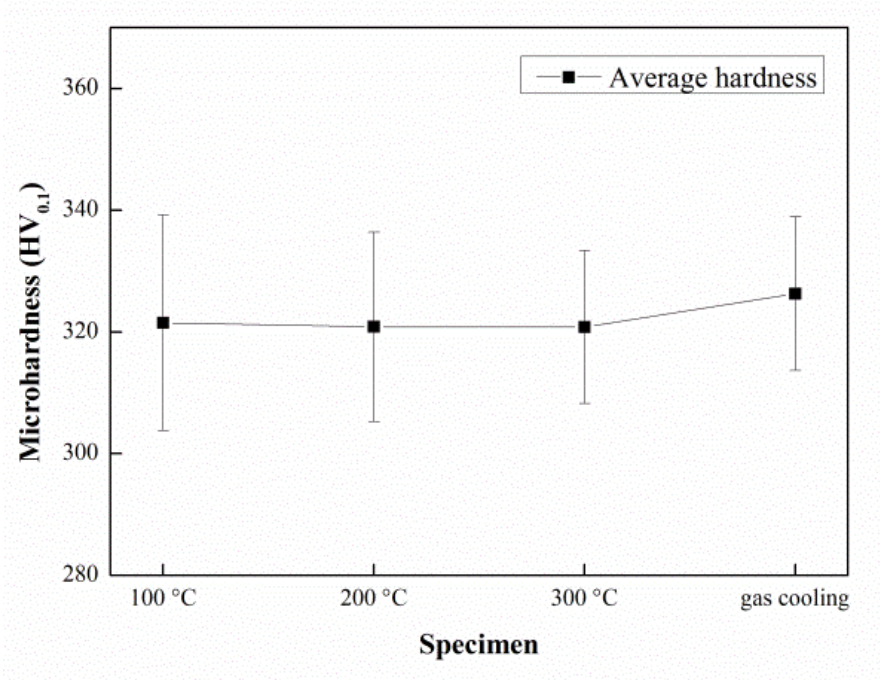

(b)

Figure 7-9 Hardness profiles of specimens: (a) Hardness distribution; (b) Average hardness

7.3.6 Mechanical property

Figure 7-10 shows the ultimate tensile strength (UTS) and elongation of tensile

specimens derived from different locations within the four parts produced under different process conditions. The UTS is sensitive to the locations within the build, decreasing along the build height even though the various interpass temperatures were controlled throughout the build height, as seen in **Figure 7-10a**. However, the elongation of these tensile specimens shows a slight increase and then a decrease from bottom to top of the deposit, as shown in **Figure 7-10b**. From both of these results it is evident that the mechanical properties are asymmetrical within the WAAM deposit. In addition, as a result of the combined effects from grain size and oxidation behaviour, a significant decrease in both average tensile strength and elongation is observed with increasing interpass temperature (**Figure 7-10c**). The deposit produced with additional CO_2 gas interpass cooling shows slightly higher UTS and lower elongation compared to those deposits produced without forced cooling, suggesting that interpass cooling is beneficial to the material properties of WAAM-fabricated Ti6Al4V components.

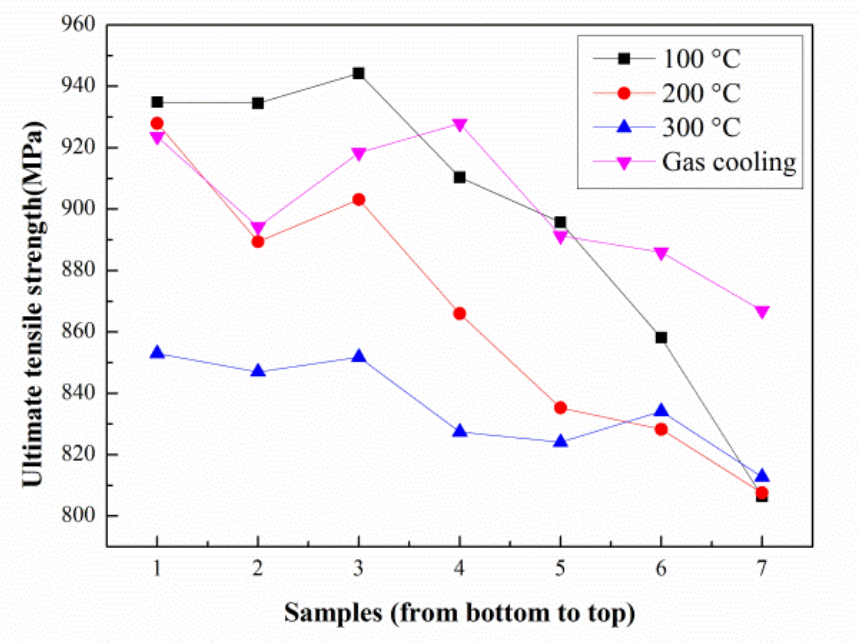

(a)

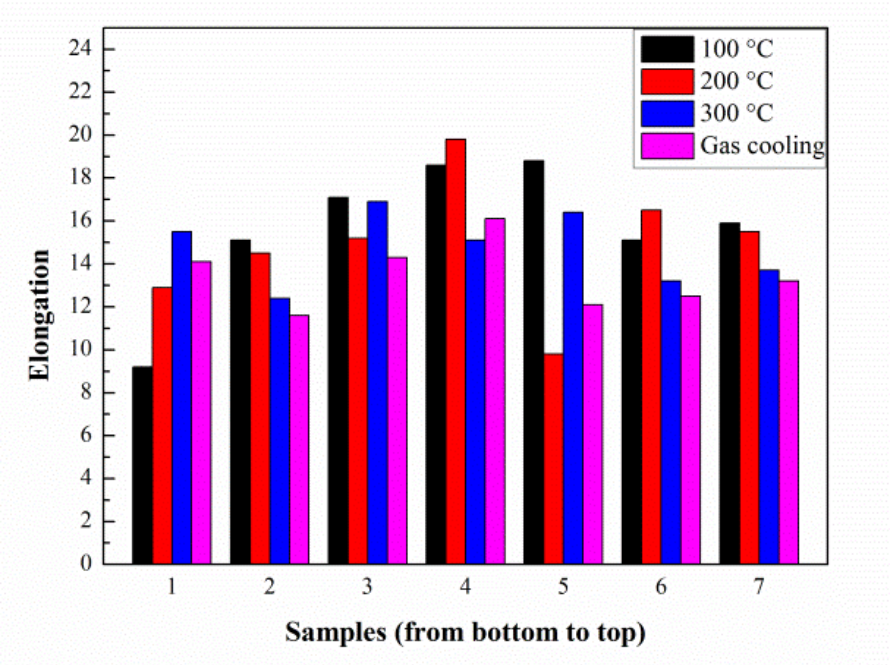

(b)

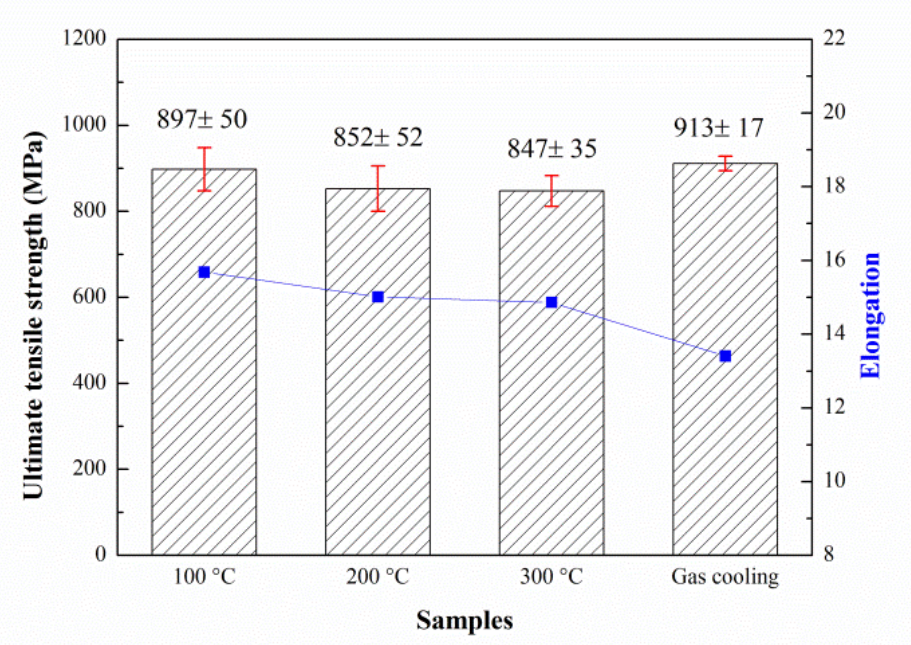

(c)

Figure 7-10 The mechanical properties of obtained specimens

7.3.7 Fracture behaviour

Figure 7-11 displays the fractographs the tested tensile samples. All the tensile samples

present ductile morphology with a large number of shallow and stretched dimples in response to fracture. There is no significant difference in the fracture features among all the components that have been produced with different process conditions. However, the fracture surface of the specimen fabricated with an interpass temperature of 300 °C presents small amounts of lamellar structures, indicated within the red rectangle in Fig.11c, which demonstrates rapid crack growth along the crystallographic planes.

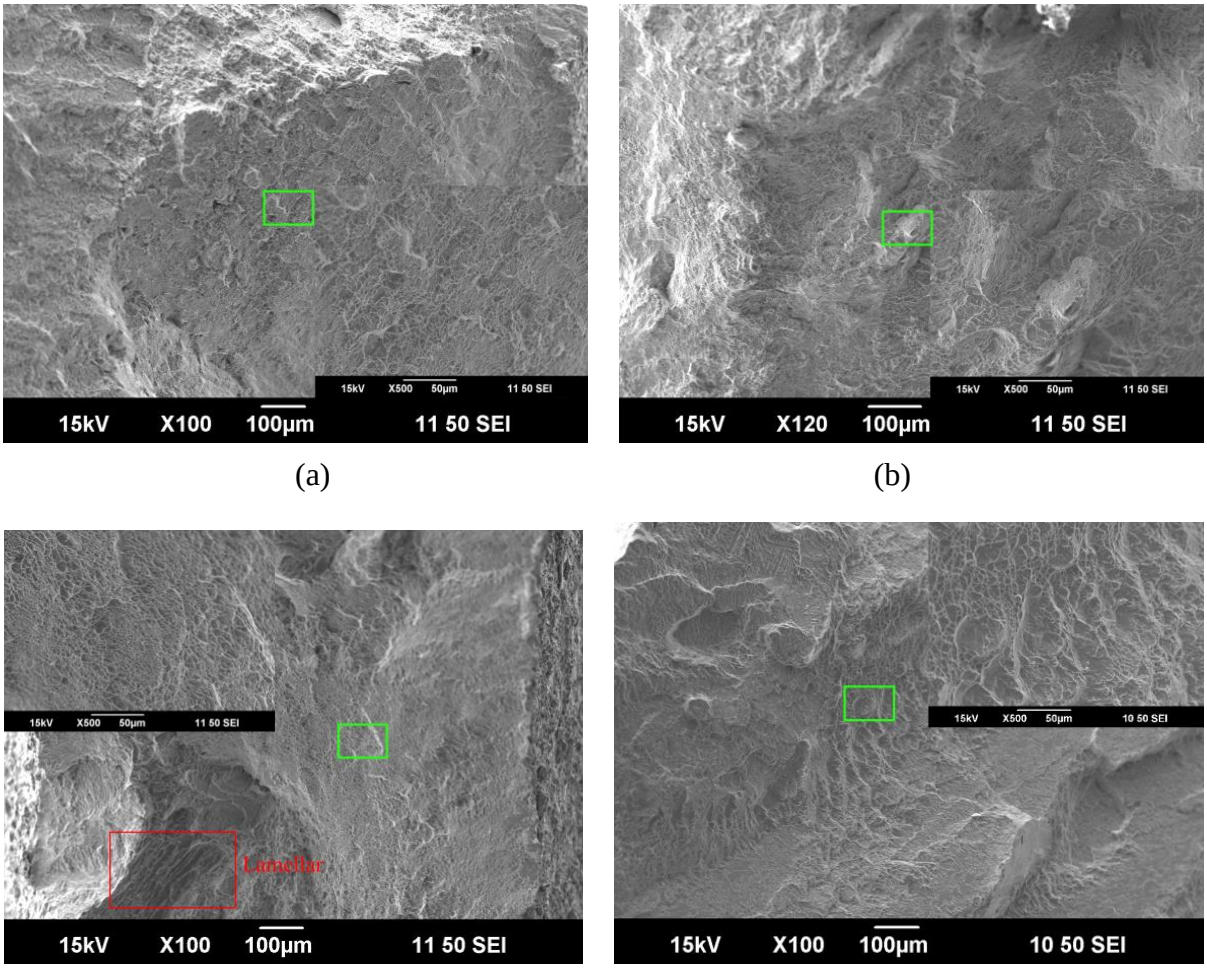

Figure 7-11 High-magnification fractographs of tensile samples: (a) 100°C; (b) 200°C; (c) 300°C; (d) Interpass CO_2 gas cooling

7.4 Discussion

Based on the results presented in the previous section, the influence of in-process

interpass temperature on the deposition geometry, surface oxidation and mechanical properties is significant, but there are no obvious changes in the microstructural evolution and hardness values. The use of forced interpass cooling discernibly improves the material properties, which suggests that the overall material properties of Ti6Al4V components, in this case, may be better controlled during the WAAM process.

It is accepted practice to visually inspect the surface additively manufactured Ti6Al4V parts for coloration and surface imperfections, as this gives an indication of the effectiveness of the inert gas shielding envelope against atmospheric contamination [131]. In this study, the localized gas shielding is only effective for the most recently deposited layers. Generally, the unshielded part is easily oxidized when depositing. As found from experimental results, when a low interpass temperature of 100°C is used, significantly less oxidation is generated on the exposed deposition surface. The low initial component temperature results in a sufficiently low final surface temperature (after deposition of the next layer) so the rate of oxygen diffusion into the surface is slow enough that significant coloration does not occur after the shielding gas flow is stopped. When the interpass temperature is increased, oxygen diffusion into the unshielded surfaces of the part progressively increases and is visibly indicated by surface coloration, accompanied by deteriorating bulk material properties. When using CO_2 gas interpass cooling, clean fabricated surfaces are achieved, with only very light oxidation, as indicated by a faint straw color. This demonstrates that interpass cooling is an effective method for minimizing surface oxidation in WAAM using localized gas shielding, while also significantly reducing the interpass dwell time. WAAM fabrication of highly reactive metals usually involves the use of a closed chamber containing an inert gas atmosphere. This

imposes severe constraints on equipment operation and maximum component size, as well as the inability to introduce other production aids such as CO_2 gas cooling to reduce production times. This study proposes an effective method for fabricating reactive metals such as Ti6Al4V using localized gas shielding in an open environment, while being able to produce components with acceptable properties. This could play an important role in reducing processing times and cost of production and improving manufacturing efficiency.

Although high interpass temperature for fabrication means less dwell time and hence higher effective deposition rate, the experimental results have shown that the layer geometry is significantly different to that produced at interpass temperatures closer to room temperature. Unless this effect is faithfully modelled by the WAAM path planning algorithm and compensatory steps are taken, the geometrical accuracy of the produced part will be poor. Hence, the interpass temperature should be considered in the path planning process for depositing and needs to be controlled during the manufacturing process. This may need to include the initial additive deposit on the substrate. Although this aspect has not been studied here because it would be considered as pre-heating, it may be necessary to avoid the geometrical inaccuracies that are often produced in the first few layers. Alternatively, the WAAM deposition parameters for the first few layers will need to have an effectively higher ratio of heat input to produce the desired geometry.

With reference to the distribution of band structures seen in the cross-sectional macrographs of the deposited parts, Baufeld et al. [13] have claimed that material taken from top regions of deposits exhibiting convex bands is much weaker than material taken from bottom regions exhibiting parallel bands. This is in agreement with the tensile results

obtained in this study. As the interpass temperature increases, more convex bands develop, leading to an increased area with inferior mechanical properties. However, more deposition layers can be visible since these convex bands form in association with layered bulges which represent the liquids of subsequent WAAM steps, as indicated by Baufeld et al. [62]. The proportion of the deposit containing parallel bands is reduced as the interpass temperature increases, indicating a reduction of build area with comparatively superior mechanical properties. It should be mentioned that these parallel bands perform inconsistency with visible deposition layers, which is evident by their end in the indentation between layered bulges [13]. For this case, forced interpass cooling is considered as an effective way to increase the number of parallel bands, as shown in **Figure 7-6** and **Figure 7-7**, and the resulting effects are even better than those for the manufacturing process with low interpass temperature achieved from natural cooling, due to the widening of band structures at higher cooling rates.

Referring to material properties, interpass temperature only has a small effect on the microstructures, but it has been observed that rapid interpass cooling causes more grain refinement, producing correspondingly better performance in hardness and mechanical properties. The hardness of WAAM-fabricated Ti6Al4V is mainly determined by solid solution and grain boundaries or dislocation distribution due to some segregated elements interacting between grain boundaries, and edge dislocations existing in α/β microstructures [73, 175]. When forced interpass cooling is used, the deposit cools down faster than for the case of natural cooling, which thus brings more grain boundaries and dislocations to produce higher microhardness values [145]. Furthermore, the Ti6Al4V microstructure obtained at

high cooling rates consists of large amounts of massive α phases with acicular appearance and non-equilibrium composition, which are usually harder and have higher strength than those produced at lower cooling rates. For the same reason, forced interpass cooling produces deposits with higher hardness. It should be mentioned that the massive α phase has similar crystalline structure to lamellar α phase and has similar chemical composition to β phase [176], which contributes to the hardness being uniformly distributed in the integral part even when the process conditions are changed.

Another benefit of forced interpass cooling is that for Ti6Al4V α+β structures, high cooling rate and rapid solidification rate are also expected to increase the β phase, helping to make the phase distribution more easily approach the equilibrium (around 5% β phase and 95% α phase) [177]. Therefore the material strength, in a manner, is enhanced.

Form the Discussion part, it is apparent that what this study prefers to display is a comprehensive analysis of WAAM printed Ti6Al4V alloy with forced interpass cooling using compressed CO_2. It is believed that the proposed innovative process is beneficial to the fabricated part. In near future, the best practices for applying interpass cooling and localized gas shielding will be continued.

7.5 Conclusion

In this study, Ti6Al4V alloy has been used as the build material for the GT-WAAM process using localized gas shielding. The effects of various interpass temperatures and CO_2 gas interpass cooling on the bead geometry, surface oxidation, microstructural morphology, grain size, mechanical properties and fracture features were investigated. The findings include:

(1) In terms of microstructural evolution and hardness, the properties of WAAM-fabricated Ti6Al4V components are measurably different but not greatly affected by variation of the interpass temperature. However, it is still necessary to control interpass temperature to a reasonable range to ensure the geometric accuracy of each deposited layer and to avoid surface oxidation.

(2) Forced interpass cooling using compressed CO_2 gas is easily implemented, and is beneficial to additively manufactured Ti6Al4V components, contributing to an appealing surface finish with less visible surface oxidation, refined microstructure, improved hardness and enhanced strength.

(3) WAAM deposition with CO_2 gas interpass cooling significantly promotes manufacturing efficiency through a sharp reduction of dwell time between the deposited layers.

Further investigations will focus on the effects of different cooling gas flow rates and various cooling times on the deposition properties in order to validate the effectiveness of this process. In addition, quantitative temperature measurement using IR pyrometry will be used to explore the thermal behaviour during deposition with interpass cooling. The residual stress and deformation of WAAM fabricated components will also be presented in near future.

Chapter 8 DISTORTION CONTROL

8.1 Introduction

Thermal distortion often affects every part of wire arc additively manufactured component, since the feed materials experience non-uniform thermal expansion and contraction under alternate heating and cooling cycles during layered deposition [141, 169]. Mukherjee et al. [178] reported the thermal distortion in additively manufactured parts is a result of the combined effects of material properties, geometric features, deposition pathways, process parameters and preheating or cooling conditions. Denlinger et al. [43] found that thermal distortion is able to accumulate along the build direction due to ineffective heat dissipation and the resultant introduced preheat for the subsequent layer. It is well known that a WAAM-deposited component exhibits different types of distortion, including longitudinal and transverse shrinkage, bending distortion, angular distortion and rotational distortion, resulting in imprecise geometry of the final part and also creating residual stress that may lead to failure during service[103]. Hence, it is necessary to control the thermal distortion to an acceptable range to ensure adequate quality of WAAM parts.

To address this issue, it is critical to predict the thermal state or the internal stress field changes in the deposition. A study was conducted by Cao et al.[179] to examine the distortion characteristics and residual stress distribution in WAAM-fabricated Ti6Al4V structures, and proposed that preheating of the substrate can significantly mitigate residual stress and distortion. Montevecchi et al.[180] introduced a number of simulation methods to predict

distortion during deposition, and satisfactory results were achieved by experimental validation.

To date, both thermal and mechanical methods can be used to reduce the distortion in WAAM-fabricated parts. Thermal methods mainly consist of heat input control and post-fabrication heat treatment. Typically, heat input control within an acceptable range only reduces the part distortion to a limited extent, while post heat treatment is time-consuming, costly and limited by the size of the produced component. Attempts have been made to develop efficient and low-cost equipment to reduce distortion, for example, using interpass cold rolling and designing suitable manufacturing fixtures [181]. However, the interpass cold rolling technique is only feasible for deposited parts with simple shapes such as straight walls, due to geometrical limitations of the rolling process [114]. Designing a variety of fixtures to minimize flexibility of work pieces obviously brings more labour and higher costs for manufacturing [182]. Recently, active interpass cooling using compressed CO_2 was applied to the WAAM process. It was found that this innovative approach provided benefits to the WAAM-produced Ti6AL4V alloy, contributing to an appealing surface finish with refined microstructure, enhanced tensile strength and improved microhardness [183].

In this section, an active interpass cooling process, where compressed CO_2 is used to cool the area behind the heat source, is employed to reduce flexural distortions in WAAM Ti6Al4V wall structures. By means of experiment and simulation, the thermal histories, geometrical features and distortional characteristics are evaluated for components produced with and without interpass cooling. Moreover, a comparative analysis between results is presented, aiming to discuss the feasibility of adding sequential active interpass cooling into

the WAAM process to control part distortion.

8.2 Experimental Procedures

8.2.1 Experiment setup

The apparatus employed in this research work as shown in **Figure 8-1**.

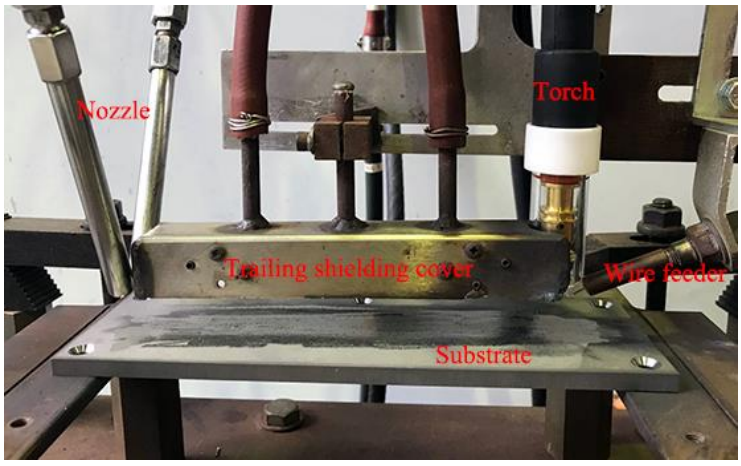

Figure 8-1 Experimental setups of the GT-WAAM deposition system with forced interpass cooling

In this study, active interpass cooling was achieved by delivering a stable CO_2 stream through a commercially-available spray nozzle located behind the trailing gas shield cover, as displayed in **Figure 8-1**. The cooling temperature achieved by the compressed CO_2 was measured at approximately -78 °C. As the relatively turbulent CO_2 flow may induce arc disruption during deposition, the CO_2 spray was started immediately after the deposited layer was completed and the arc was extinguished. Subsequently, the cooling spray was passed over the newly deposited layer with the same speed as the deposition, and it was stopped when the spray arrived at the end of the wall. Three nozzle types were alternatively tested, delivering CO_2 gas flow rates of 320 g/min, 730 g/min and 1460 g/min respectively. During the build, the thermal profiles were continuously monitored by a thermocouple which was

attached to the mid-length of the substrate and offset by 20mm from the deposition path, as shown in **Figure 8-2**. The recorded data was processed using LabVIEW software.

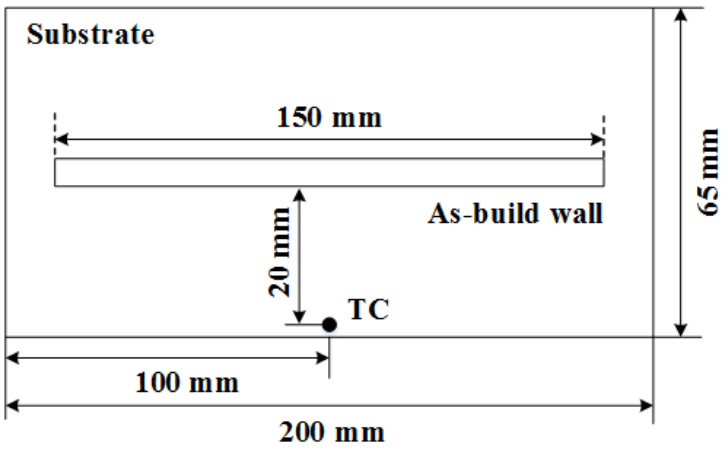

Figure 8-2 Schematic of temperature measurement location for the thermocouple

Six straight wall structures were produced with different process parameters using the described additive manufacturing system. Various cooling gas flow rates and cooling times were selected to explore the influence of different cooling strategies on thermal distortion. Accordingly, specimens were divided into three groups by cooling conditions, as listed in **Table 8-1**. Group I, with test specimen coded as S1, refers to the deposition without interpass cooling and serves as a reference. Group II with specimens from S2 to S4 and Group III with specimens S2, S5 and S6 were designed to investigate the effects of cooling gas flow rate and cooling time, respectively. The cooling times for Group III were determined by the ratio of travel speeds, which compares as relative time for the investigation. The detailed parameter design for the cooling process is provided in **Table 8-1**, and the deposition parameters are listed in **Table 8-2**. Welding grade argon (99.995% purity) was used as shielding gas for both welding torch and trailing shield cover.

Table 8-1 Parameter design for cooling process

Group	Deposition sample	CO_2 flow rate (g/min)	Travel speed (mm/min)	Delay time (min)
I	S1	0	150	N/A
II	S2	320	150	1
	S3	730	150	1
	S4	1460	150	1
III	S5	320	230	0.65
	S6	320	300	0.5

Table 8-2 Welding and deposition process parameters

Processing parameters	Details
Welding current	140A
Arc voltage	15.5V
Wire feed speed	1060 mm/min
Distance from electrode to workpiece	3 mm
Angle between electrode and filler wire	60°
Flow rate of argon in GTAW welding torch	15 L/min
Flow rate of trailing shield	15 L/min
Number of deposited layer	10

8.2.2 The deformation measurement

To measure the distortion of the as-deposited specimens, a 3D laser profile scanner with a resolution of 0.02 mm was used and the recorded data was processed with commercial MATLAB software.

8.2.3 Modeling process

8. 2.3.1 Finite element model

As shown in **Figure 8-3**, only half of the symmetrical substrate is modeled in order to reduce the simulation time. In the finite element model, the minimum mesh unit has a dimension of 1.3 mm × 1.5 mm × 0.9 mm. ANSYS SOLID5 and a 3D coupled-field element

with 8 nodes were adopted. SOLID5 has 3D magnetic, electric, thermal, piezoelectric and structural field capability with limited coupling between each field. In this study, thermal and structural field coupling was utilized. The finite element model generated 5396 units and 7804 nodes during the simulation process.

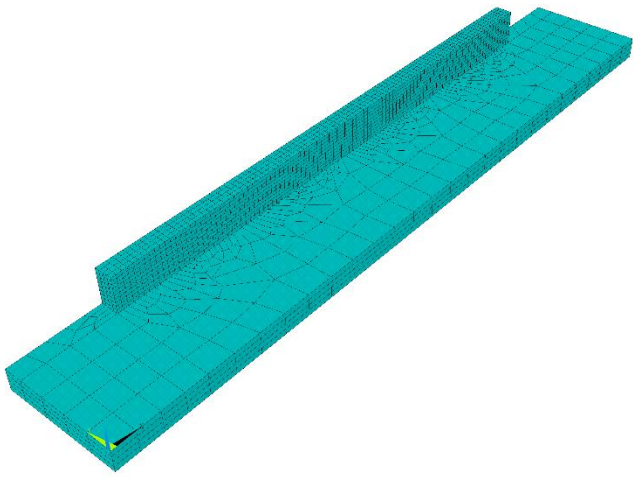

Figure 8-3 3D finite element mesh for one half of build plate

8.2.3.2 Heat source

In the numerical simulation, the heat source distribution is described by the following expression:

$$\{q(x,y) = 3P \cdot \eta \exp(-3(x^2 + y^2)/R^2)/(\pi R^2)\} \quad (8\text{-}1)$$

where q(x, y) is heat flux density; P is the power of welding arc; η is the welding arc efficiency (η =0.7); $x^2 + y^2$ is the square of the distance from the calculation point to the center of the arc and R is the radius of the arc (R =10 mm).

8.2.3.3 Cooling process

When simulating the air-cooled deposition process (Group I), the temperature at the reference point would be checked at the end of each step. Each cooling step lasted for 100

seconds. Once the temperature of the reference point reached room temperature, the natural cooling process would be terminated and the welding process for the next layer would be initiated.

In the simulation of deposition with CO_2 interpass cooling (Group II and Group III), nodes at the CO_2 spray cooling position were applied with temperature constraints using the data measured respectively after each cooling process to simulate the rapid temperature drop of the weldment. As the gas nozzle moved along the welding direction, the cooling position changed with time. Therefore, at the beginning of each step, temperature constraints of the position that had just been cooled down in the previous step would be removed and new temperature constraints would be added to the new cooling region.

8.2.3.4 Boundary conditions and material attributes

A reference temperature was set to indicate the initial temperature at the beginning of the simulation. Reference temperature was also used to simulate room temperature during the calculation. Displacement constraints that simulate the fixture of the workpiece have great influence on the stress calculation and displacement results. Four corners of the plate were set to rigid displacement in all three directions to simulate the constraints of the fixture bolts during the deposition process, as shown in **Figure 8-4**. After process completion, the constraints at these nodes were deleted to simulate the removal of the bolts after the process. Also, in order to avoid drift of the entire structure, one corner node of the plate was set to full constraint and three nodes at the other three corners were set to rigid displacement in the vertical direction. Displacements parallel to the transverse direction were constrained on the symmetrical face.

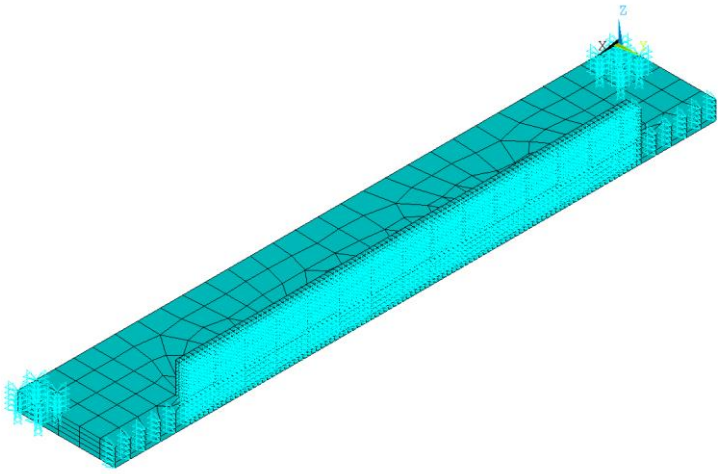

Figure 8-4 The boundary conditions for the simulated model

Temperature field simulation of the welding process is a non-linear transient analysis. Properties of the material, such as yield strength, elastic modulus, specific heat and thermal conductivity are temperature-dependent. Therefore, property data is associated with a temperature table. Poisson's ratio is considered to be constant since the change of Poisson's ratio with temperature is quite small. Therefore, it was set to 0.3 during the whole simulation process.

The workpiece was encompassed by varied thermal mediums. Heat transfer from the top surface of the workpiece was mainly conducted by air, and heat transfer from the bottom surface was considered to be forced convection to the worktable. As a result, heat transfer coefficients were set differently in different areas. No heat transfer coefficient was set on the symmetrical face.

8.3 Results and discussion

8.3.1 Thermal behaviours during deposition

Figure 8-5 shows the thermal profiles measured by thermocouple during the deposition process, with and without active interpass cooling. It is observed that when the welding torch moved along the travel direction, the temperature increased rapidly until a peak temperature was achieved. After completing the deposition of each layer, the temperature gradually decreased with natural cooling, but a much sharper drop in temperature occurs with interpass cooling. As a result, the build time for the 10 deposited layers in this study was reduced by at least 80 percent when CO_2 cooling was implemented, as comparably shown in **Figure 8-5**. It is evident that active interpass cooling in WAAM can offer a significant build-time saving through a dramatic reduction of interlayer dwell time, and thereby provides a means for improvement of manufacturing efficiency.

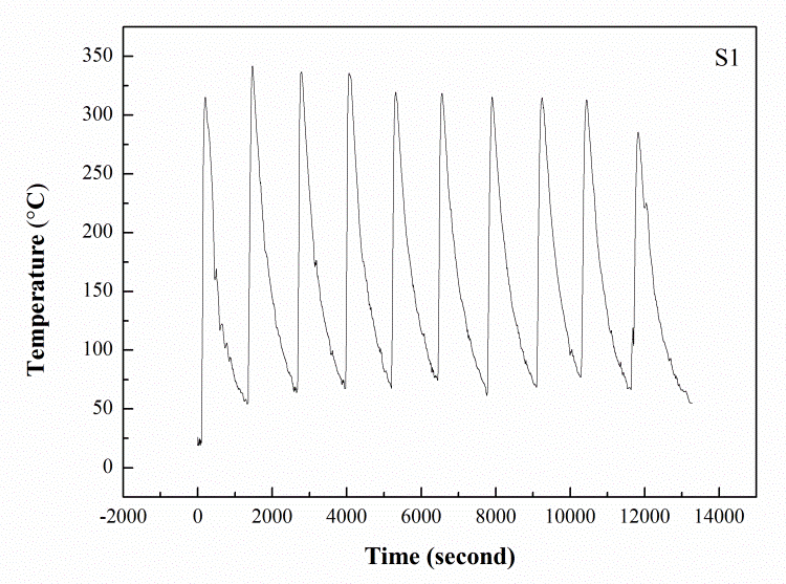

(a)

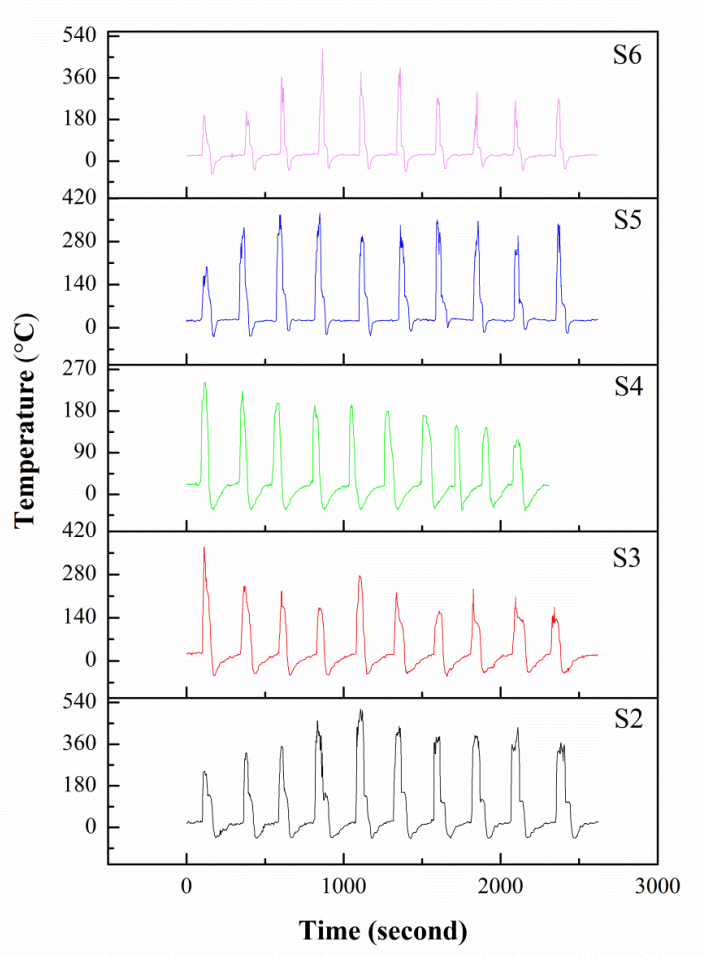

(b)

Figure 8-5 The temperature profiles of deposition (a) with natural cooling and (b) with active interpass cooling

Variations in thermal profile occur when the CO_2 cooling gas flow rate or cooling time are changed during fabrication. **Figure 8-6** compares the thermal histories of one selected layer in all five depositions using different cooling parameters. With increased CO_2 gas flow rate from 320g/min (S2) to 1460g/min (S4), the peak temperature could be reduced by over 50% due to a significant increase in heat removal from the component after the previous layer was deposited. As well, this trend can be observed in processes with increased travel speeds (S2, S5 & S6), whereby lower heat input brings likewise lower heat accumulation along the build direction. Hence, it is accepted that the combined effects of heat input, cooling gas flow

rate and cooling time potentially determines the development of peak temperature, which could be related to the different cooling effects in the deposition. Additionally, active interpass cooling can cause uneven distribution of heat in the build part. Due to the increased thermal dissipation in the uppermost layer of deposit, the interior part produces a large difference between the highest and the lowest values that cooling rates may take. As the deposition suffered from uneven heat distribution, it expands irregularly in all directions, resulting in inhomogeneous stress and distortion to the build part.

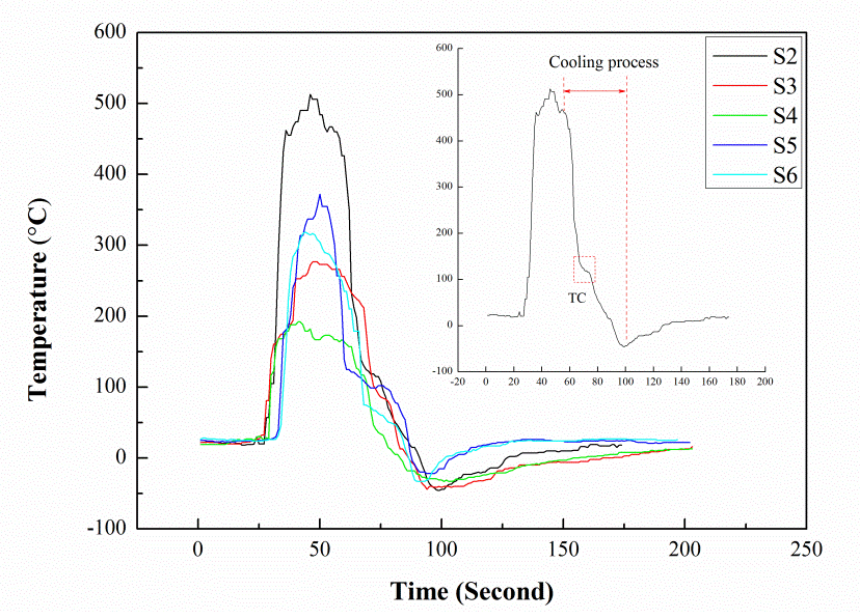

Figure 8-6 The thermal history of one selected layer with different active interpass cooling processes for specimens S2 to S6

8.3.2 Geometrical features

Figure 8-7 shows the geometrical features of as-deposited specimens in this study. Compared to the specimen produced with natural cooling (S1), when using active interpass cooling at the same travel speed (S2, S3 and S4) the average width of build walls was reduced by around 7 % and average height increased by about 6 %. Due to the rapid cooling

produced by compressed CO_2, a decreasing amount of heat distributed in the previous deposition is considered as the part of heat input for the subsequent layer, contributing to lower temperatures in the molten pool and surrounding area, and thus a narrower layer weld bead. So, although active interpass cooling can be a tremendous advantage to promote manufacturing efficiency, the results have shown that the build geometry changes slightly. Unless, this effect is correctly modelled in path planning step or compensatory steps are taken during the build process, the geometrical accuracy of the final part will be compromised. Therefore, when the proposed cooling method is implemented in WAAM, it should also be considered in the path planning strategy to ensure geometrical accuracy of the product.

It should be noted that specimens S5 and S6 were produced at different deposition travel speeds, so the bead dimensions would be different to S1, even before the additional influence of active interpass cooling.

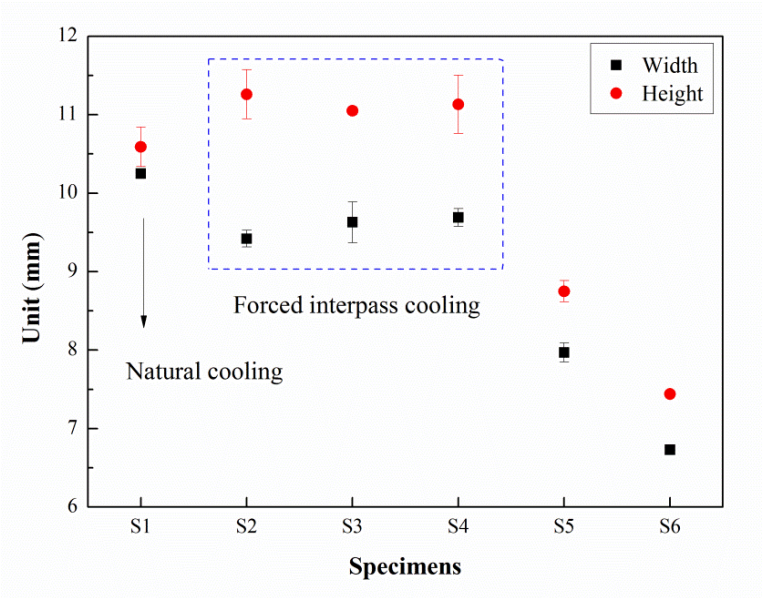

Figure 8-7 Effect of forced interpass cooling on wall dimensions

8.3.3 Thermal distortion

Figure 8-8 shows the simulation results for the distortion of the additively manufactured specimens. **Figure 8-9** further displays the distortion of the substrate, examined along the longitudinal direction (travel direction) and transverse direction (perpendicular to the travel direction). When adding sequential interpass cooling to the deposition process, the produced part sees an 81% and 69% in the maximum reduction of the longitudinal and transverse distortion, respectively. The simulation results are basically consistent with experimental observation, which indicates that active interpass cooling is able to significantly mitigate the distortion issues in WAAM parts.

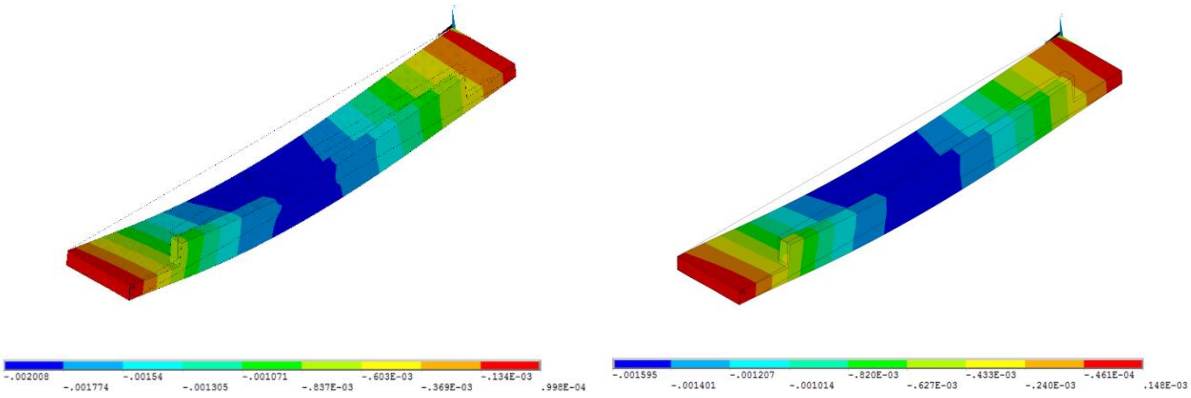

(a) S1 (b) S2

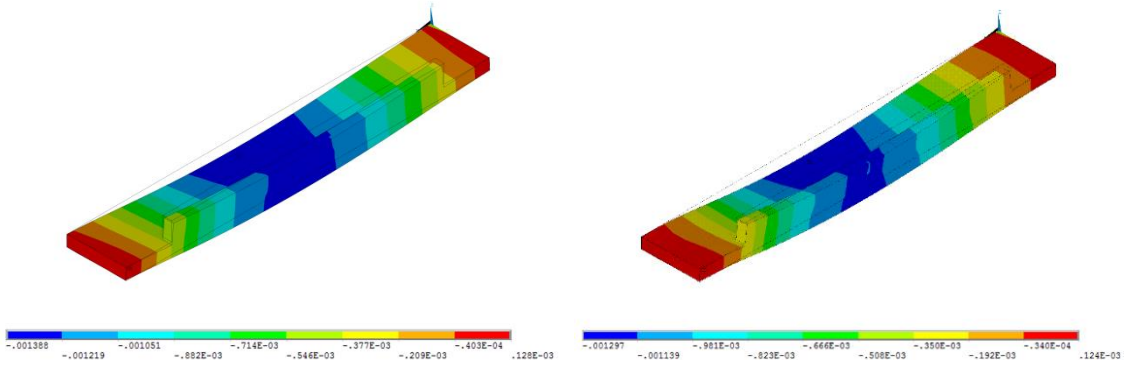

(c) S3 (d) S4

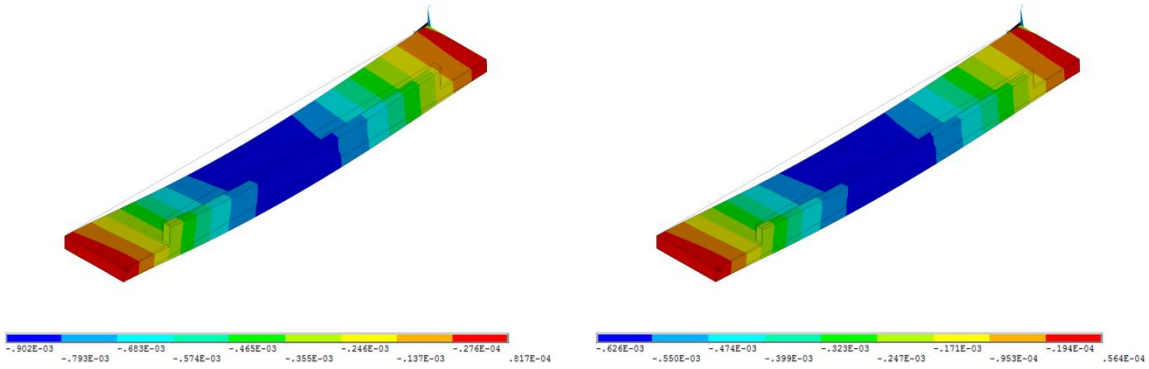

(e) S5 (f) S6

Figure 8-8 Simulation results for the distortion of produced samples: (a) S1; (b) S2; (c) S3; (d) S4; (e) S5; (f) S6.

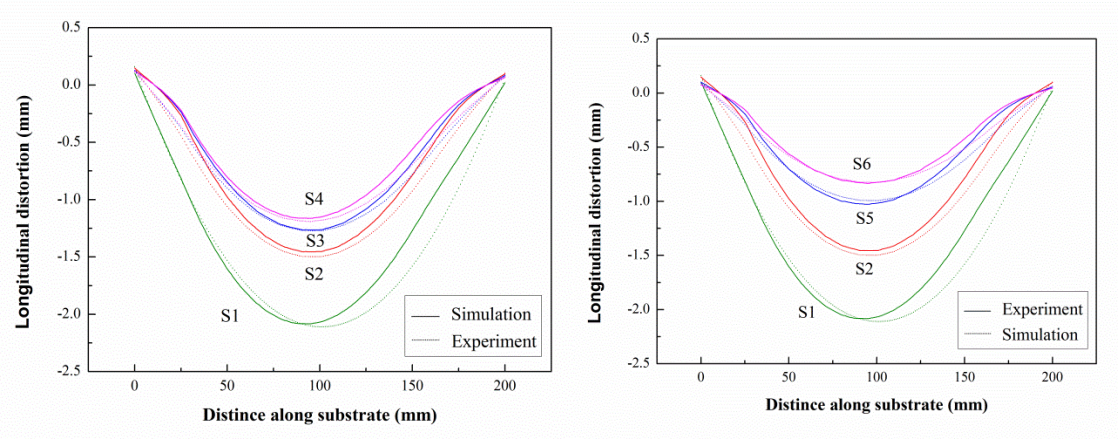

(a) Longitudinal distortion

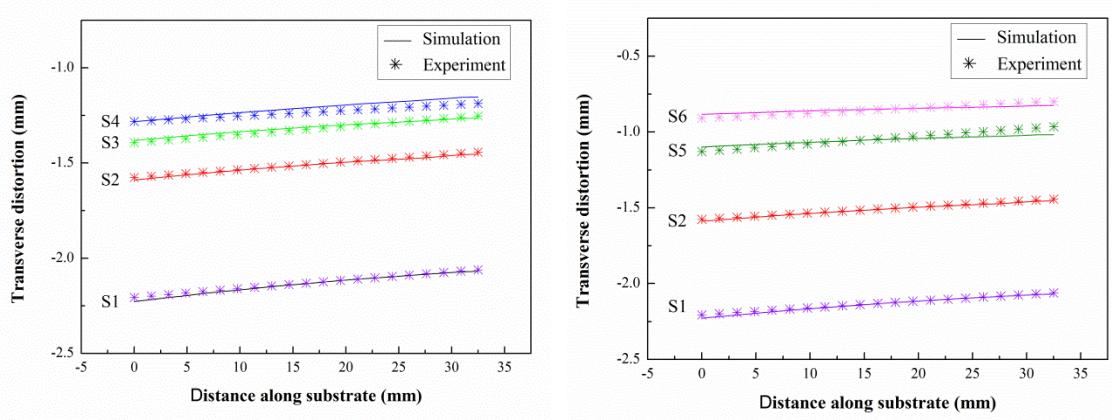

(b) Transverse distortion

Figure 8-9 The thermal distortion of as-deposited specimens: (a) longitudinal distortion and (b) transverse distortion of half of substrate.

Due to non-uniform thermal contraction in the melt area, shrinkage, which is inhibited by underlying materials, takes place. The generation and development of shrinkage induces a tensile stress in the newly added top layer and a compressive stress is generated in underlying layers, which leads to a localized distortion in the deposited areas. During deposition, theses localized distortions, particularly in the first few layers, accumulate along the build direction. These lead to distortion and dimensional variation in the final part, as shown in **Figure 8-10**. In extreme cases, complete loss of the planned bead deposit dimensional control may occur. It is worth noting that part distortion reached a steady-state condition after several layers of build, due to the thermal strain reaching a nearly constant value. Obvious distortion is generated along the travel direction, attributable to the large thermal strain.

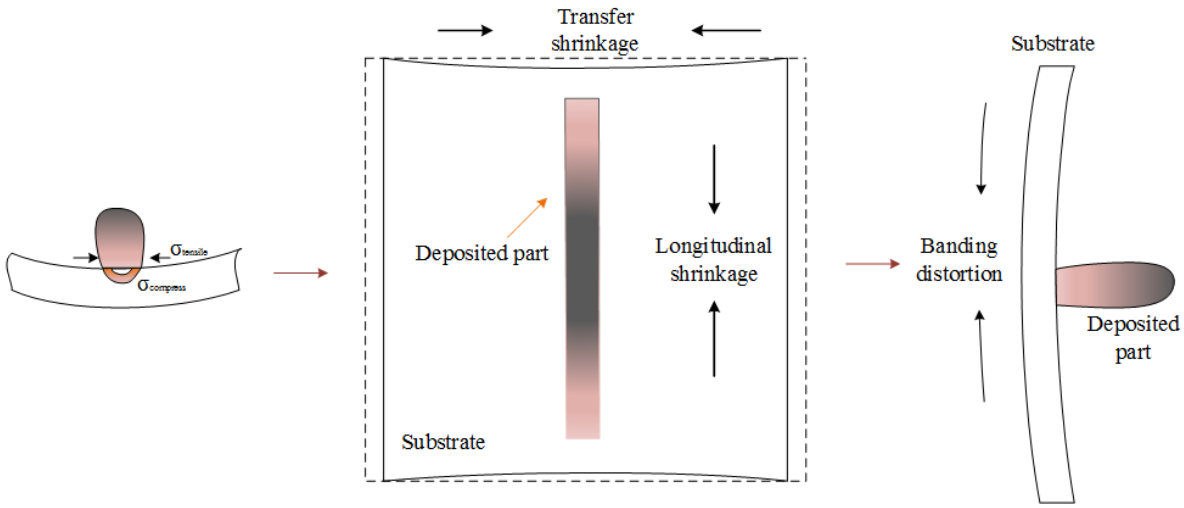

Figure 8-10 The distortion mechanism in WAAM-fabricated Ti6Al4V process

Two main parameters, cooling gas flow rates and cooling time, are primarily responsible for the change in distortion of parts produced using the WAAM process with active interpass cooling. Mukherjee et al. reported that that thermal distortion of an additively manufactured part is dependent on a strain parameter, ε*[184]:

$$\varepsilon * = \frac{\beta \Delta T t H^{\frac{3}{2}}}{EIF\sqrt{\rho}} \tag{8-2}$$

$$F = \frac{\alpha \tau}{w^2} = \frac{\alpha}{V} L \tag{8-3}$$

where β is the volumetric coefficient of thermal expansion, E is the elastic modulus, ΔT is the maximum rise in temperature, I is the moment of inertia of the substrate, t is the characteristic time, H is the heat input per unit length, F is the Fourier number which is the ratio of the heat dissipation rate to heat storage rate, ρ is the density of the alloy wire, α refers to thermal diffusivity, τ is characteristic time scale, w is deposition length, V is the traveling speed, and L is the length of molten pool. Eq (2) and (3) demonstrate that both reducing heat accumulation and improving heat dissipation in a deposited part can result in a high Fourier number and low peak temperature, leading to a low thermal strain and distortion for the additively manufactured part [178]. With the assistance of active interpass cooling, the heat stored in the deposit can be quickly dissipated, contributing to less heat accumulation. This is useful for the reduction of distortions that are difficult to mitigate with mechanical methods. In addition, distortion accumulation can also be reduced by decreasing the interlayer dwell time as pointed out by Denlinger *et al*. When active interpass cooling used, the inherently shortened dwell period brings less distortion accumulation, contributing to the desired geometrical performance of the final produced part.

In comparison to the results produced by solely adjusting the cooling gas flow rate (Group II), the effect of adjusting both the deposition speed and the cooling time (Group III) provides improved mitigation of distortion, which may be attributed to the combined effects of reduced heat input at deposition and even further shortened dwell time between deposits,

creating greater average heat dissipation per unit time during the build process. From this point of view, if active interpass cooling is used, distortion control is more effective through setting the cooling time rather than purely varying the cooling gas flow rate. By this approach, both cooling efficiency improvement and cooling gas savings can be achieved. However, the shape of the deposited material is necessarily different, so the path planning algorithm must compensate for such changes.

The primary focus of this paper has been to propose and evaluate an innovative method for low distortion WAAM fabrication of metal components, while promoting high manufacturing efficiency. Active interpass cooling using compressed CO_2 is effective in reducing distortion of WAAM components and improving dimensional accuracy. Future work will investigate the residual stress distribution in components which are produced by different cooling times and cooling gas flow rates during fabrication.

8.4 Conclusion

In this study, an innovative WAAM process with active interpass cooling using compressed CO_2 was developed for fabricating Ti6Al4V wall structures. The thermal behavior, geometrical features, and distortion characteristics of as-fabricated specimens were investigated and discussed. The following conclusions could be drawn:

(1) By applying active interpass cooling between deposition of layers, the build times have been reduced by at least 80%.

(2) By means of active interpass cooling, significant distortion reduction is possible in produced parts due to rapid heat removal and consequently decreased heat accumulation

during deposition. It was observed that simultaneously altering deposition and cooling times has a greater mitigation effect on thermal distortion than only adjusting the cooling gas flow rate, which is possibly related to the difference in the overall heat dissipation per unit time.

(3) Since active interpass cooling affects the deposition process, the path planning strategy should take this into consideration, and more optimized strategies for distortion control should be considered from the cooling time point of view.

Chapter 9 CONCLUDING REMARKS

Through matching a knowledge of material characteristics with the performance features of particular WAAM techniques, a quality-based framework is proposed, for producing high-quality and defect-free components in this chapter. A brief summary and future research direction are following provided.

9.1 A quality-based framework for WAAM process

Improving process stability, eliminating or decreasing deposition defects and producing components with high quality and mechanical performance have become major research focuses in making the WAAM process more competitive against other additive manufacturing methods. An in-depth understanding of various materials, ideal process setup, in-process parameter control and post processing is essential for achieving such a goal. After a systematic review and analysis, a quality-based framework aiming to achieve high-quality and defects-free WAAM process is proposed, as shown in **Figure 9-1**. Three main aspects are considered: feedstock optimization, manufacturing process, and postprocess treatment.

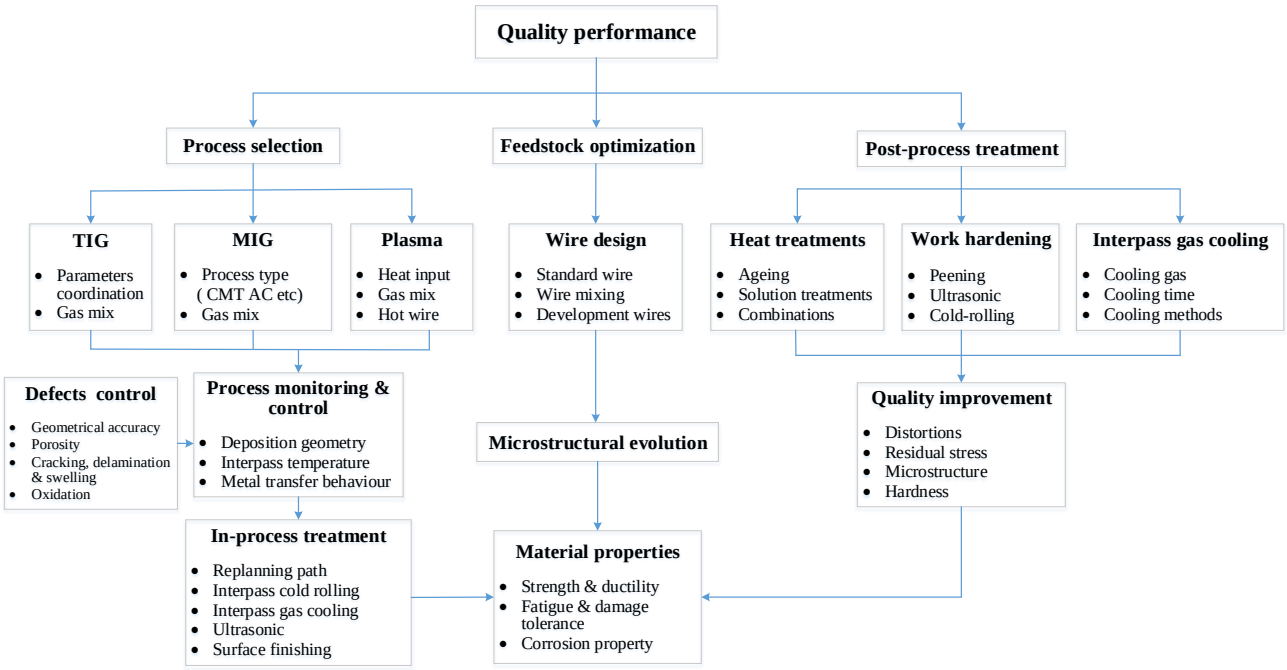

Figure 9-1 A quality-based framework for WAAM process

Selection of the most suitable welding WAAM process for the deposition material can ensure manufacturing process stability and contribute to reduction of defects. For example, if the CMT-PADV process is used for producing aluminum parts, porosity defects can be dramatically reduced when compared to other GMAW modes [98]. Moreover, integrated and reliable process monitoring and control systems are needed to maintain the stability of the process and ensure the quality of production. Usually, the bead geometry, interpass temperature, arc characteristics and metal transfer behaviour are included in process monitoring and control. Controlling the interpass temperature within a reasonable range is beneficial to microstructural evolution and the resulting mechanical properties. Further, regulating the arc characteristics and metal transfer behaviour in real time is helpful to process stability and avoidance of defects. Based on the process monitoring data that has been collected during deposition, one (or more) of several postprocess treatments can be

selected to mitigate defects and improve mechanical performance.

Considering the material characteristics, microstructural evolution and mechanical properties can also be optimized through new feedstock composition design. It is well known that different alloying elements have specific effects on material properties. By referring to the phase diagram, the desired deposition microstructures can be obtained via adding specific alloying elements in the feedstock and subsequent mechanical properties improved. Moreover, availability of wire mixings provides a potential possibility for building large functionally graded products for special applications. For example, twin-wire GTAW-based WAAM has been successfully developed to produce intermetallic graded materials [24, 90]. The development of new powder cored wires will offer exciting opportunities for fabricating target components with accurate metal composition. In summary, using new welding consumables brings a cost-effective solution, which supports high deposition quality through obtaining the desired microstructures, lowering manufacturing costs by reducing or eliminating pre-weld cleaning and re-work, and providing safer working environments by reducing weld fumes.

Another essential part of WAAM processing for most materials is post-process treatment, which is used to reduce residual stresses and distortion, refine microstructures, improve microhardness and enhance material strength. However, post-process technologies have their own limitations, for instance, peening and ultrasonic impact treatment only improve material property and reduce defects near the part surface, while extended heat treatment of certain materials promotes grain growth rather than grain refinement. Currently, most WAAM fabricated parts need to be post-process treated with a selective combination of technologies

to reduce the defects and improve the product quality to the greatest extent possible.

9.2 Future perspective

In WAAM of metallic materials, the fundamental interrelationships between material composition and microstructure govern the material properties and fabrication quality. Since the WAAM process is an inherently non-equilibrium thermal process, it is challenging to predicate and control the microstructural evolution, which is responsible for the variation of mechanical properties in the deposited part. Further research attention should be paid on the study of underlying physical and chemical metallurgical mechanisms in WAAM process to provide a guidance for the process optimization, improvement and control. The defects generated in WAAM-produced part are closely related to the target material characteristics and process parameters. The development of strategies or ancillary process to overcome defects generation are of prime importance. With the requirement of high quality WAAM part, the proposed quality-based framework will see a wide application in the future years.

As WAAM matures as a commercial manufacturing process, development of a commercially available WAAM system for metal components is an interdisciplinary challenge, which integrates physical welding process development, materials science and thermo-mechanical engineering, and mechatronic and control system design. Although much research has been carried out over recent years in various areas, such as process planning, programming, and material study, a general purpose off-the-shelf WAAM system similar to commercially available powder-bed fusion systems is yet to be developed. Due to the variety of requirements of different engineering materials and the varying scale of fabrication, many different WAAM system designs are expected to be developed that will be optimized for

particular applications, rather than a single system that is capable of addressing all of the possible problems.

PUBLICATION

[1] **Bintao Wu**, Zengxi Pan *, Donghong Ding, Dominic Cuiuri, Huijun Li, Jing Xu, John Norrish. A review on the wire arc additive manufacturing of metals: property, defect and quality improvement. *Journal of Manufacturing Processes*, 35 (2018):127-139. – from **Chapter 2**

[2] **Bintao Wu**, Donghong Ding, Zengxi Pan*, DominicCuiuri, Huijun Li, Jian Han, Zhenyu Fei. Effects of heat accumulation on the arc characteristics and metal transfer behavior in Wire Arc Additive Manufacturing of Ti6Al4V. *Journal of Materials Processing Technology*, 250 (2017):304 -312. – from **Chapter 4**

[3] **Bintao Wu**, Zengxi Pan*, Donghong Ding, Dominic Cuiuri, Huijun Li. Effects of heat accumulation on microstructure and mechanical properties of Ti6Al4V alloy deposited by wire arc additive manufacturing. *Additive Manufacturing*, 23(2018):151-160. – from **Chapter 5**

[4] **Bintao Wu**, Zenxi Pan*, Siyuan Li, Huijun Li,Donghong Ding, Dominic Cuiuri. The anisotropic corrosion behaviours of wire arc additive manufactured Ti-6Al-4V parts in 3.5% NaCl solution. *Corrosion Science*, 137 (2018):176 -183. -from **Chapter 6**

[5] **Bintao Wu**, Zengxi Pan *, Donghong Ding, Dominic Cuiuri, Huijun Li, Zhenyu Fei. The effects of forced interpass cooling on the material properties of wire arc additively

manufactured Ti6Al4V alloy, *Journal of Materials Processing Technol*ogy, 258 (2018):97-105. -from **Chapter 7**

[6] **Bintao Wu**, Zengxi Pan *, Donghong Ding, Guangyu Chen, Lei Yuan, Huijun Li, Dominic Cuiuri, Stephen van Duin. Mitigation of thermal distortion in wire arc additively manufactured Ti6Al4V parts using active interpass cooling. *Science and Technology of Welding and Joining*, 2018, (Accept)-from **chapter 8**

[7] **Bintao Wu**, Zengxi Pan *, Donghong Ding, Huijun Li. Thermal behaviour in Wire arc additive manufacturing: characteristics, effects and control. *Transactions on Intelligent Welding Manufacturing*, 2018, (Accept).

[8] **Bintao Wu**, Zengxi Pan *, Huijun Li, Donghong Ding, Dominic Cuiuri, Lei Yuan, Stephen van Duin. Innovative fabrication of aluminum pillar structure using droplet based wire arc additive manufacturing. *Journal of manufacturing process and technology*, (Under review).

[9] **Bintao Wu**, Zengxi Pan *, Huijun Li, Donghong Ding, Dominic Cuiuri. The effects of gas cooling flow rate and time on the microstructure and mechanical properties of wire arc additively manufactured Ti6Al4V alloy. *Material Science and Engineering A*. (Prepare to submit).

[10] **Bintao Wu**, Zengxi Pan *, Huijun Li, Donghong Ding, Dominic Cuiuri. Investigation on the microstructures and mechanical properties of wire arc additively manufactured Fe/Ni functional part. *Material & Design* (Prepare to submit).

[11] Zengxi Pan, Donghong Ding *, **Bintao Wu**, Dominic Cuiuri, Huijun Li, John Norrish. Arc Welding Processes for Additive Manufacturing: A Review. *Transactions on Intelligent Welding Manufacturing*, 2017, pp:3-24.

[12] Jian Han, Cheng Lu, **Bintao Wu ***, Jintao Li, Huijun Li, Yao Lu, Qiuzhi Gao. Innovative analysis of Luders band behaviour in X80 pipeline steel. *Materials Science and Engineering A*, 683 (2017):123–128.

[13] Yugang, Miao, Benshun, Zhang, **Bintao Wu***, Xiaoxiao Wang, Guangyu Chen, Duanfeng Han. Joint characteristics and corrosion properties of bypass-current double-sided Arc-welded aluminum 6061 alloy with Al-Si filler metal. *Acta Metallurgica Sinica (English Letters)*, 29 (2016):360 –366.

[14] Zhengyu Fei, Zengxi Pan, Dominic Cuiuri, Huijun Li, **Bintao Wu**, Donghong Ding, Lihong Su, AA. Gazder. Investigation into the viability of K-TIG for joining armour grade quenched and tempered steel. *Journal of Manufacturing Processes*, 32 (2018):482-493.

[15] Zhengyu Fei, Zengxi Pan, Dominic Cuiuri, Huijun Li, **Bintao Wu**, Lihong Su, Improving the weld microstructure and material properties of K-TIG welded armour steel joint using filler material. *The International Journal of Advanced Manufacturing Technology*, 10 (2018): 1-14.

REFERENCE

[1] R. Acheson, Automatic welding apparatus for weld build-up and method of achieving weld build-up, in, Google Patents, 1987.

[2] P. Dickens, M. Pridham, R. Cobb, I. Gibson, G. Dixon, Rapid prototyping using 3-D welding, in, DTIC Document, 1992.

[3] J. Spencer, P. Dickens, C. Wykes, Rapid prototyping of metal parts by three-dimensional welding, Proceedings of the Institution of Mechanical Engineers, Part B: Journal of Engineering Manufacture, 212 (1998) 175-182.

[4] R. Kovacevic, H. Beardsley, Process Control of3D Welding as a Droplet-Based Rapid Prototyping Technique, in: Proc. ofthe SFF Symposium, Univ. ofTexas at Austin, Austin TX, 1998, pp. 57-64.

[5] R. Dwivedi, R. Kovacevic, Automated torch path planning using polygon subdivision for solid freeform fabrication based on welding, Journal of Manufacturing Systems, 23 (2004) 278-291.

[6] Z. Jandric, M. Labudovic, R. Kovacevic, Effect of heat sink on microstructure of three-dimensional parts built by welding-based deposition, International Journal of Machine Tools and Manufacture, 44 (2004) 785-796.

[7] Y.-A. Song, S. Park, D. Choi, H. Jee, 3D welding and milling: Part I–a direct approach for freeform fabrication of metallic prototypes, International Journal of Machine Tools and Manufacture, 45 (2005) 1057-1062.

[8] Y.-A. Song, S. Park, S.-W. Chae, 3D welding and milling: part II—optimization of the 3D

welding process using an experimental design approach, International Journal of Machine Tools and Manufacture, 45 (2005) 1063-1069.

[9] Y. Zhang, Y. Chen, P. Li, A.T. Male, Weld deposition-based rapid prototyping: a preliminary study, Journal of Materials Processing Technology, 135 (2003) 347-357.

[10] Y.M. Zhang, P. Li, Y. Chen, A.T. Male, Automated system for welding-based rapid prototyping, Mechatronics, 12 (2002) 37-53.

[11] Y.-M. Kwak, C.C. Doumanidis, Geometry Regulation of Material Deposition in Near-Net Shape Manufacturing by Thermally Scanned Welding, Journal of Manufacturing Processes, 4 (2002) 28-41.

[12] M. Katou, J. Oh, Y. Miyamoto, K. Matsuura, M. Kudoh, Freeform fabrication of titanium metal and intermetallic alloys by three-dimensional micro welding, Materials & Design, 28 (2007) 2093-2098.

[13] B. Baufeld, O.V.d. Biest, R. Gault, Additive manufacturing of Ti–6Al–4V components by shaped metal deposition: Microstructure and mechanical properties, Materials & Design, 31, Supplement 1 (2010) S106-S111.

[14] D. Clark, M.R. Bache, M.T. Whittaker, Shaped metal deposition of a nickel alloy for aero engine applications, Journal of Materials Processing Technology, 203 (2008) 439-448.

[15] R. Merz, F. Prinz, K. Ramaswami, M. Terk, L. Weiss, Shape deposition manufacturing, Engineering Design Research Center, Carnegie Mellon Univ., 1994.

[16] J. Xiong, G. Zhang, H. Gao, L. Wu, Modeling of bead section profile and overlapping beads with experimental validation for robotic GMAW-based rapid manufacturing, Robotics and Computer-Integrated Manufacturing, 29 (2013) 417-423.

[17] J. Xiong, G. Zhang, Z. Qiu, Y. Li, Vision-sensing and bead width control of a single-bead multi-layer part: material and energy savings in GMAW-based rapid manufacturing, Journal of Cleaner Production, 41 (2013) 82-88.

[18] D. Yang, C. He, G. Zhang, Forming characteristics of thin-wall steel parts by double electrode GMAW based additive manufacturing, Journal of Materials Processing Technology, 227 (2016) 153-160.

[19] W. Aiyiti, W. Zhao, B. Lu, Y. Tang, Investigation of the overlapping parameters of MPAW-based rapid prototyping, Rapid Prototyping Journal, 12 (2006) 165-172.

[20] S. Suryakumar, K.P. Karunakaran, A. Bernard, U. Chandrasekhar, N. Raghavender, D. Sharma, Weld bead modeling and process optimization in Hybrid Layered Manufacturing, Computer-Aided Design, 43 (2011) 331-344.

[21] D. Ding, Z. Pan, D. Cuiuri, H. Li, A tool-path generation strategy for wire and arc additive manufacturing, The International Journal of Advanced Manufacturing Technology, 73 (2014) 173-183.

[22] D. Ding, Z. Pan, D. Cuiuri, H. Li, A practical path planning methodology for wire and arc additive manufacturing of thin-walled structures, Robotics and Computer-Integrated Manufacturing, 34 (2015) 8-19.

[23] D. Ding, Z. Pan, D. Cuiuri, H. Li, N. Larkin, Adaptive path planning for wire-feed additive manufacturing using medial axis transformation, Journal of Cleaner Production, 133 (2016) 942-952.

[24] Y. Ma, D. Cuiuri, H. Li, Z. Pan, C. Shen, The effect of postproduction heat treatment on γ-TiAl alloys produced by the GTAW-based additive manufacturing process, Materials

Science and Engineering: A, 657 (2016) 86-95.

[25] Reduce costs and increase output with robotic welding, in, https://www.scottautomation.com/applications/metal-fabrication/welding/.

[26] S.W. Williams, F. Martina, A.C. Addison, J. Ding, G. Pardal, P. Colegrove, Wire + Arc Additive Manufacturing, Materials Science and Technology, 32 (2016) 641-647.

[27] Y. Zhang, Y. Chen, P. Li, A.T. Male, Weld deposition-based rapid prototyping: a preliminary study, Journal of Materials Processing Technology, 135 (2003) 347-357.

[28] D. Ding, Z. Pan, D. Cuiuri, H. Li, Wire-feed additive manufacturing of metal components: technologies, developments and future interests, The International Journal of Advanced Manufacturing Technology, 81 (2015) 465-481.

[29] G.N. Levy, R. Schindel, J.P. Kruth, RAPID MANUFACTURING AND RAPID TOOLING WITH LAYER MANUFACTURING (LM) TECHNOLOGIES, STATE OF THE ART AND FUTURE PERSPECTIVES, CIRP Annals - Manufacturing Technology, 52 (2003) 589-609.

[30] W.E. Frazier, Metal additive manufacturing: a review, Journal of Materials Engineering and Performance, 23 (2014) 1917-1928.

[31] J.J. Lewandowski, M. Seifi, Metal additive manufacturing: a review of mechanical properties, Annual Review of Materials Research, 46 (2016) 151-186.

[32] W. Gao, Y. Zhang, D. Ramanujan, K. Ramani, Y. Chen, C.B. Williams, C.C.L. Wang, Y.C. Shin, S. Zhang, P.D. Zavattieri, The status, challenges, and future of additive manufacturing in engineering, Computer-Aided Design, 69 (2015) 65-89.

[33] J. Ding, P. Colegrove, J. Mehnen, S. Ganguly, P.M. Sequeira Almeida, F. Wang, S.

Williams, Thermo-mechanical analysis of Wire and Arc Additive Layer Manufacturing process on large multi-layer parts, Computational Materials Science, 50 (2011) 3315-3322.

[34] D. Ding, Z. Pan, D. Cuiuri, H. Li, A multi-bead overlapping model for robotic wire and arc additive manufacturing (WAAM), Robotics and Computer-Integrated Manufacturing, 31 (2015) 101-110.

[35] D. Ding, Z. Pan, D. Cuiuri, H. Li, S. van Duin, N. Larkin, Bead modelling and implementation of adaptive MAT path in wire and arc additive manufacturing, Robotics and Computer-Integrated Manufacturing, 39 (2016) 32-42.

[36] D. Ding, C. Shen, Z. Pan, D. Cuiuri, H. Li, N. Larkin, S. van Duin, Towards an automated robotic arc-welding-based additive manufacturing system from CAD to finished part, Computer-Aided Design, 73 (2016) 66-75.

[37] D.-H. Ding, Z.-X. Pan, C. Dominic, H.-J. Li, Process Planning Strategy for Wire and Arc Additive Manufacturing, in: Robotic Welding, Intelligence and Automation, Springer, 2015, pp. 437-450.

[38] D. Ding, Z. Pan, D. Cuiuri, H. Li, S. van Duin, Advanced Design for Additive Manufacturing: 3D Slicing and 2D Path Planning, in: New Trends in 3D Printing, InTech, 2016.

[39] P. Sequeira Almeida, Process control and development in wire and arc additive manufacturing, in, Cranfield University, 2012.

[40] J. Xiong, Z. Yin, W. Zhang, Closed-loop control of variable layer width for thin-walled parts in wire and arc additive manufacturing, Journal of Materials Processing Technology, 233 (2016) 100-106.

[41] H. Geng, J. Li, J. Xiong, X. Lin, F. Zhang, Optimization of wire feed for GTAW based additive manufacturing, Journal of Materials Processing Technology, 243 (2017) 40-47.

[42] S. Zhang, J. Li, H. Kou, J. Yang, G. Yang, J. Wang, Effects of thermal history on the microstructure evolution of Ti-6Al-4V during solidification, Journal of Materials Processing Technology, 227 (2016) 281-287.

[43] E.R. Denlinger, J.C. Heigel, P. Michaleris, T.A. Palmer, Effect of inter-layer dwell time on distortion and residual stress in additive manufacturing of titanium and nickel alloys, Journal of Materials Processing Technology, 215 (2015) 123-131.

[44] J. Gu, J. Ding, S.W. Williams, H. Gu, J. Bai, Y. Zhai, P. Ma, The strengthening effect of inter-layer cold working and post-deposition heat treatment on the additively manufactured Al–6.3Cu alloy, Materials Science and Engineering: A, 651 (2016) 18-26.

[45] A. Uriondo, M. Esperon-Miguez, S. Perinpanayagam, The present and future of additive manufacturing in the aerospace sector: A review of important aspects, Proceedings of the Institution of Mechanical Engineers, Part G: Journal of Aerospace Engineering, 229 (2015) 2132-2147.

[46] S.L. Sing, J. An, W.Y. Yeong, F.E. Wiria, Laser and electron-beam powder-bed additive manufacturing of metallic implants: A review on processes, materials and designs, Journal of Orthopaedic Research, 34 (2016) 369-385.

[47] L.E. Murr, S. Gaytan, A. Ceylan, E. Martinez, J. Martinez, D. Hernandez, B. Machado, D. Ramirez, F. Medina, S. Collins, Characterization of titanium aluminide alloy components fabricated by additive manufacturing using electron beam melting, Acta Materialia, 58 (2010) 1887-1894.

[48] N. Guo, M.C. Leu, Additive manufacturing: technology, applications and research needs, Frontiers of Mechanical Engineering, 8 (2013) 215-243.

[49] K.U. Kainer, Metal matrix composites: custom-made materials for automotive and aerospace engineering, John Wiley & Sons, 2006.

[50] C. Leyens, M. Peters, Titanium and titanium alloys: fundamentals and applications, John Wiley & Sons, 2003.

[51] T.B. Kim, S. Yue, Z. Zhang, E. Jones, J.R. Jones, P.D. Lee, Additive manufactured porous titanium structures: Through-process quantification of pore and strut networks, Journal of Materials Processing Technology, 214 (2014) 2706-2715.

[52] R. Wang, F.H. Beck, New stainless steel without nickel or chromium for marine applications, Met. Prog., 123 (1983) 72.

[53] M. Aziz-Kerrzo, K.G. Conroy, A.M. Fenelon, S.T. Farrell, C.B. Breslin, Electrochemical studies on the stability and corrosion resistance of titanium-based implant materials, Biomaterials, 22 (2001) 1531-1539.

[54] G. Lu, G. Zangari, Corrosion resistance of ternary Ni P based alloys in sulfuric acid solutions, Electrochimica Acta, 47 (2002) 2969-2979.

[55] N. Stoloff, C. Liu, S. Deevi, Emerging applications of intermetallics, Intermetallics, 8 (2000) 1313-1320.

[56] O.K. Varghese, D. Gong, M. Paulose, C.A. Grimes, E.C. Dickey, Crystallization and high-temperature structural stability of titanium oxide nanotube arrays, Journal of Materials Research, 18 (2003) 156-165.

[57] B. Bewlay, M. Jackson, P. Subramanian, J.-C. Zhao, A review of very-high-temperature

Nb-silicide-based composites, Metallurgical and Materials Transactions A, 34 (2003) 2043-2052.

[58] M. Jackson, B. Bewlay, R. Rowe, D. Skelly, H. Lipsitt, High-temperature refractory metal-intermetallic composites, JOM, 48 (1996) 39-44.

[59] G. Bissacco, H.N. Hansen, L. De Chiffre, Micromilling of hardened tool steel for mould making applications, Journal of Materials Processing Technology, 167 (2005) 201-207.

[60] L. Yan, Wire and arc addictive manufacture (WAAM) reusable tooling investigation, (2013).

[61] L. Thijs, F. Verhaeghe, T. Craeghs, J.V. Humbeeck, J.-P. Kruth, A study of the microstructural evolution during selective laser melting of Ti–6Al–4V, Acta Materialia, 58 (2010) 3303-3312.

[62] B. Baufeld, O.v.d. Biest, R. Gault, Microstructure of Ti-6Al-4V specimens produced by shaped metal deposition, International Journal of Materials Research, 100 (2009) 1536-1542.

[63] D. Herzog, V. Seyda, E. Wycisk, C. Emmelmann, Additive manufacturing of metals, Acta Materialia, 117 (2016) 371-392.

[64] J. Lin, Y. Lv, Y. Liu, Z. Sun, K. Wang, Z. Li, Y. Wu, B. Xu, Microstructural evolution and mechanical property of Ti-6Al-4V wall deposited by continuous plasma arc additive manufacturing without post heat treatment, Journal of the Mechanical Behavior of Biomedical Materials, 69 (2017) 19-29.

[65] J.J. Lin, Y.H. Lv, Y.X. Liu, B.S. Xu, Z. Sun, Z.G. Li, Y.X. Wu, Microstructural evolution and mechanical properties of Ti-6Al-4V wall deposited by pulsed plasma arc additive manufacturing, Materials & Design, 102 (2016) 30-40.

[66] Y. Hirata, Pulsed arc welding, Welding international, 17 (2003) 98-115.

[67] B. Baufeld, E. Brandl, O. Van der Biest, Wire based additive layer manufacturing: comparison of microstructure and mechanical properties of Ti–6Al–4V components fabricated by laser-beam deposition and shaped metal deposition, Journal of Materials Processing Technology, 211 (2011) 1146-1158.

[68] F. Wang, S.W. Williams, M. Rush, Morphology investigation on direct current pulsed gas tungsten arc welded additive layer manufactured Ti6Al4V alloy, (2011).

[69] E. Brandl, D. Greitemeier, Microstructure of additive layer manufactured Ti–6Al–4V after exceptional post heat treatments, Materials Letters, 81 (2012) 84-87.

[70] B.A. Szost, S. Terzi, F. Martina, D. Boisselier, A. Prytuliak, T. Pirling, M. Hofmann, D.J. Jarvis, A comparative study of additive manufacturing techniques: Residual stress and microstructural analysis of CLAD and WAAM printed Ti–6Al–4V components, Materials & Design, 89 (2016) 559-567.

[71] E. Brandl, B. Baufeld, C. Leyens, R. Gault, Additive manufactured Ti-6Al-4V using welding wire: comparison of laser and arc beam deposition and evaluation with respect to aerospace material specifications, Physics Procedia, 5 (2010) 595-606.

[72] J. Zhang, X. Zhang, X. Wang, J. Ding, Y. Traoré, S. Paddea, S. Williams, Crack path selection at the interface of wrought and wire + arc additive manufactured Ti–6Al–4V, Materials & Design, 104 (2016) 365-375.

[73] E. Brandl, A. Schoberth, C. Leyens, Morphology, microstructure, and hardness of titanium (Ti-6Al-4V) blocks deposited by wire-feed additive layer manufacturing (ALM), Materials Science and Engineering: A, 532 (2012) 295-307.

[74] F. Wang, S. Williams, P. Colegrove, A.A. Antonysamy, Microstructure and Mechanical Properties of Wire and Arc Additive Manufactured Ti-6Al-4V, Metallurgical and Materials Transactions A, 44 (2013) 968-977.

[75] F. Martina, J. Mehnen, S.W. Williams, P. Colegrove, F. Wang, Investigation of the benefits of plasma deposition for the additive layer manufacture of Ti–6Al–4V, Journal of Materials Processing Technology, 212 (2012) 1377-1386.

[76] J. Gu, J. Ding, S.W. Williams, H. Gu, P. Ma, Y. Zhai, The effect of inter-layer cold working and post-deposition heat treatment on porosity in additively manufactured aluminum alloys, Journal of Materials Processing Technology, 230 (2016) 26-34.

[77] P. Wang, S. Hu, J. Shen, Y. Liang, Characterization the contribution and limitation of the characteristic processing parameters in cold metal transfer deposition of an Al alloy, Journal of Materials Processing Technology, 245 (2017) 122-133.

[78] C. Brice, R. Shenoy, M. Kral, K. Buchannan, Precipitation behavior of aluminum alloy 2139 fabricated using additive manufacturing, Materials Science and Engineering: A, 648 (2015) 9-14.

[79] B.K. Agrawal, Introduction to Engineering Materials, Tata McGraw-Hill, New Delhi, 2007.

[80] D. Dittrich, J. Standfuss, J. Liebscher, B. Brenner, E. Beyer, Laser beam welding of hard to weld Al alloys for a regional aircraft fuselage design–first results, Physics Procedia, 12 (2011) 113-122.

[81] B. ASTM, 221-Standard Specification for Aluminum and Aluminum-Alloy Extruded Bars, Rods, Wire, Profiles, and Tubes, (2005).

[82] B. Baufeld, Mechanical Properties of INCONEL 718 Parts Manufactured by Shaped Metal Deposition (SMD), Journal of Materials Engineering and Performance, 21 (2012) 1416-1421.

[83] F. Xu, Y. Lv, Y. Liu, F. Shu, P. He, B. Xu, Microstructural Evolution and Mechanical Properties of Inconel 625 Alloy during Pulsed Plasma Arc Deposition Process, Journal of Materials Science & Technology, 29 (2013) 480-488.

[84] M. Bauccio, ASM metals reference book, ASM international, 1993.

[85] F.J. Xu, Y.H. Lv, B.S. Xu, Y.X. Liu, F.Y. Shu, P. He, Effect of deposition strategy on the microstructure and mechanical properties of Inconel 625 superalloy fabricated by pulsed plasma arc deposition, Materials & Design, 45 (2013) 446-455.

[86] J.F. Wang, Q.J. Sun, H. Wang, J.P. Liu, J.C. Feng, Effect of location on microstructure and mechanical properties of additive layer manufactured Inconel 625 using gas tungsten arc welding, Materials Science and Engineering: A, 676 (2016) 395-405.

[87] D. Ding, Z. Pan, S. van Duin, H. Li, C. Shen, Fabricating Superior NiAl Bronze Components through Wire Arc Additive Manufacturing, Materials, 9 (2016) 652.

[88] J. Guo, Y. Zhou, C. Liu, Q. Wu, X. Chen, J. Lu, Wire Arc Additive Manufacturing of AZ31 Magnesium Alloy: Grain Refinement by Adjusting Pulse Frequency, Materials, 9 (2016) 823.

[89] C. Shen, Z. Pan, Y. Ma, D. Cuiuri, H. Li, Fabrication of iron-rich Fe–Al intermetallics using the wire-arc additive manufacturing process, Additive Manufacturing, 7 (2015) 20-26.

[90] C. Shen, Z. Pan, D. Cuiuri, B. Dong, H. Li, In-depth study of the mechanical properties for Fe3Al based iron aluminide fabricated using the wire-arc additive manufacturing process,

Materials Science and Engineering: A, 669 (2016) 118-126.

[91] Y. Ma, D. Cuiuri, N. Hoye, H. Li, Z. Pan, Characterization of In-Situ Alloyed and Additively Manufactured Titanium Aluminides, Metallurgical and Materials Transactions B: Process Metallurgy and Materials Processing Science, 45 (2014) 2299-2303.

[92] Y. Ma, D. Cuiuri, C. Shen, H. Li, Z. Pan, Effect of interpass temperature on in-situ alloying and additive manufacturing of titanium aluminides using gas tungsten arc welding, Additive Manufacturing, 8 (2015) 71-77.

[93] T. Abe, H. Sasahara, Dissimilar metal deposition with a stainless steel and nickel-based alloy using wire and arc-based additive manufacturing, Precision Engineering, 45 (2016) 387-395.

[94] L. Liu, Z. Zhuang, F. Liu, M. Zhu, Additive manufacturing of steel–bronze bimetal by shaped metal deposition: interface characteristics and tensile properties, The International Journal of Advanced Manufacturing Technology, 69 (2013) 2131-2137.

[95] B. Dong, Z. Pan, C. Shen, Y. Ma, H. Li, Fabrication of Copper-Rich Cu-Al Alloy Using the Wire-Arc Additive Manufacturing Process, Metallurgical and Materials Transactions B, (2017).

[96] P. Almeida, S. Williams, Innovative process model of Ti–6Al–4V additive layer manufacturing using cold metal transfer (CMT), in.

[97] J. Xiong, G. Zhang, W. Zhang, Forming appearance analysis in multi-layer single-pass GMAW-based additive manufacturing, The International Journal of Advanced Manufacturing Technology, 80 (2015) 1767-1776.

[98] H. Wang, W. Jiang, J. Ouyang, R. Kovacevic, Rapid prototyping of 4043 Al-alloy parts

by VP-GTAW, Journal of Materials Processing Technology, 148 (2004) 93-102.

[99] B. Cong, J. Ding, S. Williams, Effect of arc mode in cold metal transfer process on porosity of additively manufactured Al-6.3%Cu alloy, The International Journal of Advanced Manufacturing Technology, 76 (2015) 1593-1606.

[100] H. Wang, R. Kovacevic, Variable polarity GTAW in rapid prototyping of aluminum parts, in.

[101] Y. Tian, B. Ouyang, A. Gontcharov, R. Gauvin, P. Lowden, M. Brochu, Microstructure evolution of Inconel 625 with 0.4 wt% boron modification during gas tungsten arc deposition, Journal of Alloys and Compounds, 694 (2017) 429-438.

[102] Z.P. Bosheng Dong, Chen Shen, Yan Ma, Huijun Li, Fabrication of copper-rich Cu-Al alloy using the wire-arc additive manufacturing process, Metallurgical and Materials Transactions B: Process Metallurgy and Materials Processing Science, under review (2017).

[103] K. Masubuchi, Analysis of welded structures: Residual stresses, distortion, and their consequences, Elsevier, 2013.

[104] P.A. Colegrove, H.E. Coules, J. Fairman, F. Martina, T. Kashoob, H. Mamash, L.D. Cozzolino, Microstructure and residual stress improvement in wire and arc additively manufactured parts through high-pressure rolling, Journal of Materials Processing Technology, 213 (2013) 1782-1791.

[105] W.J. Sames, F. List, S. Pannala, R.R. Dehoff, S.S. Babu, The metallurgy and processing science of metal additive manufacturing, International Materials Reviews, 61 (2016) 315-360.

[106] T. Mukherjee, W. Zhang, T. DebRoy, An improved prediction of residual stresses and

distortion in additive manufacturing, Computational Materials Science, 126 (2017) 360-372.

[107] P. Edwards, A. O'Conner, M. Ramulu, Electron beam additive manufacturing of titanium components: properties and performance, Journal of Manufacturing Science and Engineering, 135 (2013) 061016.

[108] A. Busachi, J. Erkoyuncu, P. Colegrove, F. Martina, J. Ding, Designing a WAAM Based Manufacturing System for Defence Applications, Procedia CIRP, 37 (2015) 48-53.

[109] W.J. Sames, F. Medina, W.H. Peter, S.S. Babu, R.R. Dehoff, Effect of Process Control and Powder Quality on Inconel 718 Produced Using Electron Beam Melting, in: 8th International Symposium on Superalloy 718 and Derivatives, John Wiley & Sons, Inc., 2014, pp. 409-423.

[110] J.H. Devletian, W.E. Wood, Factors Affecting Porosity in Aluminum Welds - a Review, Welding Research Council, 1983.

[111] J. Bai, H. Ding, J. Gu, X. Wang, H. Qiu, Porosity evolution in additively manufactured aluminium alloy during high temperature exposure, in: IOP Conference Series: Materials Science and Engineering, IOP Publishing, 2017, pp. 012045.

[112] What is hot cracking (solidification cracking), in, TWI Ltd, http://www.twi-global.com/technical-knowledge/faqs/material-faqs/faq-what-is-hot-cracking-solidification-cracking/, 2017.

[113] T.A. Davis, The Effect of Process Parameters on Laser Deposited Ti-6Al-4V.

[114] P.A. Colegrove, J. Donoghue, F. Martina, J. Gu, P. Prangnell, J. Hönnige, Application of bulk deformation methods for microstructural and material property improvement and residual stress and distortion control in additively manufactured components, Scripta

Materialia, 135 (2017) 111-118.

[115] J.-x. Huang, X.-n. Ye, Z. Xu, Effect of Cold Rolling on Microstructure and Mechanical Properties of AISI 301LN Metastable Austenitic Stainless Steels, Journal of Iron and Steel Research, International, 19 (2012) 59-63.

[116] F. Martina, P.A. Colegrove, S.W. Williams, J. Meyer, Microstructure of Interpass Rolled Wire+ Arc Additive Manufacturing Ti-6Al-4V Components, Metallurgical and Materials Transactions A, 46 (2015) 6103-6118.

[117] P.A. Colegrove, J. Donoghue, F. Martina, J. Gu, P. Prangnell, J. Hönnige, Application of bulk deformation methods for microstructural and material property improvement and residual stress and distortion control in additively manufactured components, Scripta Materialia, 135 (2017) 111-118.

[118] H. Toda, K. Minami, K. Koyama, K. Ichitani, M. Kobayashi, K. Uesugi, Y. Suzuki, Healing behavior of preexisting hydrogen micropores in aluminum alloys during plastic deformation, Acta Materialia, 57 (2009) 4391-4403.

[119] Residual stress reduction in high pressure interpass rolled wire þ arc additive manufacturing Ti–6Al–4V components, in.

[120] S. Williams, Wire + Arc Additive Manufacture – Current and Future Developments, in, Wire + Arc Additive Manufacture – Current and Future Developments, 2017.

[121] J. Donoghue, A.A. Antonysamy, F. Martina, P.A. Colegrove, S.W. Williams, P.B. Prangnell, The effectiveness of combining rolling deformation with Wire–Arc Additive Manufacture on β-grain refinement and texture modification in Ti–6Al–4V, Materials Characterization, 114 (2016) 103-114.

[122] X. Cheng, J.W. Fisher, H.J. Prask, T. Gnäupel-Herold, B.T. Yen, S. Roy, Residual stress modification by post-weld treatment and its beneficial effect on fatigue strength of welded structures, International Journal of Fatigue, 25 (2003) 1259-1269.

[123] G. Li, S. Qu, M. Xie, X. Li, Effect of ultrasonic surface rolling at low temperatures on surface layer microstructure and properties of HIP Ti-6Al-4V alloy, Surface and Coatings Technology, 316 (2017) 75-84.

[124] S.S.f.T.a.T.A.W. ASTM B863-14, ASTM International, West Conshohocken, PA, 2014, www.astm.org.

[125] S.S.f.T.a.T.A.S. ASTM B265-06, Sheet, and Plate, ASTM International, West Conshohocken, PA, 2006, www.astm.org.

[126] C. Shen, Z. Pan, D. Cuiuri, D. Ding, H. Li, Influences of deposition current and interpass temperature to the Fe3Al-based iron aluminide fabricated using wire-arc additive manufacturing process, The International Journal of Advanced Manufacturing Technology, 88 (2017) 2009-2018.

[127] H. Zhao, G. Zhang, Z. Yin, L. Wu, A 3D dynamic analysis of thermal behavior during single-pass multi-layer weld-based rapid prototyping, Journal of Materials Processing Technology, 211 (2011) 488-495.

[128] X. Zhou, H. Zhang, G. Wang, X. Bai, Three-dimensional numerical simulation of arc and metal transport in arc welding based additive manufacturing, International Journal of Heat and Mass Transfer, 103 (2016) 521-537.

[129] P. Hagqvist, F. Sikström, A.-K. Christiansson, Emissivity estimation for high temperature radiation pyrometry on Ti–6Al–4V, Measurement, 46 (2013) 871-880.

[130] D.P. DeWitt, G.D. Nutter, Theory and practice of radiation thermometry, John Wiley & Sons, 1988.

[131] K.-M. Hong, Y.C. Shin, Analysis of microstructure and mechanical properties change in laser welding of Ti6Al4V with a multiphysics prediction model, Journal of Materials Processing Technology, 237 (2016) 420-429.

[132] S. Wang, Z. Liao, Y. Liu, W. Liu, Influence of thermal oxidation temperature on the microstructural and tribological behavior of Ti6Al4V alloy, Surface and Coatings Technology, 240 (2014) 470-477.

[133] M.A. Wahab, M.J. Painter, M.H. Davies, The prediction of the temperature distribution and weld pool geometry in the gas metal arc welding process, Journal of Materials Processing Technology, 77 (1998) 233-239.

[134] H.Z.-C. Fan Ding, Huang Jian-Kang, Wang Xin-Xin, Huang Yong, Three-dimensional numerical analysis of interaction between arc and pool by considering the behavior of the metal vapor in tungsten inert gas welding, Acta Physica Sinica, 64 (2015) 108102.

[135] A.B. during Welding, Liquid Metal Oscillation and Arc Behaviour during Welding.

[136] J.H. Waszink, Experimental investigation of the forces acting on a drop of weld metal, Weld. J., (1983).

[137] J. Waszink, M. Piena, Experimental investigation of drop detachment and drop velocity in GMAW, Welding Journal, 65 (1986) S289-S298.

[138] G. Vastola, G. Zhang, Q.X. Pei, Y.-W. Zhang, Modeling the Microstructure Evolution During Additive Manufacturing of Ti6Al4V: A Comparison Between Electron Beam Melting and Selective Laser Melting, JOM, 68 (2016) 1370-1375.

[139] J. Romano, L. Ladani, J. Razmi, M. Sadowski, Temperature distribution and melt geometry in laser and electron-beam melting processes – A comparison among common materials, Additive Manufacturing, 8 (2015) 1-11.

[140] Y. Li, D. Gu, Thermal behavior during selective laser melting of commercially pure titanium powder: Numerical simulation and experimental study, Additive Manufacturing, 1–4 (2014) 99-109.

[141] B. Wu, D. Ding, Z. Pan, D. Cuiuri, H. Li, J. Han, Z. Fei, Effects of heat accumulation on the arc characteristics and metal transfer behavior in Wire Arc Additive Manufacturing of Ti6Al4V, Journal of Materials Processing Technology, 250 (2017) 304-312.

[142] T. Ahmed, H.J. Rack, Phase transformations during cooling in α+β titanium alloys, Materials Science and Engineering: A, 243 (1998) 206-211.

[143] S.L. Semiatin, S.L. Knisley, P.N. Fagin, D.R. Barker, F. Zhang, Microstructure evolution during alpha-beta heat treatment of Ti-6Al-4V, Metallurgical and Materials Transactions A, 34 (2003) 2377-2386.

[144] M. Peters, J. Hemptenmacher, J. Kumpfert, C. Leyens, Structure and Properties of Titanium and Titanium Alloys, in: Titanium and Titanium Alloys, Wiley-VCH Verlag GmbH & Co. KGaA, 2005, pp. 1-36.

[145] G. Welsch, R. Boyer, E.W. Collings, Materials Properties Handbook: Titanium Alloys, ASM International, 1993.

[146] S.S. Al-Bermani, M.L. Blackmore, W. Zhang, I. Todd, The Origin of Microstructural Diversity, Texture, and Mechanical Properties in Electron Beam Melted Ti-6Al-4V, Metallurgical and Materials Transactions A, 41 (2010) 3422-3434.

[147] G. Lütjering, Influence of processing on microstructure and mechanical properties of (α+β) titanium alloys, Materials Science and Engineering: A, 243 (1998) 32-45.

[148] Y. Kim, Y.-B. Song, S.H. Lee, Microstructure and intermediate-temperature mechanical properties of powder metallurgy Ti–6Al–4V alloy prepared by the prealloyed approach, Journal of Alloys and Compounds, 637 (2015) 234-241.

[149] P. Åkerfeldt, M.-L. Antti, R. Pederson, Influence of microstructure on mechanical properties of laser metal wire-deposited Ti-6Al-4V, Materials Science and Engineering: A, 674 (2016) 428-437.

[150] W. Xu, M. Brandt, S. Sun, J. Elambasseril, Q. Liu, K. Latham, K. Xia, M. Qian, Additive manufacturing of strong and ductile Ti–6Al–4V by selective laser melting via in situ martensite decomposition, Acta Materialia, 85 (2015) 74-84.

[151] N. Dai, L.-C. Zhang, J. Zhang, Q. Chen, M. Wu, Corrosion behavior of selective laser melted Ti-6Al-4 V alloy in NaCl solution, Corrosion Science, 102 (2016) 484-489.

[152] N. Dai, L.-C. Zhang, J. Zhang, X. Zhang, Q. Ni, Y. Chen, M. Wu, C. Yang, Distinction in corrosion resistance of selective laser melted Ti-6Al-4V alloy on different planes, Corrosion Science, 111 (2016) 703-710.

[153] J. Yang, H. Yang, H. Yu, Z. Wang, X. Zeng, Corrosion Behavior of Additive Manufactured Ti-6Al-4V Alloy in NaCl Solution, Metallurgical and Materials Transactions A, 48 (2017) 3583-3593.

[154] M.R. Amaya-Vazquez, J.M. Sánchez-Amaya, Z. Boukha, F.J. Botana, Microstructure, microhardness and corrosion resistance of remelted TiG2 and Ti6Al4V by a high power diode laser, Corrosion Science, 56 (2012) 36-48.

[155] M. Ivašková, M. Lovíšek, P. Jančovič, L. Bukovinová, Influence of temperature on the electrochemical characteristics of Ti-6Al-4V, in: Materials Science Forum, 2014.

[156] M. Lorenzetti, E. Pellicer, J. Sort, M. Baró, J. Kovač, S. Novak, S. Kobe, Improvement to the Corrosion Resistance of Ti-Based Implants Using Hydrothermally Synthesized Nanostructured Anatase Coatings, Materials, 7 (2014) 180.

[157] E. Almanza, M.J. Pérez, N.A. Rodríguez, L.E. Murr, Corrosion resistance of Ti-6Al-4V and ASTM F75 alloys processed by electron beam melting, Journal of Materials Research and Technology, 6 (2017) 251-257.

[158] C. Fonseca, M.A. Barbosa, Corrosion behaviour of titanium in biofluids containing H2O2 studied by electrochemical impedance spectroscopy, Corrosion Science, 43 (2001) 547-559.

[159] B. Grosgogeat, M. Boinet, F. Dalard, M. Lissac, Electrochemical studies of the corrosion behaviour of titanium and the Ti–6Al–4V alloy using electrochemical impedance spectroscopy, Bio-medical materials and engineering, 14 (2004) 323-331.

[160] R.W.-W. Hsu, C.-C. Yang, C.-A. Huang, Y.-S. Chen, Investigation on the corrosion behavior of Ti–6Al–4V implant alloy by electrochemical techniques, Materials Chemistry and Physics, 86 (2004) 269-278.

[161] N. Stanford, P.S. Bate, The martensitic transformation texture in Ti-6Al-4V, in: Materials science forum, Trans Tech Publ, 2005, pp. 669-674.

[162] N. Stanford, P.S. Bate, Crystallographic variant selection in Ti–6Al–4V, Acta Materialia, 52 (2004) 5215-5224.

[163] Y.-w. SUI, B.-s. LI, A.-h. LIU, N. Hai, J.-j. GUO, H.-z. FU, Microstructures and

hardness of Ti-6Al-4V alloy staging castings under centrifugal field, Transactions of Nonferrous Metals Society of China, 18 (2008) 291-296.

[164] J.-R. Chen, W.-T. Tsai, In situ corrosion monitoring of Ti–6Al–4V alloy in H2SO4/HCl mixed solution using electrochemical AFM, Electrochimica Acta, 56 (2011) 1746-1751.

[165] G.R. Argade, S.K. Panigrahi, R.S. Mishra, Effects of grain size on the corrosion resistance of wrought magnesium alloys containing neodymium, Corrosion Science, 58 (2012) 145-151.

[166] Y. Bai, X. Gai, S. Li, L.-C. Zhang, Y. Liu, Y. Hao, X. Zhang, R. Yang, Y. Gao, Improved corrosion behaviour of electron beam melted Ti-6Al–4V alloy in phosphate buffered saline, Corrosion Science, 123 (2017) 289-296.

[167] A.Y. Fasasi, S. Mwenifumbo, N. Rahbar, J. Chen, M. Li, A.C. Beye, C.B. Arnold, W.O. Soboyejo, Nano-second UV laser processed micro-grooves on Ti6Al4V for biomedical applications, Materials Science and Engineering: C, 29 (2009) 5-13.

[168] N.D. Tomashov, G.P. Chernova, Y.S. Ruscol, G.A. Ayuyan, The passivation of alloys on titanium bases, Electrochimica Acta, 19 (1974) 159-172.

[169] P.C. Collins, D.A. Brice, P. Samimi, I. Ghamarian, H.L. Fraser, Microstructural Control of Additively Manufactured Metallic Materials, Annual Review of Materials Research, 46 (2016) 63-91.

[170] S. Suryakumar, K. Karunakaran, U. Chandrasekhar, M. Somashekara, A study of the mechanical properties of objects built through weld-deposition, Proceedings of the Institution of Mechanical Engineers, Part B: Journal of Engineering Manufacture, 227 (2013) 1138-1147.

[171] P. Henckell, K. Günther, Y. Ali, J.P. Bergmann, J. Scholz, P. Forêt, The Influence of Gas Cooling in Context of Wire Arc Additive Manufacturing—A Novel Strategy of Affecting Grain Structure and Size, in: TMS 2017 146th Annual Meeting & Exhibition Supplemental Proceedings, Springer, 2017, pp. 147-156.

[172] R. Holder, N. Larkin, H. Li, L. Kuzmikova, Z. Pan, J. Norrish, Development of a DC-LSND welding process for GMAW on DH-36 Steel, (2011).

[173] X. Tan, Y. Kok, Y.J. Tan, M. Descoins, D. Mangelinck, S.B. Tor, K.F. Leong, C.K. Chua, Graded microstructure and mechanical properties of additive manufactured Ti–6Al–4V via electron beam melting, Acta Materialia, 97 (2015) 1-16.

[174] T.M. Mower, M.J. Long, Mechanical behavior of additive manufactured, powder-bed laser-fused materials, Materials Science and Engineering: A, 651 (2016) 198-213.

[175] G. Lütjering, J.C. Williams, Titanium, Springer, 2007.

[176] C. Charles, Microstructure model for Ti-6Al-4V used in simulation of additive manufacturing, in, Luleå tekniska universitet, 2016.

[177] G. Welsch, W. Bunk, H. Kellerer, Einfluß von Spannungsfrei-Glühung und Abkühlungsgeschwindigkeit auf Mikrostruktur und Festigkeit von TiAl6V4, Materialwissenschaft und Werkstofftechnik, 8 (1977) 141-148.

[178] T. Mukherjee, V. Manvatkar, A. De, T. DebRoy, Mitigation of thermal distortion during additive manufacturing, Scripta Materialia, 127 (2017) 79-83.

[179] J. Cao, M.A. Gharghouri, P. Nash, Finite-element analysis and experimental validation of thermal residual stress and distortion in electron beam additive manufactured Ti-6Al-4V build plates, Journal of Materials Processing Technology, 237 (2016) 409-419.

[180] F. Montevecchi, G. Venturini, N. Grossi, A. Scippa, G. Campatelli, Finite Element mesh coarsening for effective distortion prediction in Wire Arc Additive Manufacturing, Additive Manufacturing, 18 (2017) 145-155.

[181] Y. Zhang, Y. Ying, X. Liu, H. Wei, Deformation control during the laser welding of a Ti6Al4V thin plate using a synchronous gas cooling method, Materials & Design, 90 (2016) 931-941.

[182] T. Schenk, I.M. Richardson, M. Kraska, S. Ohnimus, A study on the influence of clamping on welding distortion, Computational Materials Science, 45 (2009) 999-1005.

[183] B. Wu, Z. Pan, D. Ding, D. Cuiuri, H. Li, Z. Fei, The effects of forced interpass cooling on the material properties of wire arc additively manufactured Ti6Al4V alloy, Journal of Materials Processing Technology, 258 (2018) 97-105.

[184] T. Mukherjee, J. Zuback, A. De, T. DebRoy, Printability of alloys for additive manufacturing, Scientific reports, 6 (2016) 19717.